

1 **Configuration and validation of an oceanic physical and**  
2 **biogeochemical model to investigate coastal**  
3 **eutrophication in the Southern California Bight**

4 **Fayçal Kessouri<sup>1</sup>, Karen McLaughlin<sup>1</sup>, Martha Sutula<sup>1</sup>, Daniele Bianchi<sup>2</sup>,**  
5 **Minna Ho<sup>1</sup>, James C McWilliams<sup>2</sup>, Lionel Renault<sup>2,3</sup>, Jeroen Molemaker<sup>2</sup>,**  
6 **Curtis Deutsch<sup>4</sup>, Anita Leinweber<sup>2</sup>**

7 <sup>1</sup>Southern California Coastal Water Research Project, Costa Mesa, CA <sup>2</sup>Department of  
8 Atmospheric and Oceanic Sciences, University of California Los Angeles, CA <sup>3</sup>Laboratoire  
9 d'Études en Géophysique et Océanographie Spatiale, Toulouse, France <sup>4</sup>School of Oceanog-  
10 raphy, University of Washington, WA

11 **Key Points:**

- 12 • The model reproduces the gradients of physical and biogeochemical properties that  
13 can be traced to the influence of coastal inputs.  
14 • The model reproduces nutrient enrichment via subsurface wastewater outfall plumes  
15 and riverine runoff.  
16 • The model is developed to disentangle natural variability, climate change, and local  
17 anthropogenic forcing.

---

Corresponding author: F. Kessouri and K. McLaughlin, [faycalk@sccwrp.org](mailto:faycalk@sccwrp.org) ;  
[karenm@sccwrp.org](mailto:karenm@sccwrp.org)

**Abstract**

The Southern California Bight (SCB), an eastern boundary upwelling system, is impacted by global warming, acidification and oxygen loss, and receives anthropogenic nutrients from a coastal population of 20 million people. We describe the configuration, forcing, and validation of a realistic, submesoscale resolving ocean model as a tool to investigate coastal eutrophication. This modeling system represents an important achievement because it strikes a balance of capturing the forcing by U.S. Pacific Coast-wide phenomena, while representing the bathymetric features and submesoscale circulation that affect the vertical and horizontal transport of nutrients from natural and human sources. Moreover, the model allows to run simulations at timescales that approach the interannual frequencies of ocean variability, making the grand challenge of disentangling natural variability, climate change, and local anthropogenic forcing a tractable task in the near-term. The model simulation is evaluated against a broad suite of observational data throughout the SCB, showing realistic depiction of mean state and its variability with remote sensing and *in situ* physical-biogeochemical measurements of state variables and biogeochemical rates. The simulation reproduces the main structure of the seasonal upwelling front, the mean current patterns, the dispersion of plumes, as well as their seasonal variability. It reproduces the mean distributions of key biogeochemical and ecosystem properties. Biogeochemical rates reproduced by the model, such as primary productivity and nitrification, are also consistent with measured rates. Results of this validation exercise demonstrate the utility of fine-scale resolution modeling in support of management decisions on local anthropogenic nutrient discharges to coastal zones.

**Plain Language Summary**

We applied and validated an ocean numerical model to investigate the effects of land-based and atmospheric nutrient loading on coastal eutrophication and its effects on carbon, nitrogen and oxygen cycles of the Southern California Bight, an upwelling-dominated marine embayment on the U.S. West Coast. The model is capable of high resolution, multi-year hindcast simulations, which permits mechanistic investigations to disentangle natural variability, climate change, and local human pressures that accelerate land-based and atmospheric nitrogen and phosphorus loads. The model performance assessment illustrates that it faithfully reproduces the monitored ocean state properties related to algal blooms, oxygen and pH, among others, that can be traced to the influence of human influences on land-based and atmospheric inputs of nutrients and carbon. The model performance assessment helps to constrain uncertainties in predictions to support ongoing conversations on approaches to mitigate climate change, including considerations of management of local nutrient and carbon inputs.

**1 Introduction**

Human-driven eutrophication has resulted in profound impacts to coastal ecosystems around the world. These impacts are arguably the best studied in estuaries and enclosed bays (e.g. Chesapeake Bay; Cerco and Cole (1993); Boesch et al. (2001)) and semi-enclosed seas such as the Baltic Sea (Savchuk & Wulff, 2007; Cederwall & Elmgren, 1990), the Mediterranean Sea (Arhonditsis et al., 2000), and the Gulf of Mexico (Justić et al., 2005; Laurent et al., 2018). To date, few investigations of coastal eutrophication have occurred in Eastern Boundary Upwelling systems (EBUS). While strong upwelling and vigorous surface currents would generally limit the extent to which coastal eutrophication could occur (Fennel & Testa, 2019), such investigations have also been limited by coupled physical biogeochemical numerical modeling approaches that can adequately resolve fine-resolution bathymetry and the complexities of submesoscale circulation (McWilliams, 2016; Dauhajre et al., 2019), while simulating a sufficient duration (several years) to distinguish oceanic versus terrestrial forcing. These submesoscale circulation features, including fine scale eddies and filaments < 5 km in horizontal resolution, strongly control the magnitude and variability of nearshore

68 upwelling and associated nutrient transport. Thus, high resolution, submesoscale-resolving  
69 numerical models are a necessary prerequisite for mechanistic modeling studies and source  
70 attribution of oceanic versus terrestrial drivers of coastal eutrophication in EBUS. Inad-  
71 equate modeling system and lack of numerical model validation have been identified as  
72 significant barriers to effective, evidence-based solutions to coastal eutrophication (Boesch,  
73 2019).

74 All the necessary ingredients are present to motivate a numerical modeling investigation  
75 of the role of coastal eutrophication in driving ocean acidification and deoxygenation in the  
76 Southern California Bight (SCB), a large marine open embayment found in the California  
77 Current System (CCS) on the U.S. Pacific Coast. First, the SCB is a biologically-productive  
78 region, and thus of high economic and ecological importance. Seasonal upwelling of nutrient-  
79 rich deep water maintains high rates of biological productivity over broad scales. At the  
80 same time, upwelling draws water masses that are naturally low in dissolved oxygen (DO),  
81 pH, and carbonate saturation state ( $\Omega_{Ar}$ ) onto the shelf and into the photic zone (Sutton et  
82 al., 2017). Second, the SCB has one of the most spatially comprehensive and longest-running  
83 coastal observational systems in the world. Several physical and biogeochemical variables  
84 are sampled regularly and extensively, creating an ideal setting for model-data comparisons.  
85 Third, the SCB is home to one of the most densely populated coastal regions in North  
86 America, where the discharges of primary or secondary treated wastewater from a population  
87 of 20 million people are released to the coastal zone via ocean outfalls, along with the urban  
88 and agricultural runoff from 75 rivers. These nutrient sources rival natural upwelling in  
89 magnitude (Howard et al., 2014), roughly doubling available nitrogen to nearshore coastal  
90 waters. Intensifying ocean acidification and deoxygenation and harmful algal blooms have  
91 motivated California policy makers to consider reducing anthropogenic nutrients as a climate  
92 change mitigation strategy (Ocean Protection Council, 2018), but wastewater treatment  
93 plant upgrades and non-point source controls would cost billions. A numerical modeling  
94 approach is needed to disentangle the effects of natural upwelling and climate change from  
95 anthropogenic nutrient loading from land-based and atmospheric sources.

96 To support such investigations, the regional oceanic model system (ROMS, Shchepetkin  
97 and McWilliams (2005)) coupled to the biogeochemical elemental cycling model (BEC,  
98 Moore et al. (2004)) has been recently adapted for the CCS (Renault, McWilliams, et  
99 al., 2020; Deutsch et al., 2020). A downscaled model domain was established, scaling from  
100 4 km (horizontal) resolution CCS-wide, one 1 km horizontal resolution grid covering Cal-  
101 ifornia nearshore, then to a 0.3 km grid in the Southern California Bight (SCB), where  
102 investigations of local anthropogenic inputs were focused. Modeling experiments investi-  
103 gating submesoscale transport (captured at model resolutions  $\leq 1$  km) have demonstrated  
104 an up to ten-fold increase in the magnitude of vertical N fluxes (Kessouri, Bianchi, et al.,  
105 2020) relative to mesoscale transport represented by a 4 km model (Sec. 2.2). Further-  
106 more, a finer horizontal resolution of bathymetry improves the representation of coastal  
107 currents, submesoscale circulation, and coast-offshore connectivity (Dauhajre et al., 2019).  
108 For this reason, investigations of coastal eutrophication are simulated at 0.3 km resolution.  
109 Simulations conducted at the 4 km ROMS-BEC model domain have been validated for  
110 regional-scale atmospheric forcing, physics, and biogeochemistry, including  $O_2$ , carbonate  
111 saturation state, primary productivity, and hydrographic parameters, demonstrating that  
112 the model captures broad patterns of critical properties in the CCS (Renault, McWilliams,  
113 et al., 2020; Deutsch et al., 2020). However, additional focused validation of nearshore,  
114 anthropogenically-enhanced gradients in nutrients, primary production, oxygen and pH in  
115 model simulations conducted at 0.3 km resolution are needed to gauge model utility to inves-  
116 tigate the role of coastal eutrophication in impacting ocean acidification and deoxygenation.

117 We employed this downscaled, submesoscale-resolving physical-biogeochemical model  
118 to investigate the effects of land-based and atmospheric nutrient inputs in driving coastal  
119 eutrophication and ocean acidification and deoxygenation. The aim of this manuscript is to:  
120 1) document the SCB ROMS-BEC model configuration, including the effects of land-based

121 and atmospheric inputs of nutrients and organic carbon, intended to support investiga-  
 122 tions of coastal eutrophication, and 2) present a validation of SCB ROMS-BEC simulations  
 123 against available observations, focusing on anthropogenically-enhanced gradients in nutri-  
 124 ent, primary production, oxygen, and pH.

## 125 **2 SCB coupled physical and biogeochemical model description, configu-** 126 **ration and forcing**

### 127 **2.1 Model description**

#### 128 *2.1.1 Ocean hydrodynamics*

129 The ocean hydrodynamics are modeled through the Regional Oceanic Modeling System  
 130 (ROMS) (Shchepetkin & McWilliams, 2005), a free-surface, terrain-following coordinate  
 131 model with 3-D curvilinear coordinates that solves the primitive equations with split-explicit  
 132 time steps. It contains state-of-art numerical algorithms that provide an accurate and stable  
 133 representation of physical processes down to scales of tens of meters, and allows for offline  
 134 downscaling of high-resolution sub-domains within larger domains. The offline downscaling  
 135 is based on the Orlanski scheme for the baroclinic mode (Marchesiello et al., 2001) and  
 136 a modified Fletcher scheme for the barotropic mode (Mason et al., 2010). The vertical  
 137 mixing in the boundary layer is resolved with a K-profile parametrization (W. G. Large et  
 138 al., 1994). The U.S. West Coast hindcast model has been successfully run over two decades  
 139 at 1 and 4 km horizontal resolution using high-resolution spatial and temporal atmospheric  
 140 forcing that resolves the effects of wind drop-off, the current feedback on the surface stress,  
 141 and high-frequency wind fluctuations (Renault, Molemaker, McWilliams, et al., 2016). We  
 142 further downscale to 0.3 km resolution to capture submesoscale processes and run the model  
 143 for 4 consecutive years between January 1997 and December 2000 for this study.

#### 144 *2.1.2 Biogeochemistry*

145 Ocean biogeochemical modeling approaches can have a broad range of complexities,  
 146 ranging from few functional groups (e.g. NPZD models, Fasham (1993)), to multiple bio-  
 147 geochemical cycles (e.g. C, N, O) and plankton functional groups. To provide a repre-  
 148 sentation of biogeochemical cycles, ROMS is dynamically coupled to the Biogeochemical  
 149 Elemental Cycling (BEC) model (Moore et al., 2004; Gruber, 2004; Gruber et al., 2011). A  
 150 schematic of BEC is shown in Fig. 1(b). BEC is a multi-element (C, N, P, O, Fe, Si) and  
 151 multiplankton model that includes three phytoplankton functional groups (picoplankton,  
 152 silicifying diatoms, and N-fixing diazotrophs), one zooplankton group, and dissolved and  
 153 sinking organic detritus. The remineralization of sinking organic material is parametrized  
 154 using Armstrong et al. (2001) formulae. As such, it models lower ecosystem trophic interac-  
 155 tions at an intermediate level of ecosystem complexity, relative to other marine ecosystem  
 156 models such as PISCES (Aumont & Bopp, 2006), NEMURO (Aita et al., 2007) and Plank-  
 157 TOM5 (Buitenhuis et al., 2012). Despite its relative simplicity, BEC exhibits good model  
 158 skill in predicting net primary production (Laufkötter et al., 2015), which is key to linking  
 159 coastal eutrophication to ocean acidification and deoxygenation.

160 The BEC model was expanded to provide a better resolution of N, C, alkalinity, Fe,  
 161 and O<sub>2</sub> cycling (Deutsch et al., 2020). These innovations include an improved nitrogen  
 162 cycle representation that tracks nitrate, nitrite, ammonium and nitrous oxide species, and  
 163 the microbially-mediated N transformations that connect them (Foster et al., 2011). Ni-  
 164 trogen loss to the sediment is parameterized according to the statistical diagenetic model  
 165 relationship of sediment denitrification, suggested in Middelburg et al. (1996). Water col-  
 166 umn denitrification is only active when oxygen concentrations fall below 5 mmol m<sup>-3</sup>. The  
 167 ecosystem is linked to a carbon system module that tracks dissolved inorganic carbon (DIC)  
 168 and alkalinity, and an air-sea gas exchange module that allows realistic representation of  
 169 dissolved gases (e.g. O<sub>2</sub>, CO<sub>2</sub> and nitrous oxide), based on the formulation of Wanninkhof

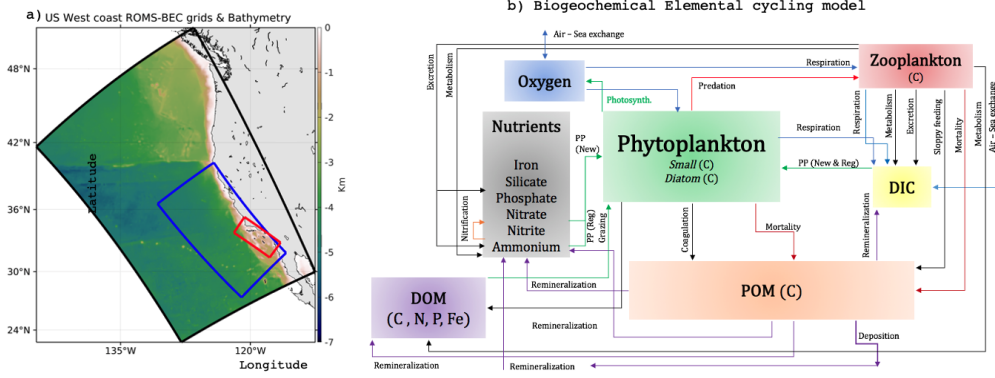


Figure 1: a) ROMS-BEC model configurations.  $dx = 4$  km is the black box,  $dx = 1$  km is the blue box,  $dx = 0.3$  km is the red box. Background is the topography from  $dx = 4$  km. b) Detailed schematic of the biogeochemical elemental cycling model. The schematic shows state variables (boxes) and biogeochemical rates and feedback (arrows).

170 (1992). Atmospheric deposition of dust from Mahowald et al. (2006) is used to implement  
 171 iron deposition, one of the mechanisms involved in the dissolved iron cycle (Deutsch et al.,  
 172 2020).

173 **2.1.3 Model configuration**

174 The SCB model domain extends along a 450 km stretch of the coast, from Tijuana to  
 175 Pismo Beach, and about 200 km offshore. This grid, shown in Fig. 1a), is composed of 1400  
 176 x 600 grid-points, with a nominal resolution of  $dx = 0.3$  km. The grid uses the stretching  
 177 parameters:  $\theta_s = 6$ ,  $\theta_b = 3$  and  $h_c = 250$  m, and a time step of 30 seconds. The model  
 178 configuration has 60  $\sigma$ -coordinate vertical levels using the stretching function described in  
 179 Shchepetkin and McWilliams (2009). Output is saved as 1-day averages.

180 The oceanic forcing of the 0.3 km domain originates from multi-level offline downscal-  
 181 ing. A 4 km simulation is initialized and forced at the open boundaries by a pre-existing  
 182 North-east Pacific-wide ROMS solution at 12 km resolution (Renault, McWilliams, et al.,  
 183 2020), initialized and forced on the boundaries by the global model Mercator Glorys2V3  
 184 (<http://www.myocean.eu>), and is run for the period 1995-2010, after a spin-up of 2 years.  
 185 A 1 km simulation is initialized and forced from the 4 km model, starting in October 1996  
 186 and ending in December 2007. The 0.3 km simulation is initialized and forced at its bound-  
 187 aries by the 1 km simulation starting from January 1997 and ending in December 2000. The  
 188 bathymetry used in this configuration comes from the Southern California Coastal Oceanic  
 189 Observation System (SCCOOS) 3 Arc-Second Coastal Relief Model Development (90 m  
 190 horizontal resolution).

191 The oceanic model is forced by hourly outputs from the atmospheric uncoupled Weather  
 192 Research and Forecast model (WRF06; Skamarock and Klemp (2008)). Using bulk formu-  
 193 lae (W. B. Large, 2006), WRF06 provides heat, surface evaporation, momentum and  
 194 atmospheric data and is run at 6 km resolution over a domain similar to the 4 km (Fig. 1  
 195 and used for Renault, Hall, and McWilliams (2016)), and includes a wind-current coupling  
 196 parameterization necessary to attain more realistic simulations of the oceanic eddy kinetic  
 197 energy (EKE) and circulation (Renault, Molemaker, McWilliams, et al., 2016; Renault,  
 198 Masson, et al., 2020).

199 Model simulations were conducted from 1997-2000, a period chosen to capture the  
200 effects of all three phases of the El Niño–Southern Oscillation (ENSO); it also captures the  
201 beginning of the "modern" state of point source management in the SCB, where several large  
202 Publicly Owned Treatment Plants (POTW) were in transition from primary to secondary  
203 treatment (we will refer to submarine point sources pipes from the treatment plants as  
204 "POTW" hereafter).

## 205 **2.2 Importance of the consideration of the submesoscale circulation**

206 Downscaling to  $dx = 0.3$  km permits the model to represent the ocean circulation that  
207 includes baroclinic and barotropic eddies and turbulence generated at the submesoscale  
208 (Capet, Campos, & Paiva, 2008). The submesoscale eddies increase the vertical variability  
209 of fluxes of biogeochemical tracers and allows more accurate representation of chemical and  
210 thus biological constituents. Figure 2(upper panel) shows the distribution and mean verti-  
211 cal flux of nitrate at 40 m from 3 different resolutions with the ROMS model (see section  
212 2.1.3). The submesoscale dynamics increase flux by more than one order of magnitude with  
213 more frequent structures (Fig. 2(bottom panels)) when increasing the resolution from 4  
214 km to 1 km and similarly another order of magnitude when increasing resolution from 1  
215 km to 0.3 km. Intensification of vertical flux of nitrate at the euphotic depth has previ-  
216 ously been shown in idealized models (Mahadevan, 2016; Lévy et al., 2012) and in realistic  
217 simulations (Kessouri, Bianchi, et al., 2020) in the central California upwelling system but  
218 has never been modeled in the SCB at this resolution. In fact, submesoscale eddies have  
219 been associated with increased productivity in the oligotrophic ocean (Mahadevan, 2016)  
220 and decreased productivity in the upwelling region (Kessouri, Bianchi, et al., 2020). Our  
221 submesoscale-resolving run at  $dx = 0.3$  km is an opportunity to quantify the complete bud-  
222 gets of nitrogen, dissolved oxygen, carbon and productivity using a realistic representation  
223 of urban anthropogenic inputs into the ocean.

224 Inclusion of submesoscale dynamics enables the active process of frontogenesis generated  
225 by mesoscale straining and strengthening from submesoscale instability (Capet, Klein, et al.,  
226 2008; Capet, Campos, & Paiva, 2008; Capet, McWilliams, et al., 2008). Oceanic fronts are  
227 a driver of significant nutrient supply to the upper ocean. They also have been recognised as  
228 areas of high biomass in many regions of the global ocean (e.g. Burke hales 1993 and others),  
229 as well as the nest of fisheries (e.g. (Galarza et al., 2009)). In our set of simulations, we  
230 show that the increased number of fronts and submesoscale instabilities promote intensified  
231 variability of nitrate as shown in figure 2, and heterogeneity at the subsurface chlorophyll  
232  $a$  maximum. However, surface phytoplankton biomass is only intensified if the timescale of  
233 the enrichment is sufficiently long and maintained in these small scale features. Modeling  
234 at this scale has allowed for accurate simulation of biogeochemical tracers as described in  
235 subsequent sections.

## 236 **2.3 Terrestrial and atmospheric forcing of freshwater, nutrients and carbon**

237 Model simulations were forced with a monthly time series of spatially-explicit input  
238 parameters (Fig. 3, upper), including freshwater flow, nitrogen, phosphorus, silica, iron,  
239 and organic carbon representing natural and anthropogenic sources (Sutula et al., 2021b).  
240 These data include POTW ocean outfalls and riverine discharges (1997-2017) and spatially-  
241 explicit modeled estimates of atmospheric deposition. POTW effluent data were compiled  
242 from permit monitoring databases and communication with sanitary agencies. Monthly time  
243 series of surface water runoff from 75 rivers are from model simulations and monitoring data  
244 (Sutula et al., 2021b). Direct atmospheric deposition is derived from the Community Multi-  
245 scale Air Quality (CMAQ) model (Byun et al., 2006), and follows the implementation of  
246 Deutsch et al. (2020). In this paper, we discuss in detail the formulation of the river and  
247 wastewater outfall inputs.

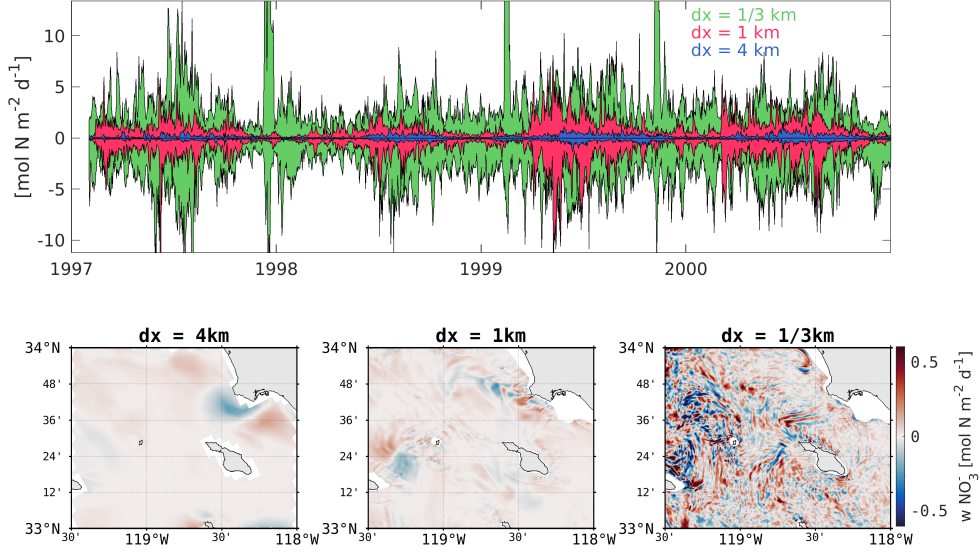


Figure 2: (Upper panel) Timeseries (1997-2001) of the vertical eddy flux of nitrate at 40 m depth calculated as follow:  $\overline{wN} = \overline{wN} + \overline{w'N'}$ , for region covering the entire Southern California Bight. The minimum and maximum values (i.e. the envelope) of the flux are shown in blue for the 4 km solution, in red for the 1 km solution and in green for the 1/3 km. (Lower) Snapshot of the vertical flux of nitrate in spring at 40 m off the coast of Palos Verdes that shows higher magnitudes and more variability when resolution increases.

248

## 2.4 Configuration of river and wastewater outfall forcing in the model

Ocean outfalls and coastal rivers are modeled as mass sources into the ocean (Fig. 3, upper). To accomplish this, we add explicit volume fluxes to the otherwise divergence-free flow in the ocean. The inclusion of these fluxes makes it possible to account for associated sources of tracers, while satisfying conservation laws. Specifically, our approach allows for the proper influx of fresh water in the ocean, without resorting to a ‘virtual salt’ flux, which is a common approach in larger scale ocean models (Kang et al., 2017). Since we explicitly include known volume fluxes for both rivers and outfall pipes, specification of tracer concentration is sufficient to correctly model the source terms. The tracer evolution equations that are used in ROMS are implemented by using control volumes (Shchepetkin & McWilliams, 2005) where for each tracer concentration  $C = C(x, y, z, t)$ ,

$$\frac{\partial \iiint C dV}{\partial t} = \iint u_n C dA. \quad (1)$$

where  $V = V(x, y, z, t)$  is the volume of the entire domain,  $u_n$  is the normal velocity into the volume and  $A = A(x, y)$  is the total area of grid cells source is being input. Additionally, we enforce mass conservation which implies;

$$\frac{\partial V}{\partial t} = \iint u_n dA. \quad (2)$$

249

250

251

252

In absence of rivers and outfalls, the flow is volume conservative, and the integral on the right hand side of Equation 2 is zero. Using Equations 1 and 2, it is easy to see that the mean concentration of a tracer can be lowered if the average concentration of the flux entering the control volume is less than the mean concentration in that volume. In this manner, fresh

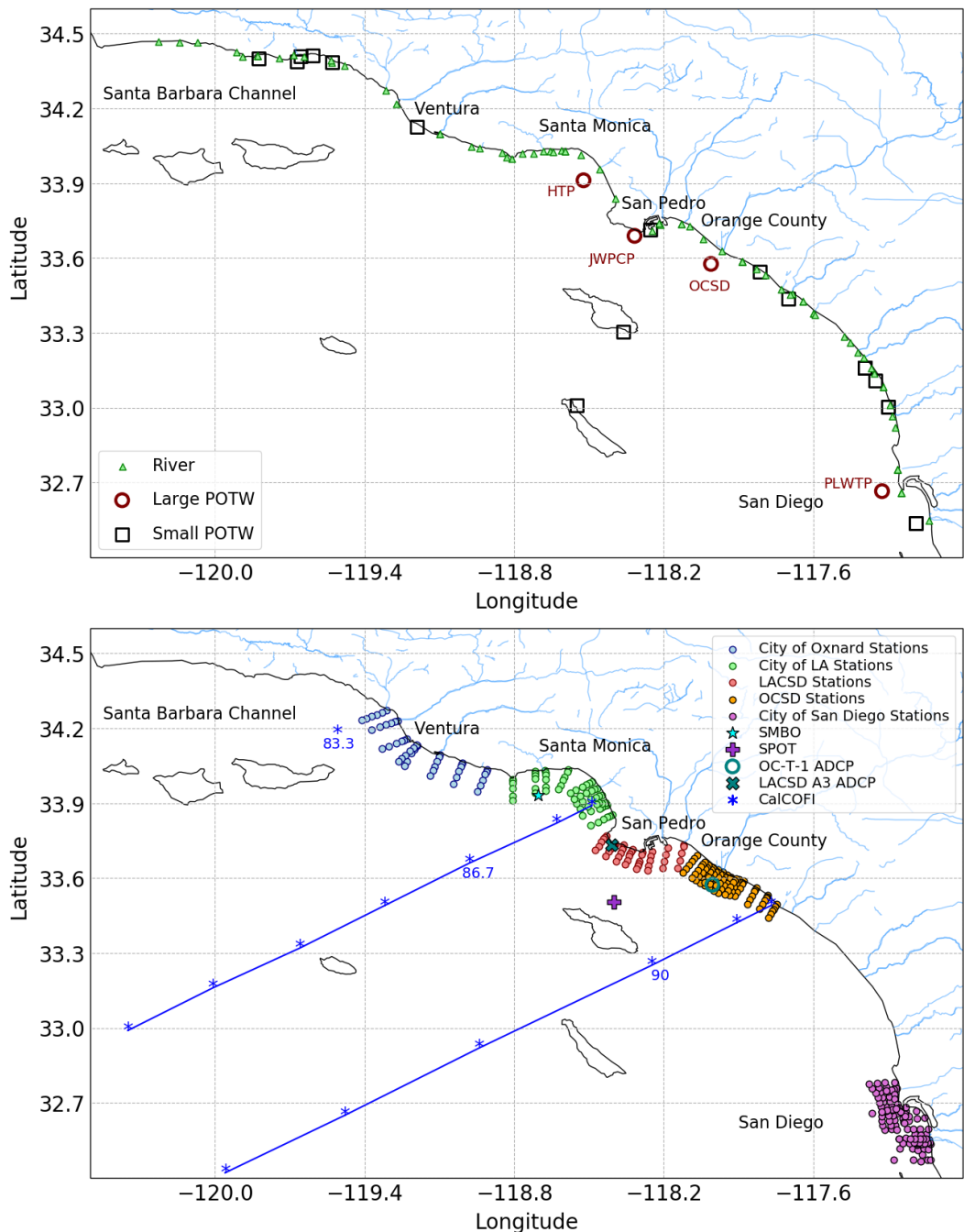


Figure 3: Upper panel: Location of rivers and POTW outfalls along the SCB. Lower panel: Monitoring stations used for the validation that include POTW quarterly monitoring surveys, CalCOFI seasonal observation program with given line number, Santa Monica Bay Observatory (SMBO) and San Pedro Oceanographic Timeseries (SPOT).

253 water rivers will lower the salinity of the water in which they enter. All 75 rivers and 23  
 254 POTW pipes that are considered in this study are implemented in this manner.

Each individual source is based on the following equation:

$$S(x, y, z, t) = \frac{W(x, y, z) Q_s(t) C_s(t)}{V_s} \quad (3)$$

255 With:

- 256  $S(x, y, z, t)$ : volume source of contaminant ( $\text{mmol m}^{-3} \text{ s}^{-1}$ ).  
 257  $W(x, y, z)$ : non-dimensional shape function (with values between 0 and 1).  
 258  $Q_s(t)$ : water volume flux from the source ( $\text{m}^3 \text{ s}^{-1}$ ).  
 259  $C_s(t)$ : concentration of the tracer C in the source water ( $\text{mmol m}^{-3}$ ).  
 260  $V_s$ : effective volume of the source ( $\text{m}^3$ ).  
 261

For each source,  $Q_s(t)$  and  $C_s(t)$  are prescribed as time series. The shape function  $W(x, y, z)$  distributes the tracer spatially and in the water column, representing non-resolved mixing and dilution effects. Its values represent the relative intensity of the *in situ* tracer injection, with values between 0 and 1. Tracer concentration C is distributed in the water column as  $C(x, y, z, t) = W(x, y, z)C_s(t)$ . The effective 3D volume of the source is calculated from the shape function  $W(x, y, z)$  as:

$$V_s = \iiint W(x, y, z) dV \quad (4)$$

where the integral is over the model domain. For convenience, we assume that  $W(x, y, z)$  can be separated into a horizontal shape function  $A(x, y)$ , multiplied by a vertical shape function  $H(z)$  (both non-dimensional and with values between 0 and 1), such that:

$$V_s = \iint A(x, y) dx dy \int H(z) dz = A_s H_s \quad (5)$$

262 Here,  $A_s$  represents the effective source surface area ( $\text{m}^2$ ), and  $H_s$  the effective source  
 263 thickness (m). The functions  $A(x, y)$  and  $H(z)$  are defined differently for POTW and rivers.  
 264 They are assumed to be fixed in time; a time-dependent generalization (for example to  
 265 mimic variations in the depth of the POTW buoyant plume) is straightforward. For POTW  
 266 inputs, at each main diffuser, the horizontal distribution  $A(x, y)$  of the source is shown in  
 267 Fig. S1. This method of weighting the plume in different cells allows the effluent to be  
 268 properly diluted vertically and horizontally at this resolution and prevents the model from  
 269 developing numerical instabilities.

Each large treatment plant has specialized outfall configurations that are taken into account for representation in the model (Fig. S1). The flow is divided in two at Hyperion Treatment Plant (HTP) located 6km off Marina Del Rey (Santa Monica Bay) (Fig. S1A) and Point Loma Wastewater Treatment Plant (PLWTP) in San Diego coast (Fig. S1D) to account for their Y-shaped diffuser, partitioning 50% of the flow to each diffuser. Orange County Sanitation District (OCSD) located 6km off Huntington Beach (Fig. S1C) has one flow through its L-shaped diffuser. Joint Water Pollution Control Plant (JWPCP) in Palos Verdes shelf (Los Angeles) (Fig. S1B) has three diffusers, the Y-shape northern typically discharges 17.5% of the flow for each leg of the Y-diffuser, and the southern L-shape diffuser discharges 65% of the flow. The vertical profile of the POTW sources is defined by a Gaussian function centered at a height  $z$  above the bottom ( $h_b$ ), to mimic a buoyant plume, so that  $H(z)$  is given by:

$$H(z) = e^{-z^2/d_s^2} \quad (6)$$

- 270 Where  $z = -h_b + h_s$ , with  
 271  $h_b$ : bottom depth (m).  
 272  $h_s$ : depth of the buoyant plume above the bottom (m).

273  $d_s$ : vertical scale of the POTW plume (m).  
 274 We further assume  $h_s = 20$  m and  $d_s = 10$  m, as in Uchiyama et al. (2014).

275 We distribute the SCB rivers on one horizontal grid point (0.3 km wide), where we  
 276 assume  $A(x, y) = 1$ , and similarly distribute the source vertically, with the Gaussian function  
 277 centered at the surface.  $h_s$  here is simply the water column depth to put the maximum input  
 278 at the surface. Because in ROMS the thickness of vertical grid cells varies in time, to ensure  
 279 tracer conservation the calculation of the input source volume  $V_s$  must be done at each time  
 280 step, even in the case of a time-independent source shape function  $W(x, y, z)$ . Effectively,  
 281 only  $H_s = H(z)$  needs to be recalculated at each time step.

### 282 3 Model performance assessment approach

283 The conceptual approach for model performance assessment is comprised of three com-  
 284 ponents, addressing different aspects of skill assessment: 1) statistical comparison of model  
 285 output to observational data for state variables by region and season; 2) comparison of model  
 286 output to observational data for biogeochemical rates; 3) evaluation of model behavior com-  
 287 pared to expected biogeochemical dynamics for coastal zones. Comparison of model output  
 288 to observational data by region and season is designed to document model skill at reproduc-  
 289 ing the statistics (e.g. mean values and variability) of ocean physical and biogeochemical  
 290 parameters at the spatio-temporal scales more relevant for evaluating human impacts on the  
 291 coastal environment. Comparison of model output to observational data for biogeochemi-  
 292 cal rates assures that model is capturing the appropriate transformations in nutrients and  
 293 carbon that structure the ecosystem response to eutrophication. Finally, the evaluation of  
 294 model behavior compared to the expected physical and biogeochemical dynamics for coastal  
 295 zones is a more qualitative evaluation of model performance to document that the model  
 296 broadly reproduces oceanographic phenomena in a way that reflects our understanding of  
 297 nearshore ocean environments.

#### 298 3.1 Description of Observational Datasets

##### 299 3.1.1 Ship-Based Ocean Monitoring

300 The SCB is home to a suite of long-running monitoring programs that make it one of  
 301 the best observed coastal ecosystems in the world (3, lower). Among them, the Califor-  
 302 nia Cooperative Oceanic Fisheries Investigations (CalCOFI) program (McClatchie, 2016),  
 303 initiated in the 1950s, samples the SCB quarterly each year, collecting hydrographic and  
 304 biogeochemical measurements in coordination with the Southern California Coastal Ocean  
 305 Observing System (SCCOOS). These observations are augmented nearshore by quarterly  
 306 surveys of nearshore water column and benthic parameters conducted collaboratively since  
 307 1990 by POTW agencies as a part of their regulatory monitoring requirements (Howard  
 308 et al., 2014; McLaughlin et al., 2018; Booth et al., 2014; Nezlin et al., 2018). These pro-  
 309 grams provide good temporal and geographical coverage of both the offshore (CalCOFI) and  
 310 nearshore (POTW) areas, coinciding with the model period, and include publicly available  
 311 water quality data for targeted sites measured quarterly. We validated model output against  
 312 observed temperature, dissolved oxygen, nitrate, ammonium, chlorophyll, carbon-system  
 313 parameters (pH and aragonite saturation state), primary production, and nitrification.

314 *In situ* measurements have inherent uncertainty, due to a combination of measurement  
 315 sensitivity and sampling frequency and intensity, making them an imperfect “truth” with  
 316 which to compare to model output. However, this uncertainty is not the same for all param-  
 317 eters. Both temperature and dissolved oxygen are collected using high resolution probes,  
 318 though the two programs used in this study incorporate slightly different calibration pro-  
 319 tocols for dissolved oxygen, lending greater confidence to data-model comparisons for these  
 320 datasets. Chlorophyll is measured on discrete bottle samples in the CalCOFI program,  
 321 a high quality measurement, but inferred from *in situ* fluorescence measurements in the

POTW monitoring program, adding uncertainty to these measurements. Nitrate and ammonium concentrations are measured on discrete bottle samples for both programs, but the detection limits are more sensitive in the CalCOFI program. Furthermore, nutrients are not measured with the same sampling density in POTW monitoring programs as sensor data. Similarly, primary production is measured at a subset of locations in the CalCOFI program and as a short-term special study in Southern California Bight Regional Marine Monitoring Program (Bight Program). Details on measurements and sample collection protocols for the CalCOFI program can be found on their website (<https://calcofi.org> ; McClatchie (2016)) and for the POTW monitoring programs in Howard et al. (2014). Figure 3 shows a map of all monitoring stations used in this study. The repository of data can be found in Kessouri, McLaughlin, et al. (2020).

### 3.1.2 High Frequency Radar and Acoustic Doppler Current Profilers

High Frequency Radar (HF) data from the database of the University of California, San Diego (<https://hfrnet-tds.ucsd.edu/thredds/catalog.html>) provides surface currents along the west coast of the United States, including the SCB. Seasonally averaged data from 2012-2020 were used to analyze trends of surface currents in the Bight compared to the model. Acoustic Doppler Current Profilers (ADCP) provide current data in the water column. ADCP measurement data from Orange County Sanitation District (OCSD) for the period June 1999 to June 2000 and Los Angeles County Sanitation District (LACSD) during November 2000 to June 2007 were used to validate vertical profiles of currents.

### 3.1.3 Remote sensing observations

Satellite ocean color measurements for chlorophyll were used to characterize horizontal gradients at finer scales than possible with the ship-based monitoring. We use monthly averaged surface chlorophyll concentration from the period 1997 to 2000 derived from the SeaWiFS sensor at 4 km spatial resolution. Large gaps in the dataset can occur because of dense cloud cover that occurs in late spring and early summer. The products of the Vertically Generalized Production Model (VGPM) net primary production algorithm (Behrenfeld & Falkowski, 1997) were also considered for this validation. Despite the limitations, satellite data provide a valuable representation of the spatial distribution of chlorophyll, temperature, and primary production at seasonal scales over the region.

## 3.2 Performance Statistics

Our approach to a statistical assessment of agreement between model predictions versus observations reflect the fact that the hydrodynamic model, under the influence of realistic forcings (e.g. wind fields) and without data assimilation, develops its own intrinsic variability in circulation, e.g. submesoscale eddies (McWilliams, 2007). The resulting modeled state variables would not necessarily overlap with observations on a point-by-point basis, but would be comparable to observations when averaged over appropriate spatio-temporal scales. We assessed a suite of statistics and metrics, following the methodology of Allen et al. (2007), to assess how well the model reproduces the magnitude and gradients of selected state variables, whether the model agreement has an apparent bias, and how well the model reproduces natural variability. We calculated six metrics, defined in the following, where  $N$  is the total number of appropriate observational data,  $D$  represents each individual observational datum,  $\bar{D}$  is the mean of the observational data,  $M$  is the model estimate representing an observation, and  $\bar{M}$  is the mean of the model estimate. The metrics considered include:

The Pearson correlation coefficient, reflecting the degree of linear correlation between the observed and model variable, and the statistical significance (p-value) of this correlation:

$$r_{xy} = \frac{\sum_{n=1}^N (D_n - \bar{D})(M_n - \bar{M})}{\sqrt{\sum_{n=1}^N (D_n - \bar{D})^2} \sqrt{\sum_{n=1}^N (M_n - \bar{M})^2}}; \quad (7)$$

The Cost Function (CF), which gives a non-dimensional value indicative of the “goodness of fit” between two sets of data, quantifying the difference between model results and measurement data:

$$CF = \frac{1}{N} \sum_{n=1}^N \frac{|D_n - M_n|}{\sigma_D} \quad (8)$$

366 where  $\sigma_D$  is the standard deviation of the observations;

The Percentage Bias (PB) (the sum of model error normalized by the data):

$$PB = \frac{\sum (D - M)}{\sum D} * 100; \quad (9)$$

The Ratio of the Standard Deviations (RSD):

$$RSD = \frac{\sigma_D}{\sigma_M} \quad (10)$$

367 where  $\sigma_M$  is the standard deviation of model outputs;

The Nash-Sutcliffe Model Efficiency (ME) (Nash & Sutcliffe, 1970), a measure of the ratio of the model error to the variability of the data:

$$ME = 1 - \frac{\sum (D_n - M_n)^2}{\sum (D - \bar{D})^2}; \quad (11)$$

And the two-sample t-test, or Welch’s t-test (Welch, 1947; Derrick et al., 2016):

$$H = (\bar{D} - \bar{M}) / \sqrt{\frac{\sigma_D^2}{N} + \frac{\sigma_M^2}{N}}. \quad (12)$$

368 We score the model performance following Table 1 per the methodology of Allen et al.  
369 (2007).

Statistic	Excellent	Good	Reasonable	Poor
Cost Function (Moll & Radach, 2003)	<1	1-2	2-3	>3
Nash Sutcliff Model Efficiency (Nash & Sutcliffe, 1970)	>0.65	0.65-0.5	0.5-0.2	<0.2
Percentage Bias (Maréchal, 2004)	< 0.1	0.1-0.2	0.2-0.4	> 0.4
H (Welch, 1947)	0			1
Correlation Coefficient	1-0.9	0.9-0.8	0.8-0.6	<0.6
p-value	<0.05			>0.05
Ratio of Standard Deviations	1-0.9, 1-1.1	0.9-0.8, 1.1-1.2	0.8-0.6, 1.2-1.4	<0.6, >1.4

Table 1: Model performance

## 370 4 Model performance assessment findings

### 371 4.1 Ocean circulation

372 The SCB is situated at the confluence of water masses from the subarctic Pacific via the  
 373 California Current, and from the eastern tropical North Pacific via the California Undercur-  
 374 rent, which all interact with the local topography, the coast, and the atmosphere to sustain  
 375 variability in circulation on inter-annual, seasonal, and intraseasonal time scales (Dong et  
 376 al., 2009; Bograd et al., 2015). The effects of this variability in circulation has profound  
 377 consequences for coastal ocean biogeochemistry (Gruber et al., 2011; Bograd et al., 2015;  
 378 Nagai et al., 2015; Nezlin et al., 2018), and is therefore critical that the model accurately  
 379 simulates spatial and temporal variability in circulation patterns.

380 Figure 4 shows the hydrodynamic characteristics of the SCB in the model compared to  
 381 data. In the northern SCB, the model shows similar qualitative and quantitative patterns  
 382 for the horizontal circulation compared to HF data (Fig. 4(a)-(b)) and as seen in Dong et  
 383 al. (2009). The circulation in the SCB is characterized by northward currents in the first 20  
 384 km of the coast and cyclonic circulation in the middle of the SCB that is stronger in summer  
 385 and weaker in winter. The model successfully reproduces the circulation of observed current  
 386 patterns with similar current magnitudes. The intensity of the northward coastal branch of  
 387 the current is on average about  $0.15\text{-}0.3\text{ m s}^{-1}$  in summer versus  $0.05\text{-}0.15\text{ m s}^{-1}$  in winter.  
 388 The offshore southward branch is generally about  $0.3\text{ m s}^{-1}$  all year round (Fig. 4(a)-(b)).  
 389 The dominant current in the coastal band (15 km from coast) of the SCB flows northward,  
 390 and follows the topography along isobaths on the shelf (Fig. 4(g)-(h)).

391 The simulated June 1999-June 2000 variability of the current in depth is shown in the  
 392 vertical profiles extracted off the coast of Palos Verdes and Orange county compared to the  
 393 ADCP data at the same locations (Fig. 4(c)-(f)). The location of both of these profiles are a  
 394 few kilometers from the continental slope and therefore capture a suite of physical processes,  
 395 including mesoscale and submesoscale eddies, fronts, jets, and tides (Capet, McWilliams,  
 396 et al., 2008; Kim et al., 2011; Dong et al., 2009). The model generally reproduces the  
 397 means and range of the variability shown in these close to shore horizontal currents, which  
 398 demonstrates that ROMS at  $dx = 0.3\text{ km}$  resolution captures the submesoscale variability  
 399 described in Sec. 2.2.

400 In the northern SCB, cyclonic vortices are generated inside the Santa Barbara Chan-  
 401 nel (Fig. 4(i)) when the northward current that flows along the Ventura coast meets the  
 402 eastern side of the Channel Islands, with higher intensity in summer (Fig. 4(a) versus (b))  
 403 (Winant et al., 2003). Submesoscale eddies are particularly prominent inside the Santa  
 404 Barbara Channel. Persistent cyclonic eddies drive an upward doming of isopycnals (Fig.  
 405 4(j)) (McGillicuddy Jr, 2016), which supplies nutrients to the euphotic layer. The model  
 406 correctly reproduces this vertical transport, described in Brzezinski and Washburn (2011),  
 407 and the high concentrations of nitrate and other nutrients in the upper layers of the Santa  
 408 Barbara Channel, which is further detailed in Section 4.3.1.

409 In the central and southern SCB, the model successfully captures flow regimes around  
 410 the large POTW outfalls, indicating that it can appropriately represent the dispersal of  
 411 wastewater plumes in these regions. In the Santa Monica and San Pedro Bays, topography  
 412 drives the circulation of currents inside the Bays, converging back to the main current  
 413 offshore (Fig. 4(g)-(h)). On top of the Hyperion and JWPCP outfalls (in the Santa Monica  
 414 Bay and offshore of the Palos Verdes peninsula, respectively), the current is mostly south-  
 415 eastward. Near the OCSO outfall, the current direction varies in winter between south-  
 416 eastward and north-westward, but is primarily southward in summer (Fig. 4(a)-(b), (e)-  
 417 (f)). At the PLWTP outfall, the current is narrow, with a dominant south-eastern direction,  
 418 parallel to the coast, demonstrated by both model and HF radar data.

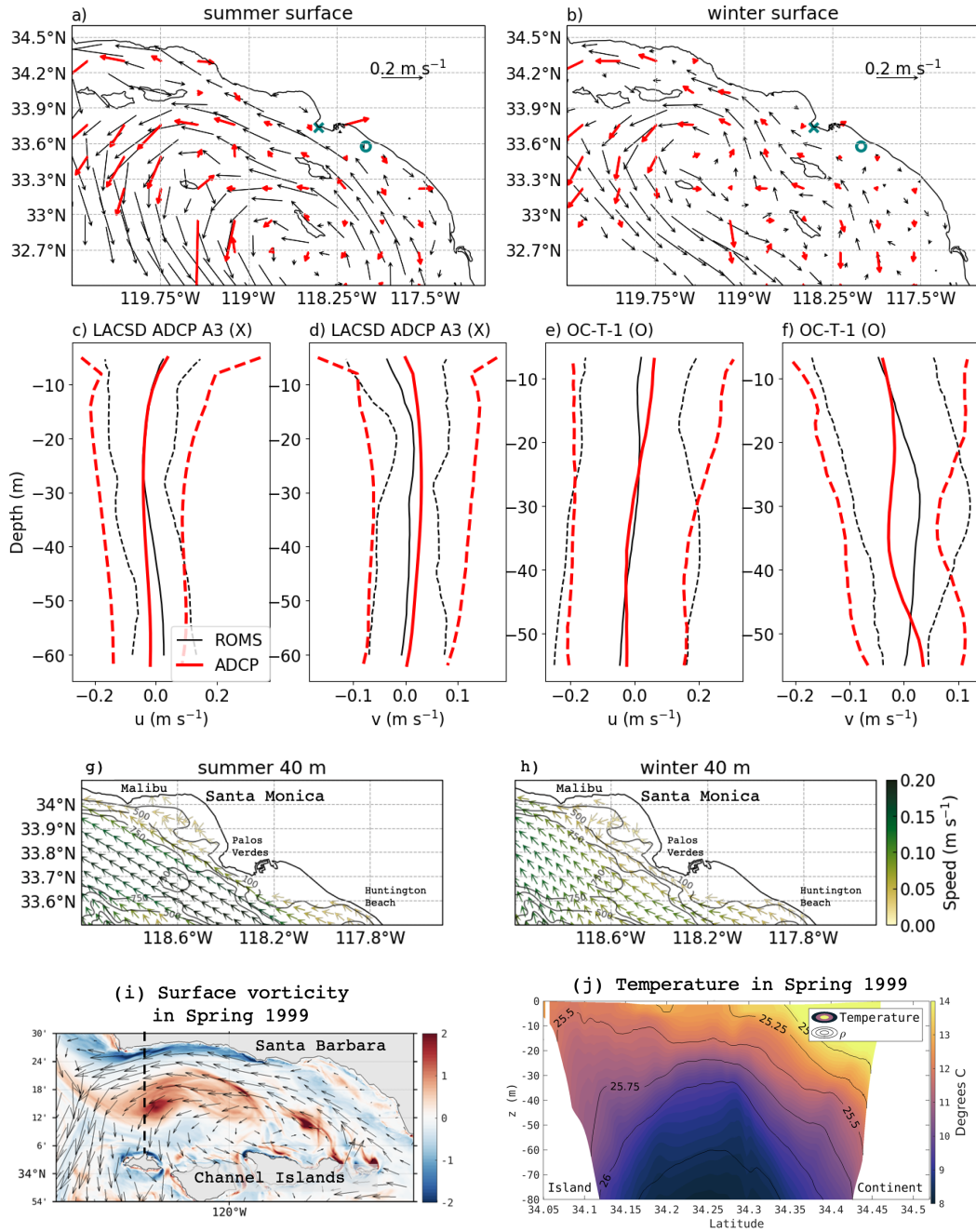


Figure 4: a) Mean surface currents in the Southern California Bight from HF data during 2012-2020 (thick red arrows) and model during 1999-2000 (black arrows) in summer and b) winter. c)-f) Vertical profiles of horizontal velocity components from ADCP instruments (thick red lines) and model (thinner black lines). The two dashed lines indicate the 5th and 95th percentile current values. c)-d) ADCP data come from the LACSD mooring A3 stationed at the teal ‘X’ in a)-b) and e)-f) come from the OCSD mooring OC-T-1 located at the teal ‘O’. g) Mean model current direction and speed (colored) at 40 m depth with bathymetry contoured in summer and h) winter. i) Surface model vorticity normalized by  $f$  in spring in Santa Barbara Channel showing cyclonic eddies. j) Cross-section of temperature and density isopycnals as drawn by the dashed line in (i) from model to show eddy-driven uplifting of the isopycnals in the center of Santa Barbara Channel.

419  
420

## 4.2 Vertical gradients and seasonal variability of temperature and the mixed layer depth

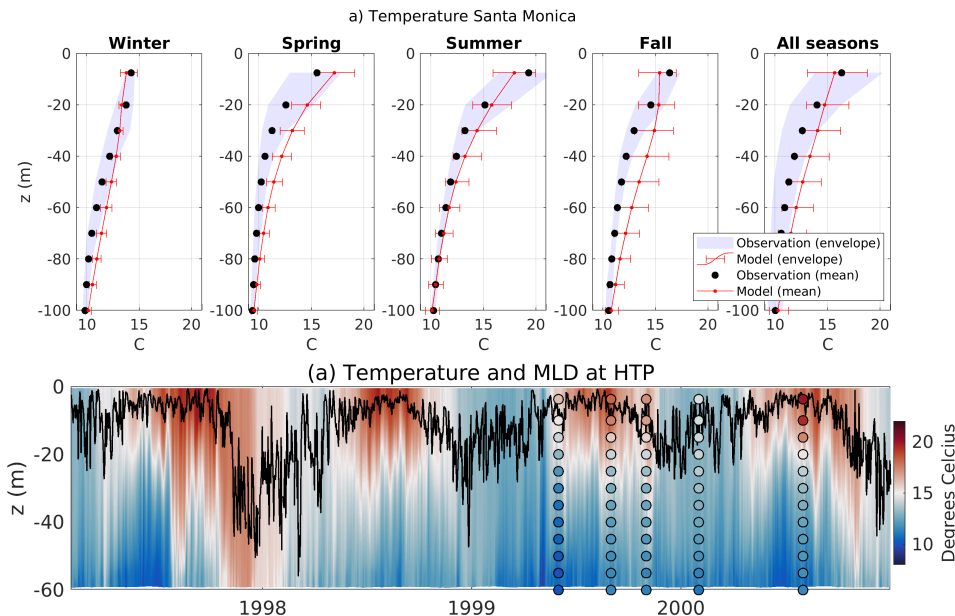


Figure 5: (a) Average seasonal profiles of temperature in the Santa Monica Bay. The red lines and red bars show the spatio-temporal mean and the variability from the model respectively. The black dots and the gray shading show the spatio-temporal mean and the variability from *in situ* data (City of LA stations), respectively. (b) Hovmöller diagram of temperature at the location of the Hyperion POTW outfall (HTP) in the Santa Monica Bay issued from the model. The black line shows the simulated time-series of mixed layer depth. The deepest mixing occurs during El Niño 1998 ( $>40$  m). Colored dots are average concentrations from *in situ* measurements.

421  
422  
423  
424  
425  
426  
427  
428  
429  
430  
431  
432  
433  
434

The model successfully reproduces the three-dimensional and seasonal variability of physical tracers, here exemplified by temperature. Temperature is the parameter in which we have the highest confidence in the observational record, because observations are abundant, and sensors are accurate and precise, regularly calibrated, and with negligible drifts. The greatest source of observational uncertainty is temporal under sampling and also to model biases (e.g. from atmospheric forcing, wind or shortwave detailed in Renault, McWilliams, et al. (2020)). Quantitative statistical analysis indicates that model performance is ‘*excellent*’ or ‘*good*’ for nearly all metrics for all regions and seasons (see Table 2). The lowest performance of the model is characterized as ‘*reasonable*’ for the certain sub-regions (Palos Verdes, Orange County, and San Diego) in the spring and fall (Palos Verdes only) (see Supporting Information Table S2). As noted above, this may be due to under-sampling during these months, which can be highly variable because the region is shifting between a well-mixed to a more stratified ocean regime. Detailed information on the other sub-regions and their statistical comparison can be found in the Supporting Information Tables S1 to S4.

435  
436  
437  
438  
439  
440

Following common practices (Montégut et al., 2007), we define the mixed layer depth (MLD) as the depth at which the temperature decreases from its surface value by more than  $0.2^{\circ}\text{C}$ . On average, the MLD deepens from the coast to offshore, and varies with season (e.g. in Santa Monica Bay in Fig. 5b). The model successfully simulates the seasonal cycle of MLD along the coast. For example, the model recreates seasonal deepening of the mixed layer calculated in the observations in the Santa Monica Bay to greater than 16-20 m depth

441 (the typical depth of the upper signature of the POTW plumes, see the Section 4.3.2) nearly  
 442 every winter (black line in the Fig. 5b)). The model reproduces interannual variability in  
 443 MLD under the influence of El Niño-Southern Oscillation (ENSO, hereafter referred to as  
 444 El Niño) (e.g. the period from fall 1997 to spring 1998 in Fig. 5b)) the MLD reached 40  
 445 m. We show that during winter of an El Niño year, the entire water column of the SCB is  
 446 warmer than on average, and temperature is homogeneous, varying between 15.5 and 17°C  
 447 (Fig. 6a). In the open ocean, during El Niño, with warmer upper layer than regular winters,  
 448 the model shows good performance to reproduce the deepening of the seasonal thermocline  
 449 (>120 m) and deeper MLD (>50 m) (e.g. off Santa Monica bay in Fig. 6a) and b)). Regular  
 450 winter shows a homogeneous upper layer of < 14°C temperature, and a mixed layer located  
 451 at 18-20 m in the coastal region and 40-60 offshore. The surface ocean is colder around the  
 452 Channel Islands (SST<12°C) (see Fig. 19). In the open ocean, the model reproduces the  
 453 de-stratification with deepening of the thermocline to about 70m and a MLD at about 40m  
 454 (Fig. 6c) and d)). In summer, stratification is the strongest, reflecting an intense vertical  
 455 temperature gradient, and the MLD (both in the model and in the observations) is found  
 456 few meters below the surface (approximately 10 m). Temperature varies rapidly from more  
 457 than 20°C at the surface in the southern domain (16-17°C in the northern domain) to less  
 458 than 12°C at 50m depth over the entire SCB (see later in Fig. 19). In the open ocean,  
 459 the model succeeds in reproducing the stratification that brings the seasonal thermocline to  
 460 50m and the MLD to 15m (Fig. 6c) and e)). These patterns of variability in temperature  
 461 are consistent with regional observations of El Niño in the SCB (Todd et al., 2011).

### 462 4.3 Dissolved Inorganic Nitrogen

#### 463 4.3.1 *Spatial patterns and seasonality of nitrate*

464 Nitrate observations are only available in the offshore CalCOFI dataset, so only broad  
 465 regional patterns in nitrate concentration can be validated. There is a clear seasonality of  
 466 nitrate, where surface concentrations are higher in spring and summer, and decrease in fall  
 467 and winter (Fig. 7). The model reproduces the average seasonal patterns observed in the  
 468 *in situ* nitrate data across multiple regions. The model also captures along-shore variability  
 469 in coastal nitrate concentrations, reproducing values greater than 25 mmol N m<sup>-3</sup> off Santa  
 470 Barbara, 20 mmol N m<sup>-3</sup> off Los Angeles, and 15 mmol N m<sup>-3</sup> off San Diego.

471 The model also reproduces observed patterns in the depth of the nitracline (Mantyla et  
 472 al., 2008; Nezlin et al., 2018), which tends to follow sloping density surfaces in the region.  
 473 These patterns include: the high values at the euphotic depth (~50m below the surface)  
 474 along the Santa Barbara coast in spring; the doming of the nitracline in the center of the  
 475 Santa Barbara Channel (Fig. 7b); the 20 to 30 m deep nitracline along the Los Angeles  
 476 coast; and the deepening of the nitracline from about 30 m at the coast to more than 60  
 477 m offshore in San Diego. In the offshore region of the SCB, the model is consistent with  
 478 observations showing high nitrate (>20 mmol N m<sup>-3</sup>) around the Channel Islands (not  
 479 shown) compared to less than 5 mmol N m<sup>-3</sup> farther offshore. This pattern is strongest in  
 480 winter and summer, when the offshore regions are particularly oligotrophic (surface NO<sub>3</sub><sup>-</sup> <  
 481 1 mmol m<sup>-3</sup>) throughout the SCB.

#### 482 4.3.2 *Vertical gradients and seasonal variability of ammonium*

483 Ammonium concentrations above a natural background concentration of 1 mmol N  
 484 m<sup>-3</sup> are indicative of POTW wastewater plumes. The model reproduces the observed  
 485 average vertical profile of ammonium in Santa Monica Bay, falling within the range of  
 486 observed variability (Fig. 8a). Similar figures for other regions are shown in the Supporting  
 487 Information (Fig. S6-Fig. S9). All regions show a similar maximum concentration between  
 488 30 to 45 m below the surface, in all seasons. The highest concentrations are seen in summer,  
 489 when stratification is stronger, while lower concentrations in winter likely reflect increased  
 490 dilution by seasonal mixing from the deepening of the mixed layer (Fig. 8b). Near ocean

Santa Monica: Temperature

	H	Correlation Coefficient	p-value	Cost Function	Percentage Bias	Ratio of Standard Deviations	Nash-Sutcliffe Model Efficiency	Number of observations
Winter	0 E	0.96 E	7E-06 E	0.05 E	-0.04 E	1.10 G	0.81 E	716
Spring	0 E	0.98 E	8E-07 E	0.10 E	-0.10 G	0.78 R	0.51 G	716
Summer	0 E	0.97 E	9E-06 E	0.04 E	-0.02 E	1.07 E	0.93 E	712
Fall	0 E	0.89 G	3E-06 E	0.09 E	-0.08 E	0.98 E	0.51 G	718
All Seasons	0 E	0.95 E	3E-05 E	0.08 E	-0.07 E	1.02 E	0.73 E	2862

Table 2: Statistical comparison between *in situ* data and model outputs for temperature profile in Santa Monica Bay (City of LA stations). Letters next to numbers indicate model performance: E = Excellent, G = good, R = reasonable, P = Poor.

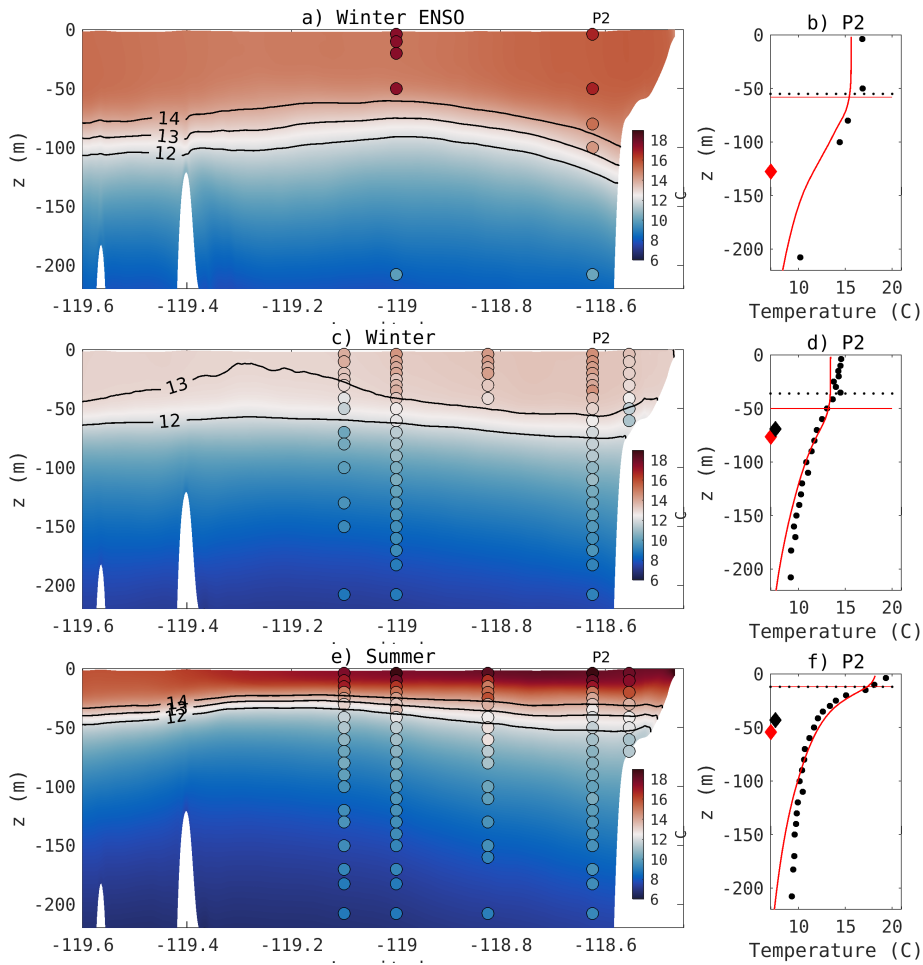


Figure 6: (a) Cross section of average temperature following line 86.7 from CalCOFI monitoring stations during an El Niño winter (12/1997 to February 1998). (b) Profile at station P2. Black dots are CalCOFI *in situ* data, red line is the simulated profile. The horizontal line is the MLD (black is CalCOFI, red is simulated). Diamonds (black is CalCOFI, red is simulated) is the depth of the maximum gradient to estimate the depth of the seasonal thermocline at 12°C. (c-d) are similar to (a-b) for average winter, and (e-f) are for average summer.

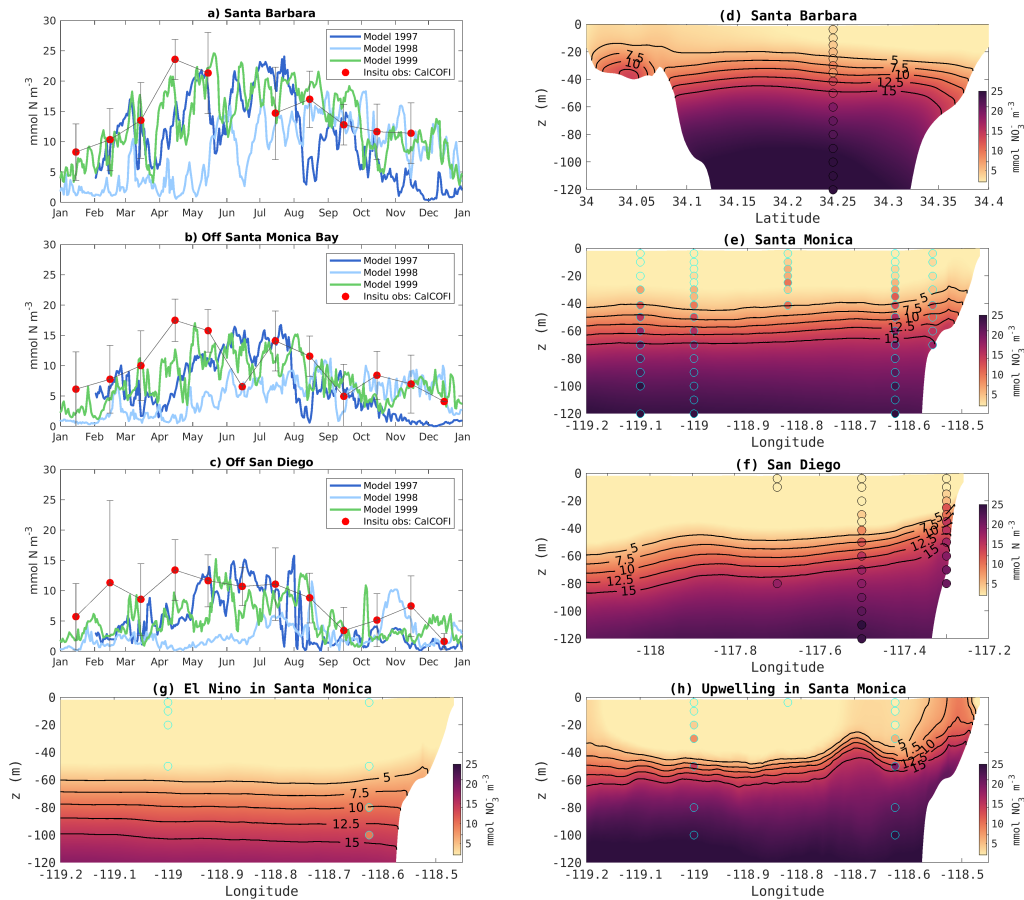


Figure 7: (a-c) Time series of nitrate concentration at 50 m depth in three different locations of the SCB: (a) is near the center of Santa Barbara Channel, (b) is offshore the Santa Monica Bay, and (c) is offshore San Diego. Model outputs are represented by the lines for three different years, with the dots showing mean values from *in situ* measurement from CalCOFI, and gray bars the standard deviation from the mean. The time-series show prominent interannual variability in addition to seasonal variability. While the years 1997 and 1999 show similar nitrate distributions, the El Niño period between the end of 1997 to 1998 is significantly different, showing nearly uniform concentrations between November 1997 through May 1998. This is caused by the deepening of the thermocline during El Niño, which depresses the nutricline. (d-f) Cross sections showing the average springtime nitrate concentration in (d) the Santa Barbara region (e) the SM region, and (f) the SD region. Background are model outputs and dots are CalCOFI *in situ* measurements. Model and *in situ* data agree on the vertical and seasonal patterns in the three regions. They highlight the main differences in these three regimes, that reside in the shoaling of the nitraclines, closer to the surface in the Santa Barbara Channel and deeper in the southern waters. (g-h) Comparison of nitrate concentrations during (g) winter El Niño (January-March 1998) and (h) during an upwelling event (the first week of May 1999) to illustrate the capacity of the model (versus *in situ* CalCOFI data) to simulate the vertical change of the nitracline during these specific events.

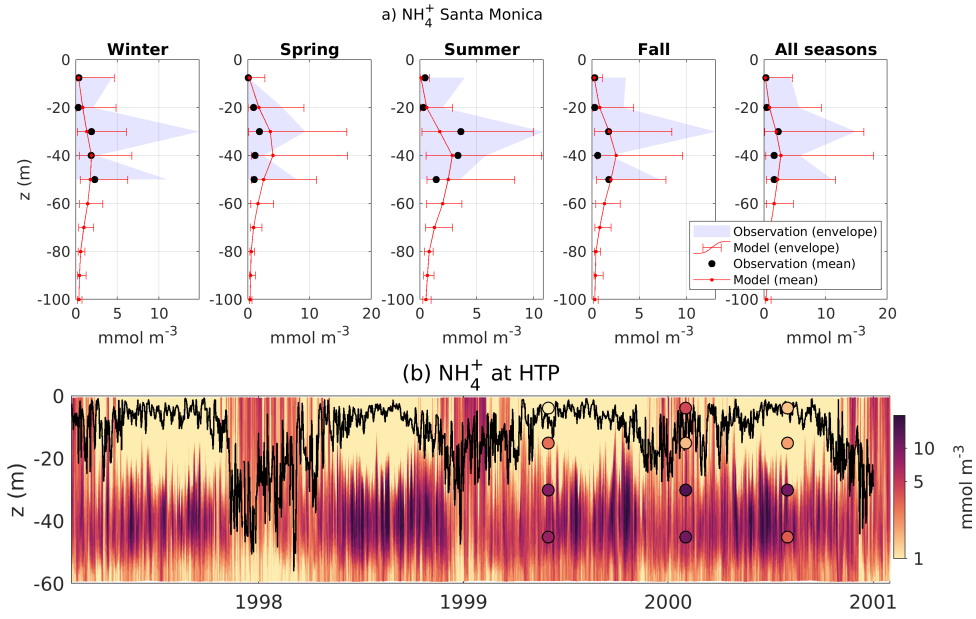


Figure 8: As for Fig. 5, but for ammonium concentration. These profiles are showing agreement on intensity, seasonality and shape of the vertical profile with exceptionally high concentrations at mid-depth.

Santa Monica: Ammonium

	H	Correlation Coefficient	p-value	Cost Function	Percentage Bias	Ratio of Standard Deviations	Nash-Sutcliffe Model Efficiency	Number of observations
Winter	0 E	0.94 E	0.06 P	0.54 E	0.24 R	1.86 P	0.68 E	20
Spring	0 E	0.85 G	0.14 P	0.58 E	-0.57 P	0.69 R	-0.61 P	21
Summer	0 E	0.58 P	0.42 P	0.72 E	0.19 G	1.76 P	0.29 R	21
Fall	0 E	0.91 E	0.09 P	0.42 E	0.07 E	1.47 P	0.80 E	21
All Seasons	0 E	0.81 G	0.10 P	0.36 E	-0.03 E	1.23 R	0.60 G	83

Table 3: Statistical comparison between *in situ* data and model outputs for ammonium profile in Santa Monica Bay.

491 outfalls, both model and observations show mid-depth peaks of ammonium concentration,  
 492 occasionally exceeding  $10 \text{ mmol m}^{-3}$ , which considerably overshadow values observed away  
 493 from outfalls. These high modeled ammonium concentrations are caused by wastewater  
 494 plumes.

495 The main source of uncertainty in data-model comparisons is the lack of spatial and  
 496 temporal coverage of measurements. Ammonium is typically measured near ocean out-  
 497 falls and is therefore biased towards high concentrations, but the dataset is highly variable.  
 498 Methodological difficulties exist with the measurement of ammonium in seawater, and as  
 499 such, we excluded non-detectable ammonium values in our analyses. Near the submarine  
 500 outfalls, ammonium concentrations are likely extremely heterogeneous due to buoyant plume  
 501 filaments, as observed in DiGiacomo et al. (2004) and in Warrick et al. (2007) in the Santa  
 502 Monica Bay, as well as in other regions (e.g. Florida, in Marmorino et al. (2010)). These  
 503 plume filaments are caused by horizontal advection of the discharged effluent. As a result,  
 504 the under sampling of ammonium may have led to poor statistical agreement between ob-  
 505 servations and model output. The model shows high to moderate agreement for the shape  
 506 of the profile and the mean concentration (Table 3). However, p-values for the correlations  
 507 were not always significant. Similarly, there were often biases and low performance regard-  
 508 ing variability statistics. This low model performance can be explained by the following two  
 509 reasons: (1) spatial sampling is likely missing plume filaments, for example observational  
 510 data points with high ammonium values that are capturing the plume are recorded next  
 511 very low or non-detect values; and (2) the resolution of the model (0.3 km), as well as model  
 512 averaging over the day, season, and depth range causes plume filaments to appear more  
 513 uniformly spread near the outfalls. Because plume filaments are lost in this averaging, the  
 514 model represents plumes as cloud-like distributions around outfalls; nevertheless, the aver-  
 515 age ammonium concentration of wastewater plumes is reasonably well represented. Detailed  
 516 information on the other sub-regions and their statistical comparison can be found in the  
 517 Supporting Information Tables S1 to S4.

### 518 *4.3.3 Horizontal gradients of ammonium*

519 Both *in situ* observations (dots in Fig. 9, Fig. 8a) and model output (background  
 520 colours in Fig. 9 and red line in Fig. 8a) show high concentrations of ammonium in the  
 521 subsurface layer below the thermocline (Fig. 9c), which we refer to as "high-ammonium  
 522 plume". This high-ammonium plume can extend from Huntington Beach to South Ventura,  
 523 encompassing three of the four major wastewater treatment plant outfalls in the SCB (See  
 524 Section 2.4). Both the model and observations show that the width and strength of the  
 525 high-ammonium plume are greatest in summer compared to other seasons. The Santa  
 526 Monica Bay Observatory (SMBO, Leinweber et al. (2009)) located 17 km north-west of the  
 527 submarine pipe Hyperion in Santa Monica Bay (Fig. 9g) frequently recorded concentrations  
 528 higher than  $2 \text{ mmol m}^{-3}$ , and up to  $4 \text{ mmol m}^{-3}$  at mid-depth (Fig. 9e), consistent with the  
 529 model (Fig. 9f). The depth of the maximum variability is at 40 m in the model, and slightly  
 530 shallower in the SMBO data, possibly because of a mismatch in the time period (1997-2000  
 531 for the model, and 2004-2010 for the SMBO). During winter, the model indicates vertical  
 532 mixing and dilution of the plume at the surface. Accordingly, ammonium concentrations  
 533 decrease slightly at depth (Fig. 9a) and increase at the surface, reaching values up to 2-6  
 534  $\text{mmol m}^{-3}$ , also consistent with observations around the outfall pipes (Fig. 8a).

### 535 *4.3.4 Spatial patterns in rates of nitrogen transformation*

536 Although we had no *in situ* nitrogen transformation rates with which to compare model  
 537 output during the simulation period, several datasets exist for the region that can serve  
 538 as a test for whether the model is simulating reasonable patterns in rates via the right  
 539 mechanisms. We found that modeled rates do agree with observed nitrogen transformation  
 540 rates. Nitrification rates, the sequential oxidation of  $\text{NH}_4^+$  to  $\text{NO}_3^-$  via  $\text{NO}_2^-$ , have been  
 541 observed to be higher within wastewater plumes in the SCB (McLaughlin et al., 2021), a

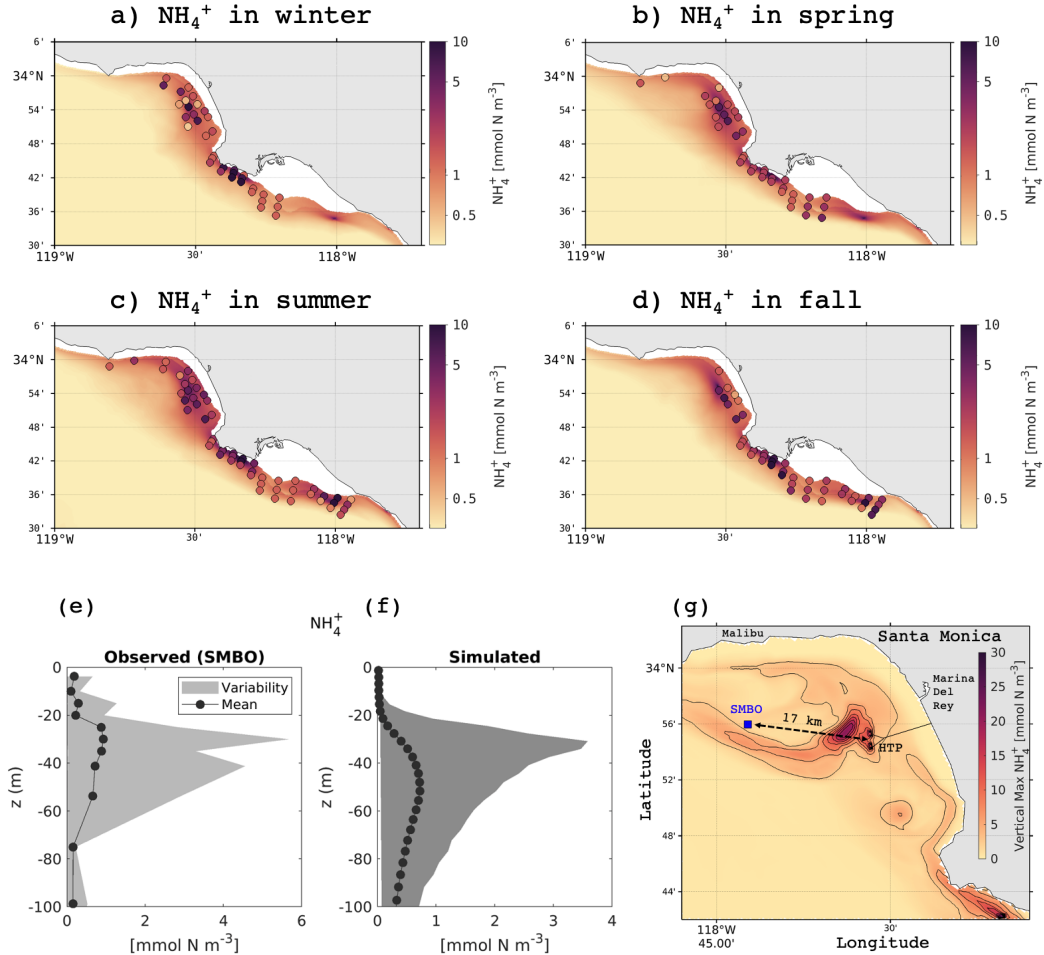


Figure 9: (a-d) Colors show seasonal average ammonium concentration between 30 and 45 m depth from the model, and dots from observations. High values highlight the movement and spatial distribution of the subsurface wastewater plumes along the Orange and Los Angeles counties. The highest concentrations are located within a narrow coastal band of about 10 - 15 km width, and are carried along the topography by the mean currents. (e-f) is a statistical comparison of the vertical profiles of ammonium at SMBO and the same location in the model. The anthropogenic ammonium plume signature is apparent 17 km away from Hyperion outfall. (g) shows the simulated vertical maximum concentration of  $\text{NH}_4^+$  averaged during a random day to illustrate the dispersal of the effluent toward SMBO originating from the 2 diffusers of Hyperion Treatment Plant (HTP).

542 pattern driven by high ammonium concentrations in the discharges (McLaughlin, Nezlin,  
 543 et al., 2017). In both observations and the model, nitrification predominately occurs below  
 544 the euphotic layer. Modeled vertically-integrated nitrification rates vary between 0.15 and  
 545 1.5 mmol N m<sup>-2</sup>d<sup>-1</sup>, consistent with observations within the SCB and in the California  
 546 Current (Table 5). The model also reproduces the spatial pattern of higher rates within  
 547 wastewater plumes (See Supporting Information Fig. S22). There is also good agreement  
 548 between observed and modeled rates of nitrate and ammonium uptake by phytoplankton  
 549 communities (McLaughlin et al., 2021) and (Kudela et al., 2017). Modeled nitrate uptake  
 550 rates vary between 2 and 11 mmol N m<sup>-2</sup>d<sup>-1</sup> and ammonium uptake rates vary between  
 551 6 and 51 mmol N m<sup>-2</sup>d<sup>-1</sup> in the Los Angeles and Orange County coasts, consistent with  
 552 observations in the SCB (Table 5).

#### 553 4.4 Chlorophyll concentrations

554 In general, the model was found to reproduce vertical and horizontal gradients in chloro-  
 555 phyll concentration in different subregions (Fig. 12). The timing of blooms was consistent  
 556 with changes in mixing and nutrient delivery in the SCB. We present three different subre-  
 557 gions characterized with distinct hydrodynamic regimes: the Santa Barbara Channel, and  
 558 the Los Angeles and San Diego coasts.

559 There are several sources of uncertainty in the chlorophyll, primary production, phyto-  
 560 plankton growth, and grazing rates observational records. For chlorophyll, bottle measure-  
 561 ments are accurate and precise, but measure a limited portion of the water column. Sensors  
 562 are accurate and precise in their measurement of fluorescence and have a rapid response  
 563 time, providing vertically resolved profiles; however, the algorithm to convert fluorescence  
 564 to chlorophyll concentration is inaccurate for the SCB. As a result, a correction factor has  
 565 been applied to Bight data which adds uncertainty to the observational dataset (Nezlin et  
 566 al., 2018). Satellite measurements of chlorophyll are inferred from ocean color (Kahru et  
 567 al., 2009). This method works well offshore, but breaks down nearshore where terrestrially-  
 568 derived colored dissolved organic matter creates uncertainty in reported satellite chlorophyll  
 569 estimates on the order of 100% or greater (Zheng & DiGiacomo, 2017). For primary pro-  
 570 duction, the incubation method to derive the rates is sensitive and precise (Cullen, 2001),  
 571 though measured rates are subject to bottle effects and there is some ambiguity as to whether  
 572 the experiments measure net primary production or gross primary production (Regaudie-de  
 573 Gioux et al., 2014). Phytoplankton growth and zooplankton grazing are also determined  
 574 experimentally, and duplicate measurements indicate that these methods are not very pre-  
 575 cise, with differences between duplicates ranging from 80% to 200% (Landry et al., 2009; Li  
 576 et al., 2011). For all three measurements, spatial and temporal under-sampling, particularly  
 577 during seasons with high variability, adds uncertainty to the data-model comparison.

##### 578 4.4.1 Horizontal gradients in chlorophyll

579 Despite the uncertainties outlined above, the model successfully simulates horizontal  
 580 gradients in chlorophyll in the three subregions (Santa Barbara, Los Angeles and San Diego).  
 581 The model captures the early, wide-spread spring bloom in the Santa Barbara Channel,  
 582 which occurs as a combination of a coastal bloom driven by spring upwelling, followed by a  
 583 bloom in the central and southwestern regions of the Channel (near the islands) in spring  
 584 and summer (Fig. 10). The latter is driven by the strengthening of the cyclonic circulation  
 585 in the Channel, which transports nutrients to the upper layers, and is regularly observed in  
 586 the region (Brzezinski & Washburn, 2011). The model captures the strong seasonality in  
 587 chlorophyll, wherein concentrations change from near zero in winter to up to 8 mg Chl m<sup>-3</sup>  
 588 in spring. Of the three regions, the blooms off Santa Barbara extends into late summer and  
 589 fall, where the average concentration is approximately 1-2 mg Chl m<sup>-3</sup>, a pattern replicated  
 590 in both model and observations .

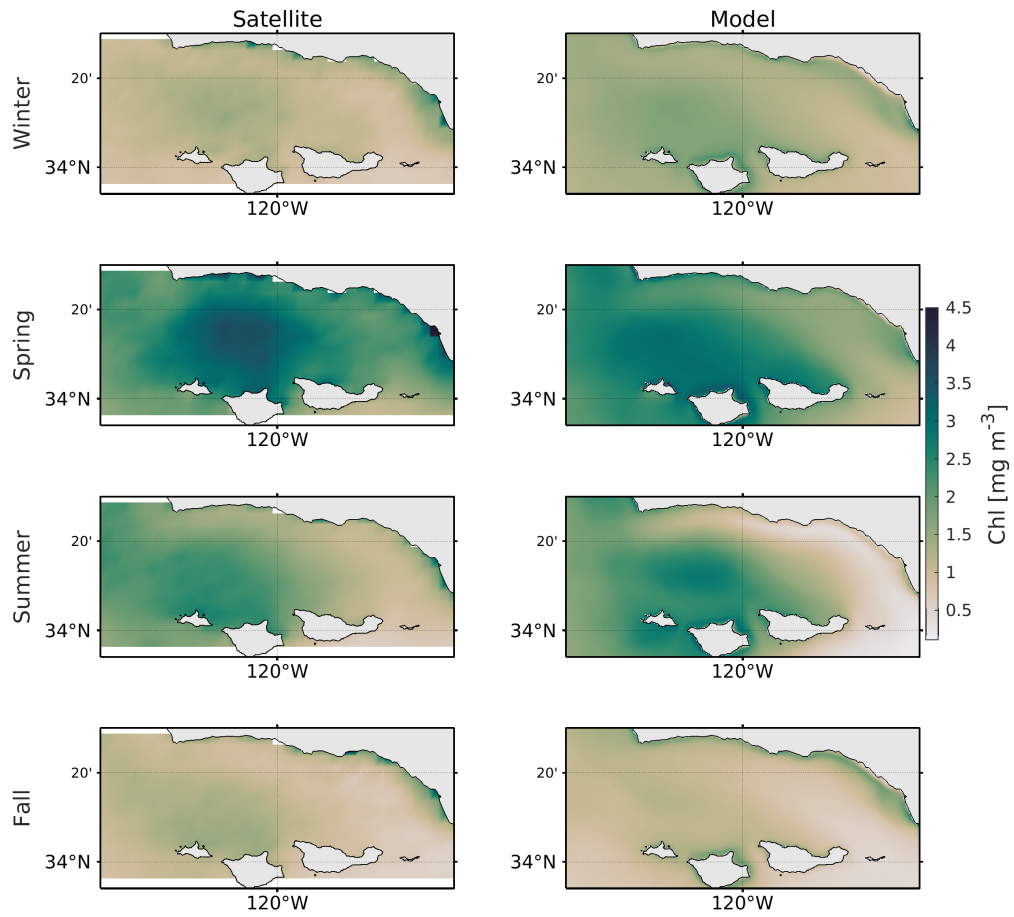


Figure 10: Comparison of seasonally-averaged surface chlorophyll between SeaWiFS remote sensing data (left panels) and the model (right panels) in the Santa Barbara Channel, where an important seasonal bloom is observed.

591 In the Los Angeles subregion, the model predicts broad patterns in chlorophyll concen-  
 592 trations, including a persistent bloom in the San Pedro Bay, consistent with observations  
 593 (Nezlin et al., 2012), and validated by comparison with remote sensing (Fig. 11). Both  
 594 satellite and modeled data show concentrations in the San Pedro Bay consistently higher  
 595 than 3 mg Chl m<sup>-3</sup> year-round, often extending into the Santa Monica Bay. The model  
 596 also reproduces the strong offshore gradients in chlorophyll, where across less than 15 km  
 597 offshore surface concentrations are reduced 3 to 4 fold (<1 mg Chl m<sup>-3</sup>) further decreasing  
 598 offshore. The model also reproduces the timing and magnitude of the blooms in the Santa  
 599 Monica and San Pedro Bays. The difference in timing of maximum chlorophyll concentra-  
 600 tions between the Santa Monica and San Pedro Bays likely reflects differences in nutrient  
 601 supply. Nutrients, in particular ammonium, are available near the surface during winter  
 602 (see Section 4.3.2), reflecting more vigorous mixing of the wastewater plume and land-based  
 603 nutrient supply by rivers (in particular in the San Pedro Bay) during winter storms (Lyon  
 604 & Stein, 2009). Storms and winter mixing events have been connected to phytoplankton  
 605 blooms in the region (Nezlin et al., 2012; Mantyla et al., 2008). Further offshore in the Los  
 606 Angeles region, the model recreates the weak seasonality of surface chlorophyll, with higher  
 607 concentrations during winter and spring, and lower concentrations in summer and fall. In  
 608 the offshore region of Santa Monica Bay, the seasonal cycle is marked by the increase of  
 609 surface phytoplankton between March and May as shown in Fig. 12b. Mean chlorophyll  
 610 values reach up to 3 to 4 mg Chl m<sup>-3</sup> in April and May, although concentrations below 2  
 611 mg Chl m<sup>-3</sup> are more common, consistent with observations over the same period.

612 Offshore of the San Diego coast subregion, the model recreates a slight increase in  
 613 surface chlorophyll in March; however, concentrations are generally below 1 mg Chl m<sup>-3</sup>  
 614 year-round (Fig 12(c)). The oligotrophic conditions of the southern Bight (Nezlin et al.,  
 615 2012; Mantyla et al., 2008) have been attributed to a deeper nitracline, which in turns  
 616 supports a deep chlorophyll maximum layer (Mantyla et al., 2008). This feature is well  
 617 represented in the model, which reproduces relatively high concentrations of chlorophyll in  
 618 subsurface layers (generally between 20 and 90 m depth) in the region).

619 **4.4.2 Vertical gradients and seasonal variability of chlorophyll**

Santa Monica: chlorophyll

	H	Correlation Coefficient	p-value	Cost Function	Percentage Bias	Ratio of Standard Deviations	Nash-Sutcliffe Model Efficiency	Number of observations
Winter	0 E	0.99 E	9E-06 E	0.48 E	0.09 E	0.91 E	0.94 E	714
Spring	0 E	0.93 E	9E-05 E	0.90 E	-0.42 P	0.52 P	-0.49 P	716
Summer	0 E	0.99 E	1E-08 E	0.58 E	-0.07 E	0.60 R	0.47 R	712
Fall	0 E	0.99 E	8E-08 E	0.48 E	0.16 G	0.75 R	0.76 E	718
All Seasons	0 E	0.99 E	4E-08 E	0.50 E	-0.01 E	0.73 R	0.80 E	2860

Table 4: Statistical comparison between *in situ* data and model outputs for chlorophyll profile in Santa Monica Bay.

620 The goodness-of-fit statistical metrics (correlation coefficient and cost function) for  
 621 chlorophyll are generally *excellent* or *good* for most seasons for all sub-regions (Table 4).  
 622 We were most concerned with performance for these metrics because the remaining statistics  
 623 may be affected by the aforementioned uncertainties due to the fluorometry calibration. The  
 624 observational measurements should be internally consistent (if not accurate), so the shapes  
 625 of profiles should be “correct” even if the magnitude is off due to poor calibration, and the  
 626 model was able to replicate these shapes accurately. Despite calibration issues, the model

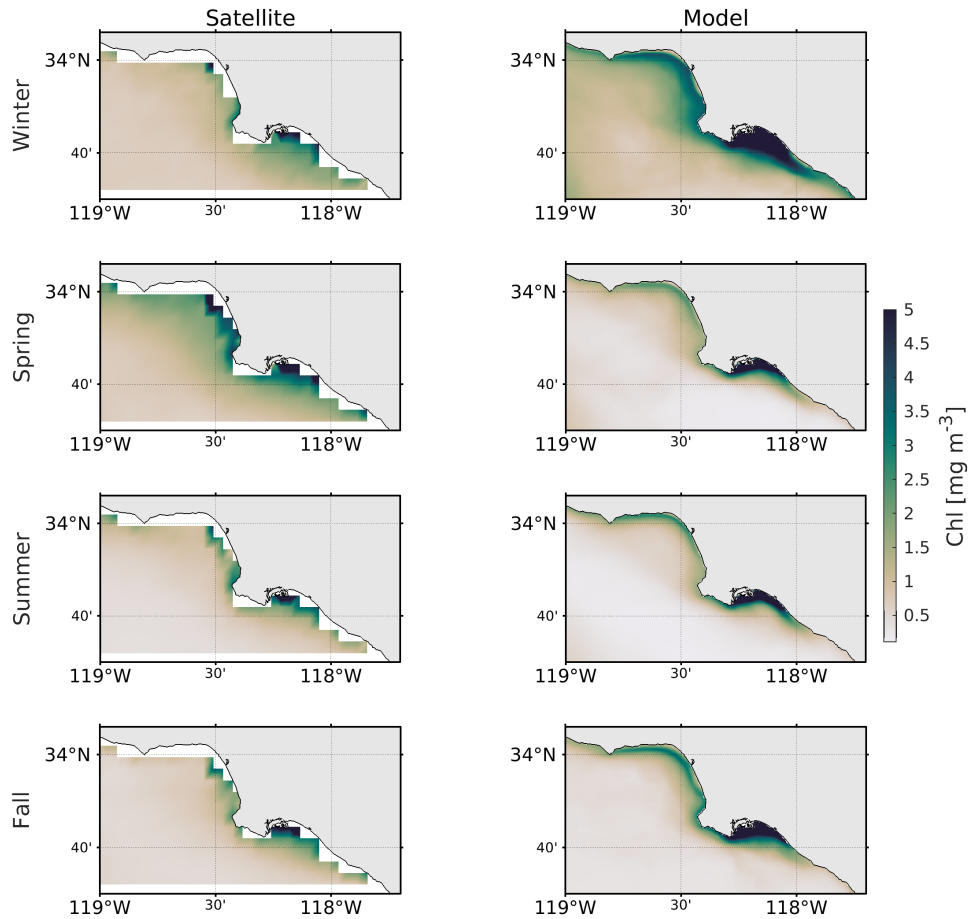


Figure 11: Comparison of seasonally-averaged surface chlorophyll between SeaWiFS remote sensing data (left panels) and the model (right panels) for years 1998-2000 in the Santa Monica and San Pedro Bays, where major POTW outfalls are found. The figure highlights the persistent coastal phytoplankton bloom, and the sharp inshore-offshore gradients.

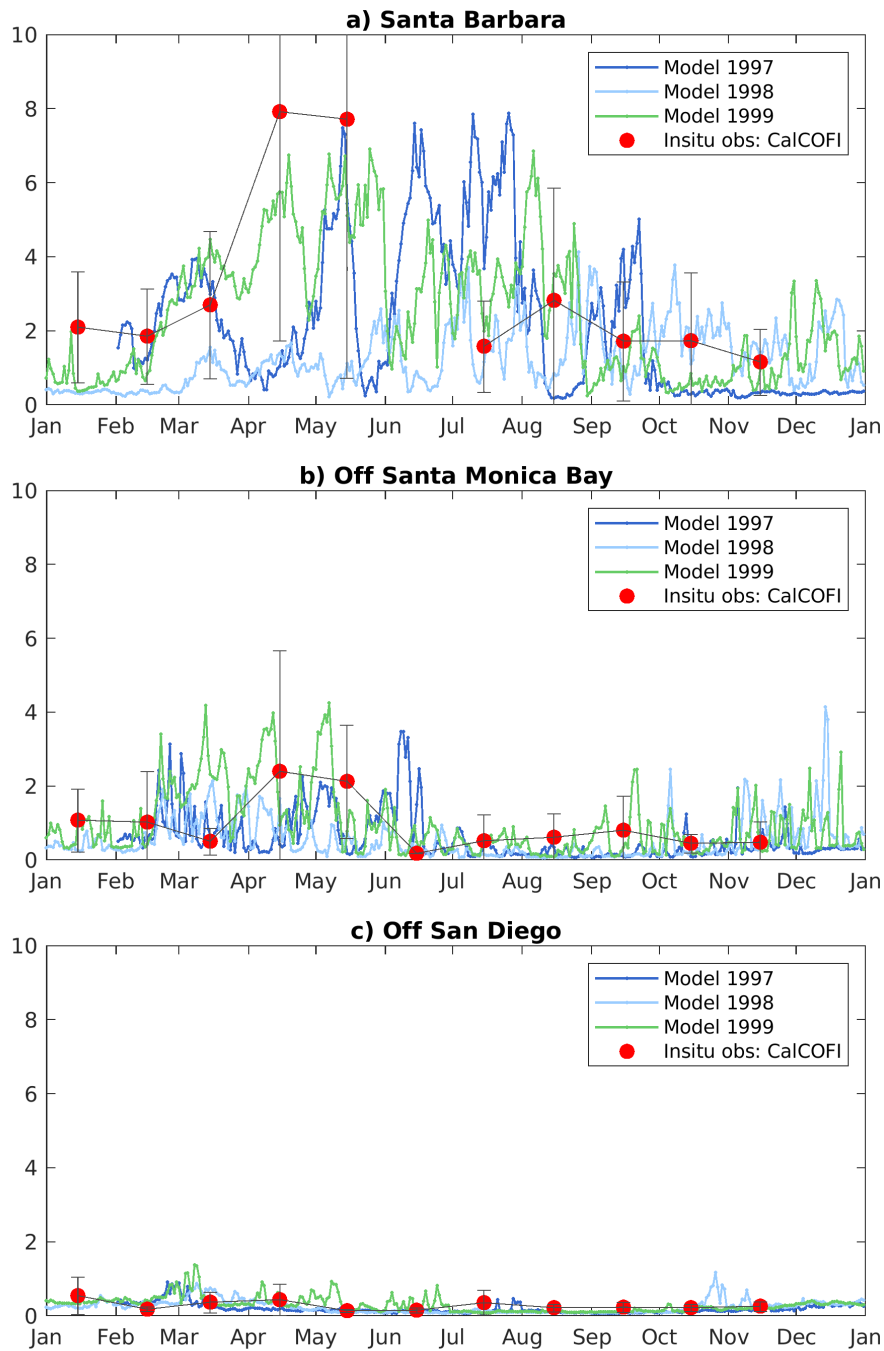


Figure 12: Comparison of surface chlorophyll concentration between different years of model output, and a climatology from CalCOFI *in situ* data. (a) is near the center of Santa Barbara Channel, (b) is offshore the Santa Monica Bay, and (c) is offshore San Diego. The model reproduces different productivity regimes across the Southern California Bight, with highly productive waters in the northern region, where average concentrations greater than  $3 \text{ mg m}^{-3}$  are observed for more than half of the year, and oligotrophic southern regions, where average surface concentrations rarely exceed  $1 \text{ mg m}^{-3}$ .

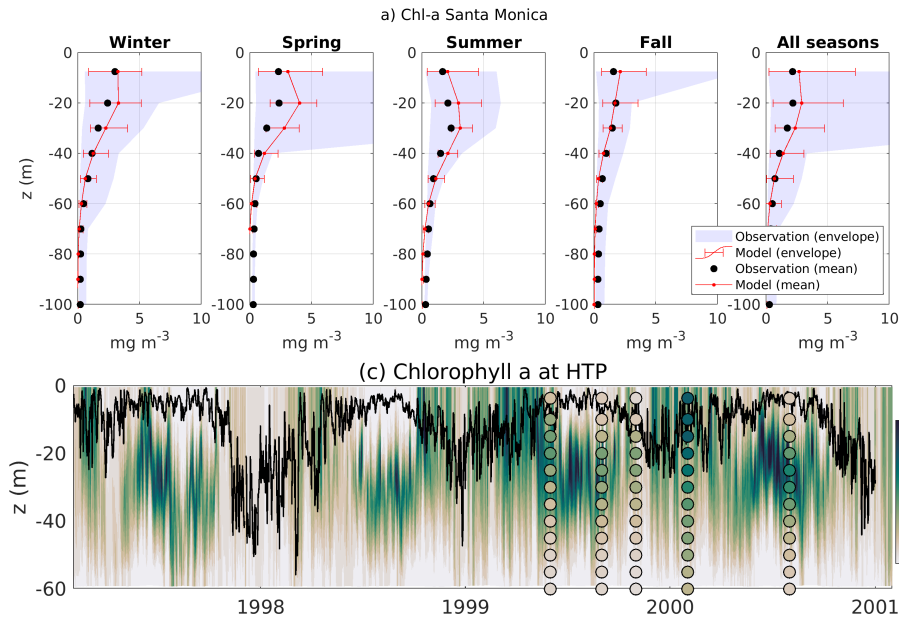


Figure 13: As for Fig. 5, but for chlorophyll concentration. Vertical profiles show a good agreement between simulated and *in situ* data, and display the formation of a subsurface chlorophyll maximum in summer, and a surface maximum in winter and spring. Concentrations in winter vary up to  $+5 \text{ mg Chl m}^{-3}$ . Note the very low concentrations during 1998 El Niño in the entire water column.

627 reproduced chlorophyll reasonably well for the northern Bight sub-regions of Santa Monica  
 628 Bay (Fig. 13) and Ventura/Oxnard (SI Fig. S11). Similar figures for other regions are shown  
 629 in the Supporting Information (Fig. S10-Fig. S13). All show that the model is reproducing  
 630 the magnitude and general shape of observed profiles. However, the model did not capture  
 631 the variability for most regions (except for Palos Verdes), generally scoring *reasonable* or  
 632 *poor* in the ratio of standard deviations for most seasons, particularly spring. This is likely  
 633 a result of the spatial and temporal averaging. Chlorophyll is highly variable in space  
 634 and time and under-sampling in either of these dimensions will adversely affect variability  
 635 estimates for a region and season. Therefore, reasonable performance for these metrics  
 636 was not unexpected. This suggests that the model may provide a conservative estimate  
 637 of phytoplankton biomass in the southern Bight, while reproducing accurate spatial and  
 638 temporal patterns in that biomass.

639 In addition to transporting nutrients from depth, upwelling 'seeds' surface waters with  
 640 subsurface water masses dominated by selected phytoplankton species, stimulating surface  
 641 blooms near the coast (Seegers et al., 2015). The model successfully reproduces this process,  
 642 wherein the subsurface chlorophyll maximum shoals and intensifies in spring, forced by the  
 643 vertical movement of the thermocline driven by upwelling. This seasonal dynamics occurs  
 644 across the domain in the model.

645 Offshore, in the more oligotrophic portion of the SCB, the model predicts that more  
 646 than 60% of the maximum concentration of phytoplankton biomass remains below the sur-  
 647 face all year, constantly fed by subsurface nutrients injections. This is consistent with  
 648 observations of a deep chlorophyll maximum throughout the region (Nezlin et al., 2018;  
 649 Mantyla et al., 2008; Seegers et al., 2015), and with observations at the San Pedro Oceanic  
 650 Time-Series (SPOT) located between the Palos Verdes Peninsula and Catalina Island (Fig.  
 651 3, lower panel). At SPOT, a region weakly influenced by anthropogenic nutrients inputs

652 at the surface, the model realistically simulates the seasonal cycle of chlorophyll. While  
 653 ammonium does not exceed typical "natural" values of  $\sim 1 \text{ mmol m}^{-3}$  below the surface,  
 654 chlorophyll concentrations regularly reach more than  $2 \text{ mg m}^{-3}$  between 20 and 40 m in  
 655 summer, in agreement with *in situ* measurement (Teel et al., 2018; Beman et al., 2011).  
 656 Figures to support the analysis are reported in the Supporting Information: Fig. S23).

657 However, in regions more heavily influenced by anthropogenic nutrients, such as the  
 658 Santa Monica Bay, the chlorophyll maximum progressively deepens from the surface in  
 659 winter to about 25 to 30 m depth in spring and summer, with chlorophyll concentrations  
 660 exceeding  $5 \text{ mg Chl m}^{-3}$  (Fig. 13(a)). This subsurface chlorophyll maximum is maintained  
 661 for four to five months (Fig. 13(b)) before the stratification is weakened by winter mixing.

#### 662 4.4.3 Primary production

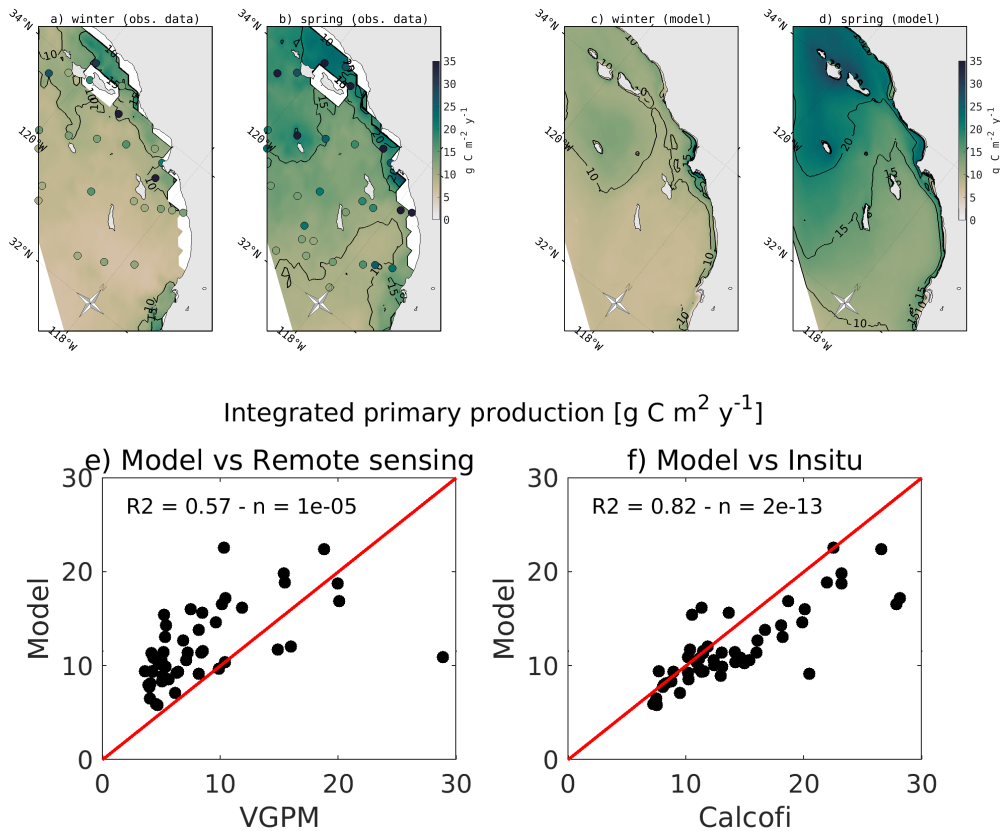


Figure 14: (a)-(b) Maps of vertically integrated Vertically Generalized Production Model (VGPM) net primary production and CalCOFI *in situ* measurements plotted as dots for (a) winter (January and February) and (b) spring (April to June). (c)-(d) Maps of vertically integrated primary production from the model, in (c) winter and (d) spring. Note the higher values for CalCOFI *in situ* measurements as compared to the satellite estimate, in better agreement with the model.

663 Validation on rates of primary production, phytoplankton growth and zooplankton grazing  
 664 (Table 5) provides an independent check on mechanisms responsible for chlorophyll as a  
 665 state variable. The spatial and temporal frequency of these data, garnered from CalCOFI  
 666 observations and literature values, is low. The most data as well as the most standardized  
 667 methodologies are available for primary production. However, many of the primary pro-

duction measurements used in this validation do not temporally coincide with the model period. Despite these uncertainties, the model generally reproduces expected large-scale patterns and seasonal variability in primary production.

This large scale variability was also mentioned in Deutsch et al. (2020). Model and data both show lower productivity in winter (Fig. 14a,c) and higher in spring (Fig. 14b,d), when the primary production is high along the coastal band, in the northern Bight around the Channel Islands (Fig. 14d), consistent with observations (Fig. 14b). This is consistent with the "green ribbon" of high-chlorophyll observed along the coast throughout the SCB (Lucas et al., 2011). The model reasonably reproduces the seasonal cycle of primary production in each of the subregions.

Phytoplankton are generally limited by a combination of nutrients and light, the latter of which is only limiting at depth in the SCB (Deutsch et al., 2020).

In winter, nitrogen is high at the surface in the northern SCB, and thus is not limiting. In the southern SCB, light and nitrogen are co-limiting due to stronger stratification, leading to oligotrophic conditions. In spring and through the summer, nitrogen is limiting nearly everywhere except in the Santa Barbara Channel and near the Channel Islands, where upwelling and submesoscale eddies maintain high nutrients at the surface.

The scatter plots in Fig. 14e-f show comparison of the simulated primary production between the *in situ* CalCOFI data and that derived from remote sensing (empirically adjusting the Behrenfeld-Falkowski Vertically Generalized Production Model [VGPM]). Model shows a correlation of about 0.6 with calCOFI, similarly to that reported by Kahru et al. (2009) when comparing the VGPM product with CalCOFI. The model shows a stronger correlation with VGPM data of the order of 0.8.

Finally, while slightly outside our model domain and simulation period, the modeled phytoplankton growth and zooplankton grazing rates were within the same order of magnitude as the measured rates from the California Current Long Term Ecological Research project (CC-LTER, see Landry et al. (2009)) (Table 5) in the northern portion of the Bight.

	Bight 13	Literature	Model
Primary production ( $\text{g C m}^{-2} \text{ y}^{-1}$ )	47.4, 1037.4		250, 1660
Nitrification ( $\text{mmol m}^{-3} \text{ d}^{-1}$ )	0, 0.225	0.02, 0.08	0.001, 0.27
$\text{NO}_3^-$ Uptake Rate ( $\text{mmol N mg Chl}^{-1} \text{ d}^{-1}$ )	0.005, 2.16		0.03, 0.15
$\text{NH}_4^+$ Uptake Rate ( $\text{mmol N mg Chl}^{-1} \text{ d}^{-1}$ )	0.10, 8.30		0.08, 0.15
Total Phytoplankton Growth $\mu$ ( $\text{d}^{-1}$ )		0.05, 0.8	0.3, 0.4
Grazing ( $\text{d}^{-1}$ )		0.02, 0.5	0.3, 1.5

Table 5: Comparison of biogeochemical rates between literature and model. Values are minimum and maximum. Literature values come from Landry et al. (2009); Li et al. (2011). Bight 13 is extracted from McLaughlin et al., (2021) study.

#### 4.5 Carbonate system and oxygen parameters

The model predicts changes in dissolved oxygen and carbon-system parameters related to photosynthesis and respiration processes, as well as horizontal transport and vertical mixing. As described in section 4.4.1, the coasts of Los Angeles and Santa Barbara are hot-spots of intensified plankton activity, and both systems are impacted by high variability and small-scale eddy circulation. In the upper layers, photosynthesis increases both dissolved oxygen and pH (Figs. 16 and 18), consistent with observations in these regions. The Santa

702 Monica Bay shows the highest oxygen production rates ( $60 \text{ mmol m}^{-2} \text{ d}^{-1}$ ), followed by the  
 703 Santa Barbara coast ( $57 \text{ mmol m}^{-2} \text{ d}^{-1}$ ), while rates in the Orange County and San Diego  
 704 coasts are nearly two times lower. Oxygen and carbon are further replenished at the surface  
 705 by air-sea gas exchange with the atmosphere. Export of newly-fixed organic carbon leads in  
 706 both regions to high remineralization rates that consume oxygen and release carbon dioxide  
 707 at depth. We simulate similar high organic matter export (around  $30 \text{ mmol m}^{-2} \text{ d}^{-1}$ ) in  
 708 both the Santa Barbara and Los Angeles coasts (see Supporting Information: Fig. S24).

709 The reliability of these predictions can be tested through validation of dissolved oxygen  
 710 and carbonate system parameters. There are several sources of uncertainty in the dissolved  
 711 oxygen, pH, and aragonite saturation state observational records which affect data-model  
 712 comparisons. For dissolved oxygen, sensors are relatively accurate and precise and have a  
 713 rapid response time ( $< 1\text{s}$ ) creating vertically resolved profiles. Repeated field measurement  
 714 accuracy for CTD dissolved oxygen sensors was reported to be approximately  $8 \text{ mmol m}^{-3}$   
 715 (Coppola et al., 2013). The pH observational record is particularly fraught with uncertainty.  
 716 An evaluation of pH sensor data in the SCB indicated that, while sensor pH measurements  
 717 were well correlated with discrete bottle samples collected at the same depth, there was a  
 718 clear bias in pH, with sensor measurements under-predicting bottle measurements and high  
 719 variability in the differences between paired bottle and sensor measurements ( $\Delta\text{pH}$  ranging  
 720 from  $\pm 0.5$ ) (McLaughlin, Dickson, et al., 2017). The aragonite saturation state is esti-  
 721 mated using an algorithm developed for the region (Juraneck et al., 2011) for both *in situ*  
 722 observations and model output, because complete measurements of carbon-system param-  
 723 eters required to calculate  $\Omega_{Ar}$  are missing. For all three variables, spatial and temporal  
 724 under-sampling, particularly during seasons with high variability, adds uncertainty to the  
 725 data-model comparison.

#### 726 4.5.1 Vertical gradients and seasonal variability of dissolved oxygen

727 The model reproduces observed seasonal and spatial patterns in dissolved oxygen con-  
 728 centration (Fig. 15), accurately simulating magnitude, vertical and horizontal gradients,  
 729 and variability. Quantitative statistical analysis (see Table 6) indicated that the model per-  
 730 formance was ‘*excellent*’ or ‘*good*’ for nearly all metrics for all regions and seasons. The  
 731 lowest performance of the model was characterized as ‘*poor*’ for two sub-regions for the  
 732 Nash-Sutcliff Model Efficiency during Spring, and ‘*reasonable*’ for some metrics in some  
 733 sub-regions, which may be related to under sampling during seasons with high variability,  
 734 as described above. Similar to temperature, we tested whether the variability in spring may  
 735 be impacting the performance statistics by extracting random profiles for the region (not  
 736 shown, expressed with large error-bars in the spring season plots in Fig. 16), which show how  
 737 dissolved oxygen on a random single day can more closely align with the observations. This  
 738 supports the hypothesis that observational uncertainty is behind the lack of observational  
 739 agreement with the model. Model performance was lowest in the Orange County and San  
 740 Diego subregions, where model predictions tended to overestimate dissolved oxygen, consis-  
 741 tent with the chlorophyll underprediction, a likely consequence of the lack of cross-border  
 742 inputs from Mexican waters.

743 The model also reproduces the seasonality in dissolved oxygen in all subregions (Fig.  
 744 16), characterized by large meridional and vertical variability. Near the Channel Islands,  
 745 dissolved oxygen varies at 50 m by up to  $140 \text{ mmol O}_2 \text{ m}^{-3}$  between the highest winter  
 746 values and the lowest summer values, reflecting the dynamics of upwelling, productivity,  
 747 and gas-exchange with the atmosphere. Offshore the Santa Monica and San Diego coasts,  
 748 the variability between winter and summer is of the order of  $80\text{-}90 \text{ mmol O}_2 \text{ m}^{-3}$ . Surface  
 749 concentrations are everywhere above  $240 \text{ mmol O}_2 \text{ m}^{-3}$  year-round, consistent with observa-  
 750 tions. The highest summer concentrations are observed at the depth of the deep chlorophyll  
 751 maximum, reflecting photosynthesis, while decreasing at depth to below  $150 \text{ mmol O}_2 \text{ m}^{-3}$ .  
 752 These patterns are generally consistent with observations in the same regions.

753 During the 1998 El Niño event, the model shows a net decrease of dissolved oxygen  
 754 near the surface, and a net increase below it. During this period, the entire upper layer  
 755 (0-80 m) is characterized by a homogeneous concentration of about 240 mmol O<sub>2</sub> m<sup>-3</sup> over  
 756 almost the entire SCB (not shown). Only the San Pedro and Santa Monica Bays show  
 757 higher concentrations, which we attribute to the local anthropogenic nutrient enrichment  
 758 and subsequent blooms (see Fig. 19). This is consistent with observations of the 1998 event  
 759 in California coastal waters (Chavez et al., 2002; Booth et al., 2014).

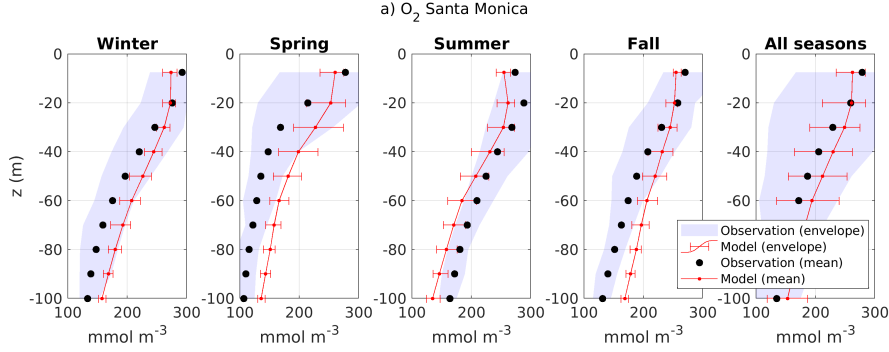


Figure 15: As for Fig. 5, but for oxygen concentration.

Santa Monica								
	H	Correlation Coefficient	p-value	Cost Function	Oxygen Percentage Bias	Ratio of Standard Deviations	Nash-Sutcliffe Model Efficiency	Number of observations
Winter	0 E	0.97 E	9E-07 E	0.14 E	-0.09 E	1.20 G	0.77 E	716
Spring	0 E	0.91 E	3E-04 E	0.26 E	-0.23 R	1.03 E	0.37 R	702
Summer	0 E	0.99 E	2E-10 E	0.07 E	0.07 E	0.99 E	0.86 E	712
Fall	0 E	0.97 E	2E-06 E	0.19 E	-0.14 G	1.49 P	0.42 R	718
All Seasons	0 E	0.97 E	3E-06 E	0.14 E	-0.11 G	1.18 G	0.69 E	2848
pH								
	H	Correlation Coefficient	p-value	Cost Function	Percentage Bias	Ratio of Standard Deviations	Nash-Sutcliffe Model Efficiency	Number of observations
Winter	0 E	0.99 E	2E-08 E	0.01 E	0.01 E	0.59 P	0.57 G	632
Spring	0 E	0.97 E	2E-06 E	0.02 E	-0.02 E	1.45 P	0.15 P	702
Summer	0 E	0.96 E	9E-06 E	0.01 E	0.01 E	1.01 E	0.85 E	712
Fall	0 E	0.97 E	3E-06 E	0.01 E	0.01 E	1.49 P	0.78 E	715
All Seasons	0 E	0.97 E	5E-06 E	0.01 E	-0.01 E	1.12 G	0.84 E	2761

Table 6: Statistical comparison between *in situ* data and model outputs for dissolved oxygen and pH profile in Santa Monica Bay.

760 **4.5.2 Vertical gradients and seasonal variability of carbon-system parameters**  
 761

762 Together with pH, the saturation state of aragonite ( $\Omega_{Ar}$ ) is often used as a metric  
 763 to identify the potential impact of Ocean Acidification on marine calcifiers, because it is a

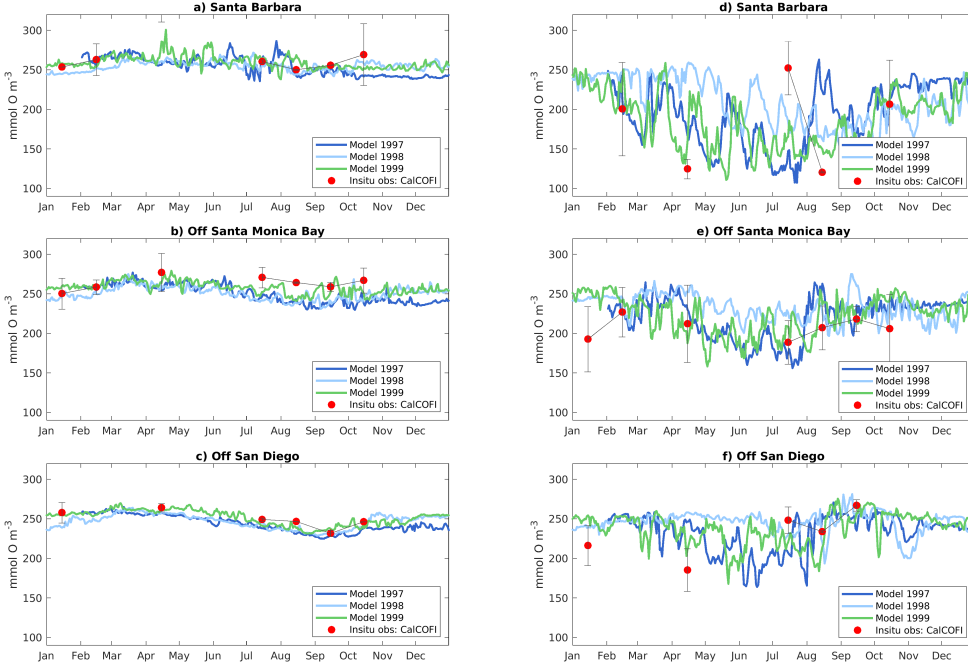


Figure 16: Comparison of dissolved oxygen concentration between different years of model output, and a climatology from CalCOFI *in situ* data. SB is near the center of Santa Barbara Channel, SM is offshore the Santa Monica Bay, and SD is offshore San Diego. Left panels show surface concentrations, right panels concentrations at 50 m depth.

764 measure of the availability of carbonate ions for calcium carbonate precipitation (Bednarsek  
 765 et al., 2019).  $\Omega_{Ar}$  shows similar vertical variability as dissolved oxygen (Juraneck et al.,  
 766 2009; Alin et al., 2012). Similar to deoxygenation, reduction in pH and  $\Omega_{Ar}$  in the upper  
 767 layers is generally caused by coastal upwelling or by local physical processes (Feely et al.,  
 768 2018). We utilize sensor pH data sets to evaluate vertical profiles in the carbonate system.  
 769 Because of the known uncertainty in pH measurements, we are most concerned with how  
 770 well the model reproduced the shape of the profiles (i.e., goodness of fit estimates, as with  
 771 chlorophyll). Sensor-derived pH profile measurements should be internally consistent within  
 772 a data set (if the sensor is working properly and if pressure issues are minimal), providing  
 773 some value to goodness of fit assessments. Given these constraints, the data-model compar-  
 774 isons for pH sensor data were generally ‘*excellent*’ or ‘*good*’ for all sub-regions and all  
 775 seasons. Unsurprisingly, the model performance reproducing observational means and vari-  
 776 ability was generally ‘*reasonable*’ or ‘*poor*’ for most sub-regions and seasons, with some,  
 777 if not most, of this disagreement due to difficulties in conducting a validation of the model  
 778 with large uncertainties in sensor-derived pH profiles. Recently, the CalCOFI program has  
 779 incorporated  $\Omega_{Ar}$  into its sampling program. Although the data do not line up with the  
 780 model period, they are useful for evaluating seasonal variability in the model. Generally,  
 781 the model reproduces seasonal and vertical variability in  $\Omega_{Ar}$ , with higher saturation states  
 782 in the summer and fall, when waters are generally more stratified, and lower values in win-  
 783 ter and spring, when upwelling brings undersaturated waters closer to the surface.  $\Omega_{Ar}$  is  
 784 also much lower and more highly variable at depth. These patterns are consistent with  
 785 observations throughout the SCB (McLaughlin et al., 2018).

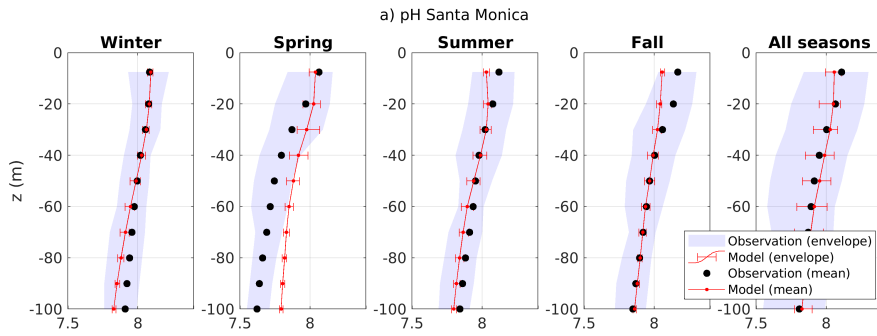


Figure 17: As for Fig. 5 but for dissolved pH.

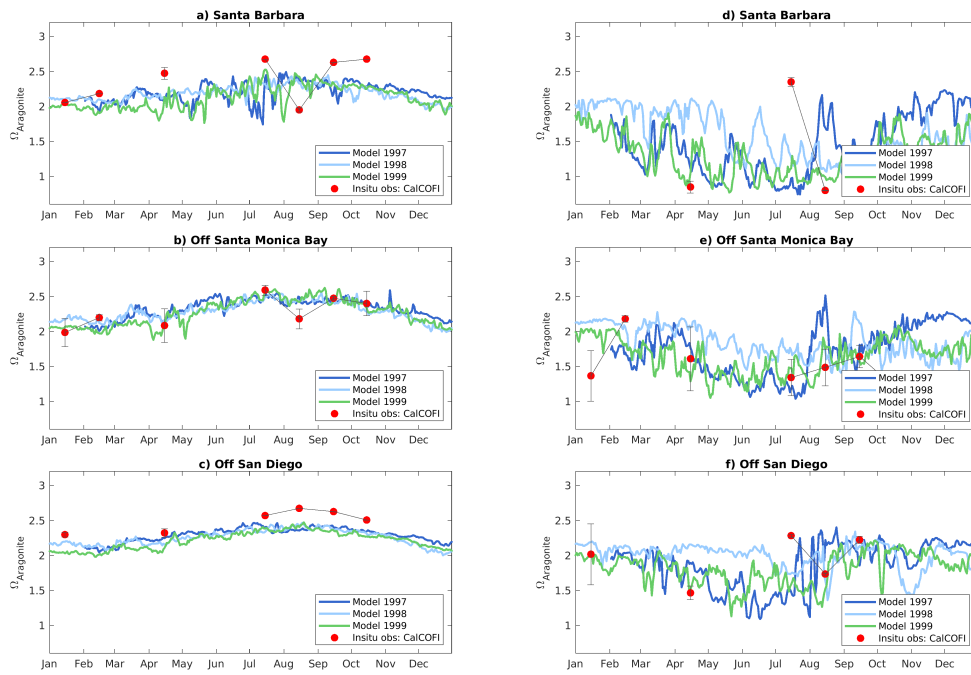


Figure 18: Comparison of the saturation state of aragonite between different years of model output, and a climatology from CalCOFI *in situ* data. SB is near the center of Santa Barbara Channel, SM is offshore the Santa Monica Bay, and SD is offshore San Diego. Left panels show surface values, right panels values at 50 m depth.

## 5 Summary

In this study, we demonstrated the readiness of high-resolution, dynamically down-scaled, physical-biogeochemical model to mechanistically investigate links between a comprehensive reconstruction of terrestrial and atmospheric nutrient inputs, coastal eutrophication, and biogeochemical change in the SCB coastal waters. This modeling platform is an important achievement because it strikes a balance of capturing the forcing of coast-wide basin mesoscale phenomena, while capturing the combined effects of bathymetry and sub-mesoscale eddies that intensify transport of nutrients and biological material. Moreover, this model allows to run hindcast simulation of primary production, ocean acidification and de-oxygenation at timescales that can approach the multi-annual frequencies of intrinsic ocean variability, making the grand challenge of disentangling natural variability, climate change, and local anthropogenic forcing a tractable task in the near-term.

ROMS has a long history of validation and management acceptance through various applications in the CCS (e.g. Marchesiello et al. (2003); Capet et al. (2004); Capet, Colas, et al. (2008); Capet, Campos, and Paiva (2008); Capet, McWilliams, et al. (2008); Shchepetkin and McWilliams (2011); Renault, Molemaker, Gula, et al. (2016)). In contrast, experience with BEC within the SCB is more limited. Our validation study of coastal eutrophication gradients in the SCB nearshore complements the U.S. West Coast-wide study of (Deutsch et al., 2020) and strengthens confidence that the basic CCS BEC model formulation, forcing and parameterization is appropriate not only for coastwide analyses but also for detailed local studies of coastal eutrophication in the highly urbanized SCB. The representation of physical processes such as vertical mixing and horizontal circulation was consistent across the model and measurements. The model reproduces the main structure of the climatological upwelling front and cross-shore isopycnal slopes, the mean current patterns and associated temperature gradients. We also demonstrate good agreement between model simulations and the mean distributions and variability of key ecosystem metrics, including surface nutrients and productivity, and subsurface  $O_2$  and carbonate saturation. The spatial patterns of PP, phytoplankton growth rates, and zooplankton grazing are broadly consistent with measured rates. The distribution of primary production is governed by the trade-off between nutrient and light limitation, a balance that reproduces and explains the observed spatial variations in the depth of the deep chlorophyll maximum. Statistical measures of model agreement on biogeochemical state variables was excellent to good and the range of predicted biogeochemical rates on par with observations. Under the realistic flow fields produced by ROMS, the conformity of model predictions with a rich observational dataset is a strong demonstration of model validity for coastal eutrophication applications. We also demonstrated that the model responds with confidence to the variability caused by El Niño modifying the vertical distribution of the physical and biogeochemical properties across the upper ocean of the entire Bight as shown in the three-dimensional representation in Fig.19.

Whereas the points cited above show that the model is effective and encouraging. Other points remain even less clear in the model. For example, the structure of the food web is simplified, the model is unable to detect bloom events called red tides, which occur over short periods on limited coastal scales in the spring. Despite the good performance of the model in reproducing the total primary production and the scales of variability of the grazing rate, the model does not have the functionality to demonstrate the decoupling between different groups of zooplankton, thus biasing our knowledge of the cycle of the upper scales. From a mechanical point of view, at scales of 300m resolution, the model does not resolve dynamics occurring at sales of tens of meters (Dauhajre et al., 2019), or the vertical displacement of the nutrients in the surf zone. And finally, simplification of the biological processes can generate model biases at the hourly to daily scale to simulate the variability of vertical gradients in oxygen and pH at the limit between the upper layer dominated by the air-ocean exchange and photosynthesis production and the deeper layer dominated by plankton and bacterial consumption.

Quantitative and qualitative results of confidence assessments are essential for informing management decisions, evaluating management strategies, and providing a basis for risk analyses. The most successful management approaches are those that explicitly incorporate uncertainty (e.g. Taylor et al. (2000)). An assessment of model validation must consider the complex combination of model and observational uncertainties (Allen et al., 2007), including: 1) uncertainty/error in the model, including intrinsic variability; 2) uncertainty/error in measured data; 3) uncertainty from the difference in spatial scales of the model output relative to the measured data used in the comparison (specifically, comparing a 0.3 km grid cell to a discrete sampling station); and 4) uncertainty from the difference in temporal averaging of the model output relative to the measured data. For parameters in which we have high confidence in the observational record, temperature and dissolved oxygen, model performance statistics show excellent agreement for mean profiles, vertical and horizontal gradients, as well as seasonal variability. The model reproduces chlorophyll reasonably well, albeit with some bias, which can be partly attributed to model simplification of the plankton diversity and partly to measurement uncertainty and sparseness of the sampling data in respect to ship-based data or cloud cover and algorithm biases in respect to satellite derived data. pH and ammonium have lower agreement, likely due to important measurement uncertainty and sampling bias, but general spatial and temporal patterns are correctly reproduced in the model.

Greater clarity is needed in the requirements for model performance and uncertainty to support decisions on management of SCB coastal water quality and eutrophication (Boesch, 2019). These requirements are likely to be driven largely by the approach that will be used to interpret a "significant impact" (e.g. existing water quality pH and DO criteria, or biologically relevant thresholds; (Weisberg et al., 2016)), as these have significant implications for required model precision and accuracy on different spatial and temporal scales. Future efforts to constrain uncertainty could include sensitivity analyses and model ensemble comparisons of BEC with other biogeochemical models that feature increasingly complex representations of planktonic functional groups and including the representation of the benthic communities, and the effects of the sediment-pelagic interactions. Finally, long-term investments are needed in coupled chemical-biological observations of phytoplankton and zooplankton community structure. These observations are critical to provide understanding of evolution of lower trophic ecosystem structure with climate change, and their relationship with biogeochemical cycles linked to ocean acidification and oxygen loss (Sailley et al., 2013). Ultimately, the need to constrain uncertainty will likely scale with the economic import of management decisions under consideration, which could range from increased monitoring requirements to multi-billion dollar non-point source controls and wastewater treatment plant upgrades.

## Acknowledgments

This research was supported by NOAA grants NA15NOS4780186 and NA18NOS4780174, California Ocean Protection Council grant C0100400, and NSF grants OCE-1419323 and OCE-1419450. Computational resources were provided by the Extreme Science and Engineering Discovery Environment (XSEDE) through allocation TG-OCE170017, and by the super-computer Hoffman2 at the University of California Los Angeles, at the Institute for Digital Research and Education (IDRE, UCLA). Code is available in (Kessouri, McWilliams, et al., 2020). In situ observation data to generate the figures and statistics are available in (Kessouri, McLaughlin, et al., 2020). Local land-based and atmospheric data can be found in (Sutula et al., 2021a).

## References

Aita, M. N., Yamanaka, Y., & Kishi, M. J. (2007). Interdecadal variation of the lower trophic ecosystem in the northern Pacific between 1948 and 2002, in a 3-d implementation of the nemuro model. *ecological modelling*, 202(1-2), 81–94.

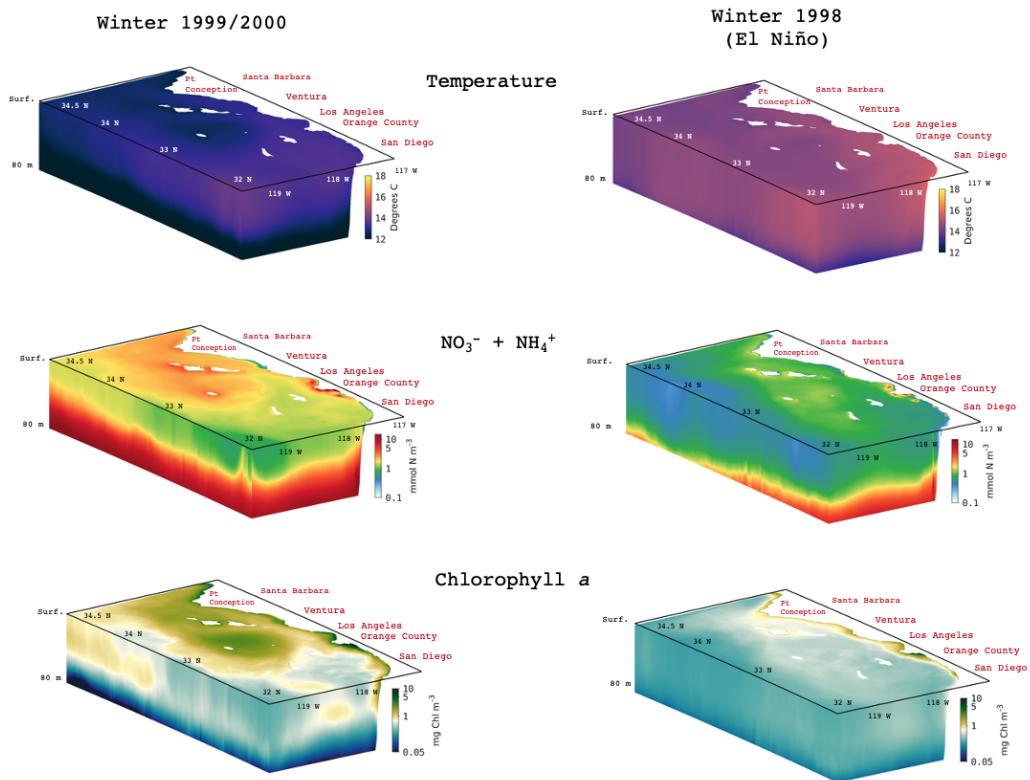


Figure 19: Three-dimensional illustration of temperature, DIN ( $\text{NO}_3^- + \text{NH}_4^+$ ) and chlorophyll in the Southern California Bight. Panels show winter 1999 and 2000 (left panels), winter 1998 during El Niño period (right panels).

- 889 Alin, S. R., Feely, R. A., Dickson, A. G., Hernández-Ayón, J. M., Juranek, L. W., Ohman,  
890 M. D., & Goericke, R. (2012). Robust empirical relationships for estimating the  
891 carbonate system in the southern california current system and application to calcofi  
892 hydrographic cruise data (2005–2011). *Journal of Geophysical Research: Oceans*,  
893 *117*(C5).
- 894 Allen, J., Somerfield, P., & Gilbert, F. (2007). Quantifying uncertainty in high-resolution  
895 coupled hydrodynamic-ecosystem models. *Journal of Marine Systems*, *64*(1-4), 3–14.
- 896 Arhonditsis, G., Tsirtsis, G., Angelidis, M., & Karydis, M. (2000). Quantification of the  
897 effects of nonpoint nutrient sources to coastal marine eutrophication: applications to a  
898 semi-enclosed gulf in the mediterranean sea. *Ecological Modelling*, *129*(2-3), 209–227.
- 899 Armstrong, R. A., Lee, C., Hedges, J. I., Honjo, S., & Wakeham, S. G. (2001). A new,  
900 mechanistic model for organic carbon fluxes in the ocean based on the quantitative  
901 association of poc with ballast minerals. *Deep Sea Research Part II: Topical Studies  
902 in Oceanography*, *49*(1-3), 219–236.
- 903 Aumont, O., & Bopp, L. (2006). Globalizing results from ocean in situ iron fertilization  
904 studies. *Global Biogeochemical Cycles*, *20*(2).
- 905 Bednarsek, N., Feely, R. A., Howes, E. L., Hunt, B., Kessouri, F., León, P., ... others  
906 (2019). Systematic review and meta-analysis towards synthesis of thresholds of ocean  
907 acidification impacts on calcifying pteropods and interactions with warming. *Frontiers  
908 in Marine Science*, *6*, 227.
- 909 Behrenfeld, M. J., & Falkowski, P. G. (1997). Photosynthetic rates derived from  
910 satellite-based chlorophyll concentration. *Limnology and Oceanography*, *42*(1), 1-20.  
911 Retrieved from [https://aslopubs.onlinelibrary.wiley.com/doi/abs/10.4319/  
912 lo.1997.42.1.0001](https://aslopubs.onlinelibrary.wiley.com/doi/abs/10.4319/lo.1997.42.1.0001) doi: <https://doi.org/10.4319/lo.1997.42.1.0001>
- 913 Beman, J. M., Steele, J. A., & Fuhrman, J. A. (2011). Co-occurrence patterns for abundant  
914 marine archaeal and bacterial lineages in the deep chlorophyll maximum of coastal  
915 california. *The ISME journal*, *5*(7), 1077–1085.
- 916 Boesch, D. F. (2019). Barriers and bridges in abating coastal eutrophication. *Frontiers in  
917 Marine Science*, *6*, 123.
- 918 Boesch, D. F., Brinsfield, R. B., & Magnien, R. E. (2001). Chesapeake bay eutrophication:  
919 Scientific understanding, ecosystem restoration, and challenges for agriculture. *Journal  
920 of Environmental Quality*, *30*(2), 303–320.
- 921 Bograd, S. J., Buil, M. P., Di Lorenzo, E., Castro, C. G., Schroeder, I. D., Goericke, R.,  
922 ... Whitney, F. A. (2015). Changes in source waters to the southern california bight.  
923 *Deep Sea Research Part II: Topical Studies in Oceanography*, *112*, 42–52.
- 924 Booth, J., Woodson, C., Sutula, M., Micheli, F., Weisberg, S., Bograd, S., ... Crowder, L.  
925 (2014). Patterns and potential drivers of declining oxygen content along the southern  
926 california coast. *Limnology and Oceanography*, *59*(4), 1127–1138.
- 927 Brzezinski, M. A., & Washburn, L. (2011). Phytoplankton primary productivity in the santa  
928 barbara channel: Effects of wind-driven upwelling and mesoscale eddies. *Journal of  
929 Geophysical Research: Oceans*, *116*(C12).
- 930 Buitenhuis, E. T., Li, W. K., Vaultot, D., Lomas, M. W., Landry, M., Partensky, F., ...  
931 others (2012). Picophytoplankton biomass distribution in the global ocean. *Earth  
932 System Science Data*, *4*(1), 37–46.
- 933 Byun, D. W., Song, C.-K., Percell, P., Pleim, J., Otte, T., Young, J., & Mathur, R. (2006).  
934 Linkage between wrf/nmm and cmaq models. In *Presentation at 5th annual cmas  
935 conference, chapel hill, nc, available at: www.cmascenter.org* (pp. 16–18).
- 936 Capet, X., Campos, E., & Paiva, A. (2008). Submesoscale activity over the Argentinian  
937 shelf. *Geophysical Research Letters*, *35*(15).
- 938 Capet, X., Colas, F., McWilliams, J. C., Penven, P., & Marchesiello, P. (2008). Eddies  
939 in eastern boundary subtropical upwelling systems. *Ocean Modeling in an Eddying  
940 Regime, Geophys. Monogr. Ser.*, *177*, 131–147.
- 941 Capet, X., Klein, P., Hua, B. L., Lapeyre, G., & McWilliams, J. C. (2008). Surface kinetic  
942 energy transfer in surface quasi-geostrophic flows. *Journal of Fluid Mechanics*, *604*,  
943 165–174.

- 944 Capet, X., Marchesiello, P., & McWilliams, J. (2004). Upwelling response to coastal wind  
945 profiles. *Geophysical Research Letters*, *31*(13).
- 946 Capet, X., McWilliams, J. C., Molemaker, M. J., & Shchepetkin, A. (2008). Mesoscale  
947 to submesoscale transition in the California Current System. Part I: Flow structure,  
948 eddy flux, and observational tests. *Journal of Physical Oceanography*, *38*(1), 29–43.
- 949 Cederwall, H., & Elmgren, R. (1990). Biological effects of eutrophication in the baltic sea,  
950 particularly the coastal zone. *Ambio. Stockholm*, *19*(3), 109–112.
- 951 Cerco, C. F., & Cole, T. (1993). Three-dimensional eutrophication model of chesapeake  
952 bay. *Journal of Environmental Engineering*, *119*(6), 1006–1025.
- 953 Chavez, F., Pennington, J., Castro, C., Ryan, J., Michisaki, R., Schlining, B., ... Collins,  
954 C. (2002). Biological and chemical consequences of the 1997–1998 el niño in central  
955 california waters. *Progress in Oceanography*, *54*(1-4), 205–232.
- 956 Coppola, L., Salvetat, F., Delauney, L., BSH, D. M., Karstensen, J., & Thierry, V. (2013).  
957 White paper on dissolved oxygen measurements: scientific needs and sensors accuracy.  
958 *Jerico Project*.
- 959 Cullen, J. (2001). *Primary production methods*. London, UK: Academic Press.
- 960 Dauhajre, D. P., McWilliams, J. C., & Renault, L. (2019). Nearshore lagrangian con-  
961 nectivity: Submesoscale influence and resolution sensitivity. *Journal of Geophysical*  
962 *Research: Oceans*, *124*(7), 5180–5204.
- 963 Derrick, B., Toher, D., & White, P. (2016). Why Welch’s test is Type I error robust.  
964 *QUANTITATIVE METHODS FOR PSYCHOLOGY*, *12*(1), 30-38. doi: {10.20982/  
965 tqmp.12.1.p030}
- 966 Deutsch, C. A., Frenzel, H., McWilliams, J. C., Renault, L., Kessouri, F., Howard, E. M., ...  
967 Yang, S. (2020). Biogeochemical variability in the california current system. *bioRxiv*.
- 968 DiGiacomo, P. M., Washburn, L., Holt, B., & Jones, B. H. (2004). Coastal pollution  
969 hazards in southern california observed by sar imagery: stormwater plumes, wastew-  
970 ater plumes, and natural hydrocarbon seeps. *Marine Pollution Bulletin*, *49*(11-12),  
971 1013–1024.
- 972 Dong, C., Idica, E. Y., & McWilliams, J. C. (2009). Circulation and multiple-scale variability  
973 in the southern california bight. *Progress in Oceanography*, *82*(3), 168–190.
- 974 Fasham, M. J. (1993). Modelling the marine biota. In *The global carbon cycle* (pp. 457–504).  
975 Springer.
- 976 Feely, R. A., Okazaki, R. R., Cai, W.-J., Bednaršek, N., Alin, S. R., Byrne, R. H., &  
977 Fassbender, A. (2018). The combined effects of acidification and hypoxia on ph and  
978 aragonite saturation in the coastal waters of the california current ecosystem and the  
979 northern gulf of mexico. *Continental Shelf Research*, *152*, 50–60.
- 980 Fennel, K., & Testa, J. M. (2019). Biogeochemical controls on coastal hypoxia. *Annual*  
981 *Review of Marine Science*, *11*, 105–130.
- 982 Foster, R. A., Kuypers, M. M., Vagner, T., Paerl, R. W., Musat, N., & Zehr, J. P. (2011).  
983 Nitrogen fixation and transfer in open ocean diatom–cyanobacterial symbioses. *The*  
984 *ISME journal*, *5*(9), 1484–1493.
- 985 Galarza, J. A., Carreras-Carbonell, J., Macpherson, E., Pascual, M., Roques, S., Turner,  
986 G. F., & Rico, C. (2009). The influence of oceanographic fronts and early-life-history  
987 traits on connectivity among littoral fish species. *Proceedings of the National Academy*  
988 *of Sciences*, *106*(5), 1473–1478.
- 989 Gruber, N. (2004). The dynamics of the marine nitrogen cycle and its influence on atmo-  
990 spheric co 2 variations. In *The ocean carbon cycle and climate* (pp. 97–148). Springer.
- 991 Gruber, N., Lachkar, Z., Frenzel, H., Marchesiello, P., Münnich, M., McWilliams, J. C., ...  
992 Plattner, G.-K. (2011). Eddy-induced reduction of biological production in eastern  
993 boundary upwelling systems. *Nature geoscience*, *4*(11), 787.
- 994 Howard, M. D., Sutula, M., Caron, D. A., Chao, Y., Farrara, J. D., Frenzel, H., ... Sengupta,  
995 A. (2014). Anthropogenic nutrient sources rival natural sources on small scales in the  
996 coastal waters of the southern california bight. *Limnology and Oceanography*, *59*(1),  
997 285–297.
- 998 Juranek, L., Feely, R., Gilbert, D., Freeland, H., & Miller, L. (2011). Real-time estima-

- 999 tion of ph and aragonite saturation state from argo profiling floats: Prospects for an  
1000 autonomous carbon observing strategy. *Geophysical Research Letters*, *38*(17).
- 1001 Juranek, L., Feely, R., Peterson, W., Alin, S., Hales, B., Lee, K., . . . Peterson, J. (2009).  
1002 A novel method for determination of aragonite saturation state on the continental  
1003 shelf of central oregon using multi-parameter relationships with hydrographic data.  
1004 *Geophysical Research Letters*, *36*(24).
- 1005 Justić, D., Rabalais, N. N., & Turner, R. E. (2005). Coupling between climate variability  
1006 and coastal eutrophication: evidence and outlook for the northern gulf of mexico.  
1007 *Journal of Sea Research*, *54*(1), 25–35.
- 1008 Kahru, M., Kudela, R., Manzano-Sarabia, M., & Mitchell, B. G. (2009). Trends in primary  
1009 production in the california current detected with satellite data. *Journal of Geophysical  
1010 Research: Oceans*, *114*(C2).
- 1011 Kang, X., Zhang, R.-H., & Wang, G. (2017). Effects of different freshwater flux repre-  
1012 sentations in an ocean general circulation model of the tropical pacific. *Science Bul-  
1013 letin*, *62*(5), 345 - 351. Retrieved from [http://www.sciencedirect.com/science/  
1014 article/pii/S2095927317300932](http://www.sciencedirect.com/science/article/pii/S2095927317300932) doi: <https://doi.org/10.1016/j.scib.2017.02.002>
- 1015 Kessouri, F., Bianchi, D., Renault, L., McWilliams, J. C., Frenzel, H., & Deutsch, C. A.  
1016 (2020). Submesoscale currents modulate the seasonal cycle of nutrients and pro-  
1017 ductivity in the california current system. *Global Biogeochemical Cycles*, *34*(10),  
1018 e2020GB006578.
- 1019 Kessouri, F., McLaughlin, K., Sutula, M., Ho, M., McWilliams, J., C, & Bianchi, D.  
1020 (2020, August). *Collection of situ monitoring data in the Southern California Bight  
1021 1950-2017 for model validation*. Zenodo. Retrieved from [https://doi.org/10.5281/  
1022 zenodo.3988574](https://doi.org/10.5281/zenodo.3988574) doi: 10.5281/zenodo.3988574
- 1023 Kessouri, F., McWilliams, C. J., Deutsch, C., Renault, L., Frenzel, H., Bianchi, D., &  
1024 Molemaker, J. (2020, August). *ROMS-BEC oceanic physical and biogeochemical model  
1025 code for the Southern California Current System V2020*. Zenodo. Retrieved from  
1026 <https://doi.org/10.5281/zenodo.3988618> doi: 10.5281/zenodo.3988618
- 1027 Kim, S. Y., Terrill, E. J., Cornuelle, B. D., Jones, B., Washburn, L., Moline, M. A., . . .  
1028 Kosro, P. M. (2011). Mapping the u.s. west coast surface circulation: A multiyear anal-  
1029 ysis of high-frequency radar observations. *Journal of Geophysical Research: Oceans*,  
1030 *116*(C3). Retrieved from [https://agupubs.onlinelibrary.wiley.com/doi/abs/  
1031 10.1029/2010JC006669](https://agupubs.onlinelibrary.wiley.com/doi/abs/10.1029/2010JC006669) doi: <https://doi.org/10.1029/2010JC006669>
- 1032 Kudela, R. M., Howard, M. D., Hayashi, K., & Beck, C. (2017). Evaluation of uptake kinetics  
1033 during a wastewater diversion into nearshore coastal waters in southern california.  
1034 *Estuarine, Coastal and Shelf Science*, *186*, 237–249.
- 1035 Landry, M. R., Ohman, M. D., Goericke, R., Stukel, M. R., & Tsyrklevich, K. (2009).  
1036 Lagrangian studies of phytoplankton growth and grazing relationships in a coastal  
1037 upwelling ecosystem off southern california. *Progress in Oceanography*, *83*(1-4), 208–  
1038 216.
- 1039 Large, W. B. (2006). Surface fluxes for practitioners of global ocean data assimilation. In  
1040 *Ocean weather forecasting* (pp. 229–270). Springer.
- 1041 Large, W. G., McWilliams, J. C., & Doney, S. C. (1994). Oceanic vertical mixing: A review  
1042 and a model with a nonlocal boundary layer parameterization. *Reviews of Geophysics*,  
1043 *32*(4), 363–403.
- 1044 Laufkötter, C., Vogt, M., Gruber, N., Aita-Noguchi, M., Aumont, O., Bopp, L., . . . others  
1045 (2015). Drivers and uncertainties of future global marine primary production in marine  
1046 ecosystem models. *Biogeosciences*, *12*(23), 6955–6984.
- 1047 Laurent, A., Fennel, K., Ko, D. S., & Lehrter, J. (2018). Climate change projected to  
1048 exacerbate impacts of coastal eutrophication in the northern gulf of mexico. *Journal  
1049 of Geophysical Research: Oceans*, *123*(5), 3408–3426.
- 1050 Leinweber, A., Gruber, N., Frenzel, H., Friederich, G., & Chavez, F. (2009). Diurnal carbon  
1051 cycling in the surface ocean and lower atmosphere of santa monica bay, california.  
1052 *Geophysical research letters*, *36*(8).
- 1053 Lévy, M., Ferrari, R., Franks, P. J., Martin, A. P., & Rivière, P. (2012). Bringing physics

- 1054 to life at the submesoscale. *Geophysical Research Letters*, *39*(14).
- 1055 Li, Q. P., Franks, P. J., & Landry, M. R. (2011). Microzooplankton grazing dynamics: pa-  
 1056 rameterizing grazing models with dilution experiment data from the california current  
 1057 ecosystem. *Marine Ecology Progress Series*, *438*, 59–69.
- 1058 Lucas, A. J., Dupont, C. L., Tai, V., Largier, J. L., Palenik, B., & Franks, P. J. (2011). The  
 1059 green ribbon: Multiscale physical control of phytoplankton productivity and commu-  
 1060 nity structure over a narrow continental shelf. *Limnology and Oceanography*, *56*(2),  
 1061 611–626.
- 1062 Lyon, G. S., & Stein, E. D. (2009). How effective has the clean water act been at reducing  
 1063 pollutant mass emissions to the southern california bight over the past 35 years?  
 1064 *Environmental monitoring and assessment*, *154*(1-4), 413.
- 1065 Mahadevan, A. (2016). The impact of submesoscale physics on primary productivity of  
 1066 plankton. *Annual Review of Marine Science*, *8*, 161–184.
- 1067 Mahowald, N. M., Yoshioka, M., Collins, W. D., Conley, A. J., Fillmore, D. W., & Coleman,  
 1068 D. B. (2006). Climate response and radiative forcing from mineral aerosols during the  
 1069 last glacial maximum, pre-industrial, current and doubled-carbon dioxide climates.  
 1070 *Geophysical Research Letters*, *33*(20).
- 1071 Mantyla, A. W., Bograd, S. J., & Venrick, E. L. (2008). Patterns and controls of chlorophyll-  
 1072 a and primary productivity cycles in the southern california bight. *Journal of Marine*  
 1073 *Systems*, *73*(1-2), 48–60.
- 1074 Marchesiello, P., McWilliams, J. C., & Shchepetkin, A. (2001). Open boundary conditions  
 1075 for long-term integration of regional oceanic models. *Ocean modelling*, *3*(1-2), 1–20.
- 1076 Marchesiello, P., McWilliams, J. C., & Shchepetkin, A. (2003). Equilibrium structure and  
 1077 dynamics of the california current system. *Journal of physical Oceanography*, *33*(4),  
 1078 753–783.
- 1079 Maréchal, D. (2004). A soil-based approach to rainfall-runoff modelling in ungauged catch-  
 1080 ments for england and wales.
- 1081 Marmorino, G. O., Smith, G. B., Miller, W. D., & Bowles, J. (2010). Detection of a buoy-  
 1082 ant coastal wastewater discharge using airborne hyperspectral and infrared imagery.  
 1083 *Journal of Applied Remote Sensing*, *4*(1), 043502.
- 1084 Mason, E., Molemaker, J., Shchepetkin, A. F., Colas, F., McWilliams, J. C., & Sangrà, P.  
 1085 (2010). Procedures for offline grid nesting in regional ocean models. *Ocean modelling*,  
 1086 *35*(1-2), 1–15.
- 1087 McClatchie, S. (2016). *Regional fisheries oceanography of the california current system*.  
 1088 Springer.
- 1089 McGillicuddy Jr, D. J. (2016). Mechanisms of physical-biological-biogeochemical interaction  
 1090 at the oceanic mesoscale.
- 1091 McLaughlin, K., Dickson, A., Weisberg, S. B., Coale, K., Elrod, V., Hunter, C., ... others  
 1092 (2017). An evaluation of isfet sensors for coastal ph monitoring applications. *Regional*  
 1093 *Studies in Marine Science*, *12*, 11–18.
- 1094 McLaughlin, K., Nezlin, N. P., Howard, M. D., Beck, C. D., Kudela, R. M., Mengel, M. J.,  
 1095 & Robertson, G. L. (2017). Rapid nitrification of wastewater ammonium near coastal  
 1096 ocean outfalls, southern california, usa. *Estuarine, Coastal and Shelf Science*, *186*,  
 1097 263–275.
- 1098 McLaughlin, K., Nezlin, N. P., Weisberg, S. B., Dickson, A. G., Booth, J. A. T., Cash,  
 1099 C. L., ... others (2018). Seasonal patterns in aragonite saturation state on the  
 1100 southern california continental shelf. *Continental Shelf Research*, *167*, 77–86.
- 1101 McWilliams, J. C. (2007). Irreducible imprecision in atmospheric and oceanic simulations.  
 1102 *Proceedings of the National Academy of Sciences*, *104*(21), 8709–8713.
- 1103 McWilliams, J. C. (2016). Submesoscale currents in the ocean. *Proceedings of the Royal*  
 1104 *Society A: Mathematical, Physical and Engineering Sciences*, *472*(2189), 20160117.
- 1105 Middelburg, J. J., Soetaert, K., Herman, P. M., & Heip, C. H. (1996). Denitrification in  
 1106 marine sediments: A model study. *Global Biogeochemical Cycles*, *10*(4), 661–673.
- 1107 Moll, A., & Radach, G. (2003). Review of three-dimensional ecological modelling related to  
 1108 the north sea shelf system: Part 1: models and their results. *Progress in Oceanography*,

- 1109 57(2), 175–217.
- 1110 Montégut, C. B., Vialard, J., Shenoi, S. S., Shankar, D., Durand, F., Ethé, C., & Madec, G.  
1111 (2007). Simulated seasonal and interannual variability of the mixed layer heat budget  
1112 in the northern indian ocean. *Journal of Climate*, 20(13), 3249–3268.
- 1113 Moore, J. K., Doney, S. C., & Lindsay, K. (2004). Upper ocean ecosystem dynamics and iron  
1114 cycling in a global three-dimensional model. *Global Biogeochemical Cycles*, 18(4).
- 1115 Nagai, T., Gruber, N., Frenzel, H., Lachkar, Z., McWilliams, J. C., & Plattner, G.-K.  
1116 (2015). Dominant role of eddies and filaments in the offshore transport of carbon and  
1117 nutrients in the California Current System. *Journal of Geophysical Research: Oceans*,  
1118 120(8), 5318–5341.
- 1119 Nash, J., & Sutcliffe, J. (1970). River flow forecasting through conceptual models part i —  
1120 a discussion of principles. *Journal of Hydrology*, 10(3), 282 - 290. Retrieved from  
1121 <http://www.sciencedirect.com/science/article/pii/0022169470902556> doi:  
1122 [https://doi.org/10.1016/0022-1694\(70\)90255-6](https://doi.org/10.1016/0022-1694(70)90255-6)
- 1123 Nezlin, N. P., McLaughlin, K., Booth, J. A. T., Cash, C. L., Diehl, D. W., Davis, K. A.,  
1124 ... others (2018). Spatial and temporal patterns of chlorophyll concentration in the  
1125 southern california bight. *Journal of Geophysical Research: Oceans*, 123(1), 231–245.
- 1126 Nezlin, N. P., Sutula, M. A., Stumpf, R. P., & Sengupta, A. (2012). Phytoplankton  
1127 blooms detected by seawifs along the central and southern california coast. *Journal*  
1128 *of Geophysical Research: Oceans*, 117(C7).
- 1129 Ocean Protection Council. (2018). *State of california ocean acidification action plan*. Re-  
1130 trieved from <https://www.opc.ca.gov/oa-action-plan/>
- 1131 Regaudie-de Gioux, A., Lasternas, S., Agustí, S., & Duarte, C. M. (2014). Comparing  
1132 marine primary production estimates through different methods and development of  
1133 conversion equations. *Frontiers in Marine Science*, 1, 19.
- 1134 Renault, L., Hall, A., & McWilliams, J. C. (2016). Orographic shaping of us west coast  
1135 wind profiles during the upwelling season. *Climate Dynamics*, 46(1-2), 273–289.
- 1136 Renault, L., Masson, S., Arsouze, T., Madec, G., & McWilliams, J. C. (2020). Recipes  
1137 for how to force oceanic model dynamics. *Journal of Advances in Modeling Earth*  
1138 *Systems*, 12(2), e2019MS001715.
- 1139 Renault, L., McWilliams, J. C., Jousse, A., Deutsch, C., Frenzel, H., Kessouri, F., & Chen,  
1140 R. (2020). The physical structure and behavior of the california current system.  
1141 *bioRxiv*.
- 1142 Renault, L., Molemaker, M. J., Gula, J., Masson, S., & McWilliams, J. C. (2016). Control  
1143 and stabilization of the gulf stream by oceanic current interaction with the atmosphere.  
1144 *Journal of Physical Oceanography*, 46(11), 3439–3453.
- 1145 Renault, L., Molemaker, M. J., McWilliams, J. C., Shchepetkin, A. F., Lemarié, F., Chelton,  
1146 D., ... Hall, A. (2016). Modulation of wind work by oceanic current interaction with  
1147 the atmosphere. *Journal of Physical Oceanography*, 46(6), 1685–1704.
- 1148 Sailley, S., Vogt, M., Doney, S., Aita, M., Bopp, L., Buitenhuis, E., ... Yamanaka, Y.  
1149 (2013). Comparing food web structures and dynamics across a suite of global marine  
1150 ecosystem models. *Ecological Modelling*, 261, 43–57.
- 1151 Savchuk, O. P., & Wulff, F. (2007). Modeling the baltic sea eutrophication in a decision  
1152 support system. *AMBIO: A Journal of the Human Environment*, 36(2), 141–148.
- 1153 Seegers, B. N., Birch, J. M., Marin III, R., Scholin, C. A., Caron, D. A., Seubert, E. L.,  
1154 ... Jones, B. H. (2015). Subsurface seeding of surface harmful algal blooms observed  
1155 through the integration of autonomous gliders, moored environmental sample proces-  
1156 sors, and satellite remote sensing in southern c alifornia. *Limnology and Oceanography*,  
1157 60(3), 754–764.
- 1158 Shchepetkin, A. F., & McWilliams, J. C. (2005). The regional oceanic modeling system  
1159 (roms): a split-explicit, free-surface, topography-following-coordinate oceanic model.  
1160 *Ocean modelling*, 9(4), 347–404.
- 1161 Shchepetkin, A. F., & McWilliams, J. C. (2009). Correction and commentary for “Ocean  
1162 forecasting in terrain-following coordinates: Formulation and skill assessment of the  
1163 regional ocean modeling system” by Haidvogel et al., *J. Comp. Phys.* 227, pp. 3595–

- 1164 3624. *Journal of Computational Physics*, 228(24), 8985–9000.
- 1165 Shchepetkin, A. F., & McWilliams, J. C. (2011). Accurate boussinesq oceanic modeling  
1166 with a practical, “stiffened” equation of state. *Ocean Modelling*, 38(1-2), 41–70.
- 1167 Skamarock, W. C., & Klemp, J. B. (2008). A time-split nonhydrostatic atmospheric model  
1168 for weather research and forecasting applications. *Journal of Computational Physics*,  
1169 227(7), 3465–3485.
- 1170 Sutton, A., Wanninkhof, R., Sabine, C., Feely, R., Cronin, M., & Weller, R. (2017). Variabil-  
1171 ity and trends in surface seawater pco2 and co2 flux in the pacific ocean. *Geophysical  
1172 Research Letters*, 44(11), 5627–5636.
- 1173 Sutula, M., Ho, M., Sengupta, A., Kessouri, F., McLaughlin, K., McCune, K., & Bianchi,  
1174 D. (2021a, January). *A Baseline of Terrestrial Freshwater and Nitrogen Fluxes to  
1175 the Southern California Bight, USA*. Zenodo. Retrieved from [https://doi.org/  
1176 10.5281/zenodo.4448224](https://doi.org/10.5281/zenodo.4448224) doi: 10.5281/zenodo.4448224
- 1177 Sutula, M., Ho, M., Sengupta, A., Kessouri, F., McLaughlin, K., McCune, K., & Bianchi,  
1178 D. (2021b). Dataset of terrestrial fluxes of freshwater, nutrients, carbon, and iron to  
1179 the southern california bight, u.s.a. *Data in Brief*, 106802. Retrieved from [https://  
1180 www.sciencedirect.com/science/article/pii/S235234092100086X](https://www.sciencedirect.com/science/article/pii/S235234092100086X) doi: [https://  
1181 doi.org/10.1016/j.dib.2021.106802](https://doi.org/10.1016/j.dib.2021.106802)
- 1182 Taylor, B. L., Wade, P. R., De Master, D. P., & Barlow, J. (2000). Incorporating uncertainty  
1183 into management models for marine mammals. *Conservation Biology*, 14(5), 1243–  
1184 1252.
- 1185 Teel, E. N., Liu, X., Seegers, B. N., Ragan, M. A., Haskell, W. Z., Jones, B., & Levine,  
1186 N. M. (2018). Contextualizing time-series data: quantification of short-term regional  
1187 variability in the san pedro channel using high-resolution in situ glider data.
- 1188 Todd, R. E., Rudnick, D. L., Davis, R. E., & Ohman, M. D. (2011). Underwater gliders  
1189 reveal rapid arrival of el niño effects off california’s coast. *Geophysical Research Letters*,  
1190 38(3).
- 1191 Uchiyama, Y., Idica, E. Y., McWilliams, J. C., & Stolzenbach, K. D. (2014). Wastewater  
1192 effluent dispersal in southern california bays. *Continental Shelf Research*, 76, 36–52.
- 1193 Wanninkhof, R. (1992). Relationship between wind speed and gas exchange over the ocean.  
1194 *Journal of Geophysical Research: Oceans*, 97(C5), 7373–7382.
- 1195 Warrick, J. A., DiGiacomo, P. M., Weisberg, S. B., Nezlin, N. P., Mengel, M., Jones, B. H.,  
1196 ... Farnsworth, K. L. (2007). River plume patterns and dynamics within the southern  
1197 california bight. *Continental Shelf Research*, 27(19), 2427–2448.
- 1198 Weisberg, S. B., Bednaršek, N., Feely, R. A., Chan, F., Boehm, A. B., Sutula, M., ...  
1199 Newton, J. A. (2016). Water quality criteria for an acidifying ocean: Challenges and  
1200 opportunities for improvement. *Ocean & Coastal Management*, 126, 31–41.
- 1201 Welch, B. L. (1947, 01). THE GENERALIZATION OF ‘STUDENT’S’ PROBLEM  
1202 WHEN SEVERAL DIFFERENT POPULATION VARIANCES ARE INVOLVED.  
1203 *Biometrika*, 34(1-2), 28-35. Retrieved from [https://doi.org/10.1093/biomet/  
1204 34.1-2.28](https://doi.org/10.1093/biomet/34.1-2.28) doi: 10.1093/biomet/34.1-2.28
- 1205 Winant, C., Dever, E. P., & Hendershott, M. (2003). Characteristic patterns of shelf circula-  
1206 tion at the boundary between central and southern california. *Journal of Geophysical  
1207 Research: Oceans*, 108(C2).
- 1208 Zheng, G., & DiGiacomo, P. M. (2017). Uncertainties and applications of satellite-derived  
1209 coastal water quality products. *Progress in oceanography*, 159, 45–72.

1210  
1211  
1212  
1213

**Supporting Information for “Configuration and  
validation of an oceanic physical and biogeochemical  
model to investigate coastal eutrophication in the  
Southern California Bight”**

1214

**Contents of this file**

1215  
1216

1. Tables S1 to S4
2. Figures S1 to S24

Ventura/Oxnard								
Temperature								
	H	Correlation Coefficient	p-value	Cost Function	Percentage Bias	Ratio of Standard Deviations	Nash-Sutcliffe Model Efficiency	Number of observations
Winter	0 E	0.95 E	2E-05 E	0.06 E	-0.04 E	1.11 G	0.77 E	469
Spring	0 E	0.98 E	7E-07 E	0.09 E	-0.09 E	0.80 G	0.59 G	468
Summer	0 E	0.98 E	1E-06 E	0.04 E	-0.02 E	1.08 E	0.94 E	468
Fall	0 E	0.89 G	5E-04 E	0.09 E	-0.08 E	0.97 E	0.50 R	469
All Seasons	0 E	0.95 E	3E-05 E	0.08 E	-0.06 E	1.03 E	0.74 E	1874
Oxygen								
	H	Correlation Coefficient	p-value	Cost Function	Percentage Bias	Ratio of Standard Deviations	Nash-Sutcliffe Model Efficiency	Number of observations
Winter	0 E	0.98 E	1E-06 E	0.14 E	-0.09 E	1.20 R	0.77 E	469
Spring	0 E	0.92 E	1E-04 E	0.25 E	-0.21 R	1.06 E	0.47 R	454
Summer	0 E	0.99 E	1E-09 E	0.07 E	0.08 E	1.03 E	0.84 E	468
Fall	0 E	0.98 E	1E-06 E	0.19 E	-0.14 G	1.52 P	0.44 R	469
All Seasons	0 E	0.98 E	1E-06 E	0.14 E	-0.010 G	1.20 R	0.73 E	1860
Chlorophyll-a								
	H	Correlation Coefficient	p-value	Cost Function	Percentage Bias	Ratio of Standard Deviations	Nash-Sutcliffe Model Efficiency	Number of observations
Winter	0 E	0.99 E	1E-08 E	0.43 E	-0.06 E	0.90 E	0.96 E	469
Spring	0 E	0.97 E	3E-06 E	0.86 E	-0.42 P	0.51 P	-0.47 P	468
Summer	0 E	0.96 E	1E-05 E	0.59 E	-0.04 E	0.64 R	0.51 G	468
Fall	0 E	0.94 E	5E-05 E	0.53 E	0.20 R	0.71 R	0.50 R	469
All Seasons	0 E	0.99 E	9E-11 E	0.50 E	-0.01 E	0.71 R	0.79 E	1874
pH								
	H	Correlation Coefficient	p-value	Cost Function	Percentage Bias	Ratio of Standard Deviations	Nash-Sutcliffe Model Efficiency	Number of observations
Winter	0 E	0.99 E	2E-08 E	0.01 E	0.01 E	0.62 R	0.57 G	455
Spring	0 E	0.97 E	2E-07 E	0.01 E	-0.01 E	1.45 P	0.25 R	454
Summer	0 E	0.97 E	2E-06 E	0.01 E	0.01 E	1.06 E	0.84 E	468
Fall	0 E	0.98 E	6E-07 E	0.01 E	0.01 E	1.43 P	0.75 E	467
All Seasons	0 E	0.98 E	1E-06 E	0.01 E	-0.01 E	1.13 G	0.89 E	1844
Ammonia								
	H	Correlation Coefficient	p-value	Cost Function	Percentage Bias	Ratio of Standard Deviations	Nash-Sutcliffe Model Efficiency	Number of observations
Winter	0 E	0.86 G	0.34 P	0.53 E	0.24 R	1.56 P	0.58 G	11
Spring	0 E	0.99 E	0.02 E	1.40 G	-1.87 P	0.36 P	-10.52 P	12
Summer	0 E	0.92 E	0.25 P	2.59 R	0.28 R	1.62 P	0.67 E	12
Fall	0 E	0.92 E	0.26 P	4.42 P	-2.77 P	0.35 P	-10.48 P	12
All Seasons	0 E	0.89 G	0.04 E	0.77 E	-0.49 P	0.91 E	0.01 P	47

Table S1: Statistical comparison of vertical profiles of temperature, dissolved oxygen, chlorophyll *a*, pH, and ammonium concentration at Ventura/Oxnard (City of Oxnard stations) monitoring region. Letters next to numbers indicate model performance: E = Excellent, G = very good, R = reasonable, P = Poor.

Palos Verdes								
Temperature								
	H	Correlation Coefficient	p-value	Cost Function	Percentage Bias	Ratio of Standard Deviations	Nash-Sutcliffe Model Efficiency	Number of observations
Winter	0 E	0.95 E	2E-05 E	0.04 E	-0.01 E	1.13 G	0.87 E	469
Spring	0 E	0.94 E	6E-05 E	0.24 E	-0.11 G	0.75 R	0.19 P	466
Summer	0 E	0.98 E	7E-07 E	0.03 E	0.03 E	1.19 G	0.91 E	466
Fall	0 E	0.88 G	7E-04 E	0.11 E	-0.11 G	0.75 R	-0.27 P	468
All Seasons	0 E	0.94 E	5E-05 E	0.07 E	-0.06 E	0.98 E	0.74 E	1869
Oxygen								
	H	Correlation Coefficient	p-value	Cost Function	Percentage Bias	Ratio of Standard Deviations	Nash-Sutcliffe Model Efficiency	Number of observations
Winter	0 E	0.99 E	9E-09 E	0.03 E	0.02 E	1.05 E	0.94 E	469
Spring	0 E	0.83 G	3E-03 E	0.24 E	-0.22 R	0.87 G	0.01 P	466
Summer	0 E	0.97 E	2E-06 E	0.08 E	0.08 E	0.87 G	0.69 E	466
Fall	0 E	0.97 E	7E-04 E	0.08 E	-0.06 E	1.14 G	0.76 E	467
All Seasons	0 E	0.98 E	1E-06 E	0.06 E	-0.05 E	0.97 E	0.88 E	1868
Chlorophyll-a								
	H	Correlation Coefficient	p-value	Cost Function	Percentage Bias	Ratio of Standard Deviations	Nash-Sutcliffe Model Efficiency	Number of observations
Winter	0 E	0.75 R	0.01 E	0.70 E	0.25 R	0.83 G	0.19 P	469
Spring	0 E	0.83 G	2E-03 E	0.72 E	0.06 E	1.01 E	0.65 E	466
Summer	0 E	0.67 R	0.04 E	0.73 E	0.38 R	1.28 R	0.17 P	466
Fall	0 E	0.99 E	1E-10 E	0.48 E	0.25 R	1.01 E	0.91 E	468
All Seasons	0 E	0.95 E	2E-05 E	0.55 E	0.30 R	1.00 E	0.70 E	1869
pH								
	H	Correlation Coefficient	p-value	Cost Function	Percentage Bias	Ratio of Standard Deviations	Nash-Sutcliffe Model Efficiency	Number of observations
Winter	1 P	0.99 E	2E-07 E	0.03 E	-0.03 E	1.36 R	-2.96 P	469
Spring	0 E	0.84 G	2E-03 E	0.01 E	0.01 E	1.44 P	0.67 E	466
Summer	1 P	0.99 E	2E-09 E	0.03 E	0.03 E	1.62 P	-2.80 P	466
Fall	1 P	0.96 E	9E-06 E	0.02 E	0.02 E	1.54 P	-1.29 P	468
All Seasons	0 E	0.96 E	1E-05 E	0.01 E	0.01 E	1.50 P	0.73 E	1869
Ammonia								
	H	Correlation Coefficient	p-value	Cost Function	Percentage Bias	Ratio of Standard Deviations	Nash-Sutcliffe Model Efficiency	Number of observations
Winter	N/A	N/A	N/A	N/A	N/A	N/A	N/A	0
Spring	N/A	N/A	N/A	N/A	N/A	N/A	N/A	0
Summer	0 E	0.82 G	0.18 P	0.31 E	0.15 G	1.05 E	0.53 G	18
Fall	0 E	0.79 R	0.21 P	0.30 E	0.32 R	1.38 R	-0.15 P	18
All Seasons	0 E	0.84 G	0.16 P	0.30 E	0.32 R	1.34 R	-0.01 P	36

Table S2: Same as Table S1 for Palos Verdes (LACSD stations) monitoring region.

Orange County								
Temperature								
	H	Correlation Coefficient	p-value	Cost Function	Percentage Bias	Ratio of Standard Deviations	Nash-Sutcliffe Model Efficiency	Number of observations
Winter	0 E	0.96 E	1E-05 E	0.05 E	-0.01 E	1.27 R	0.84 E	160
Spring	0 E	0.95 E	3E-05 E	0.11 E	-0.11 G	0.81 G	0.44 R	533
Summer	0 E	0.99 E	2E-08 E	0.02 E	-0.01 E	0.96 E	0.98 E	533
Fall	0 E	0.92 E	2E-04 E	0.08 E	-0.07 E	1.06 E	0.66 E	536
All Seasons	0 E	0.95 E	3E-05 E	0.07 E	-0.05 E	1.07 E	0.79 E	1762
Oxygen								
	H	Correlation Coefficient	p-value	Cost Function	Percentage Bias	Ratio of Standard Deviations	Nash-Sutcliffe Model Efficiency	Number of observations
Winter	0 E	0.98 E	1E-06 E	0.14 E	-0.12 G	1.03 E	0.67 E	150
Spring	0 E	0.90 E	4E-04 E	0.19 E	-0.16 G	0.96 E	0.51 G	533
Summer	0 E	0.99 E	5E-08 E	0.07 E	0.07 E	0.91 E	0.80 E	534
Fall	0 E	0.92 E	4E-07 E	0.09 E	-0.02 E	1.06 E	0.80 E	536
All Seasons	0 E	0.95 E	9E-06 E	0.09 E	-0.06 E	1.07 E	0.81 E	1753
Chlorophyll-a								
	H	Correlation Coefficient	p-value	Cost Function	Percentage Bias	Ratio of Standard Deviations	Nash-Sutcliffe Model Efficiency	Number of observations
Winter	0 E	0.98 E	8E-07 E	0.97 E	0.53 P	2.25 P	0.49 R	160
Spring	0 E	0.74 R	0.02 E	2.24 R	0.29 R	2.12 P	0.46 R	533
Summer	0 E	0.94 E	7E-05 E	0.57 E	-0.16 G	0.83 G	0.76 E	535
Fall	0 E	0.92 E	1E-04 E	0.55 E	0.41 P	1.32 R	0.62 G	536
All Seasons	0 E	0.91 E	3E-04 E	0.47 E	0.33 R	1.80 P	0.63 G	1764
pH								
	H	Correlation Coefficient	p-value	Cost Function	Percentage Bias	Ratio of Standard Deviations	Nash-Sutcliffe Model Efficiency	Number of observations
Winter	0 E	0.98 E	1E-06 E	0.01 E	0 E	1.26 R	0.88 E	160
Spring	0 E	0.79 R	0.01 E	0.01 E	-0.01 E	1.32 R	0.28 R	533
Summer	1 P	0.96 E	2E-05 E	0.02 E	0.02 E	1.32 R	-1.13 P	534
Fall	1 P	0.98 E	1E-06 E	0.03 E	-0.03 E	2.02 P	-2.62 P	536
All Seasons	0 E	0.93 E	9E-05 E	0.01 E	-0.01 E	1.43 P	0.51 G	1763
Ammonia								
	H	Correlation Coefficient	p-value	Cost Function	Percentage Bias	Ratio of Standard Deviations	Nash-Sutcliffe Model Efficiency	Number of observations
Winter	N/A	N/A	N/A	N/A	N/A	N/A	N/A	0
Spring	N/A	N/A	N/A	N/A	N/A	N/A	N/A	0
Summer	1 P	0.97 E	0.14 P	0.86 E	0.83 P	3.89 P	-2.38 P	48
Fall	0 E	0.71 R	0.50 P	0.43 E	0.37 R	0.44 P	-8.71 P	48
All Seasons	1 P	0.76 R	0.14 P	0.62 E	0.63 P	2.36 P	-1.67 P	96

Table S3: Same as Table S1 for Orange County (OCSD stations) monitoring region.

San Diego								
Temperature								
	H	Correlation Coefficient	p-value	Cost Function	Percentage Bias	Ratio of Standard Deviations	Nash-Sutcliffe Model Efficiency	Number of observations
Winter	0 E	0.98 E	3E-08 E	0.02 E	-0.01 E	0.92 E	0.95 E	875
Spring	0 E	0.93 E	1E-05 E	0.09 E	-0.09 E	0.77 R	0.30 R	870
Summer	0 E	0.98 E	5E-08 E	0.04 E	-0.01 E	0.99 E	0.94 E	872
Fall	0 E	0.92 E	3E-05 E	0.08 E	-0.08 E	0.79 R	0.29 R	752
All Seasons	0 E	0.98 E	4E-07 E	0.05 E	-0.05 E	0.83 G	0.70 E	3369
Oxygen								
	H	Correlation Coefficient	p-value	Cost Function	Percentage Bias	Ratio of Standard Deviations	Nash-Sutcliffe Model Efficiency	Number of observations
Winter	0 E	0.96 E	1E-06 E	0.11 E	-0.09 E	1.05 E	0.74 E	875
Spring	1 P	0.87 G	3E-04 E	0.33 E	-0.32 R	0.87 G	-0.45 P	870
Summer	0 E	0.99 E	5E-12 E	0.27 E	-0.20 R	1.47 P	0.51 G	872
Fall	0 E	0.92 E	3E-05 E	0.22 E	-0.16 G	1.59 P	0.37 R	752
All Seasons	0 E	0.97 E	4E-07 E	0.18 E	-0.16 G	1.18 G	0.55 G	3369
Chlorophyll-a								
	H	Correlation Coefficient	p-value	Cost Function	Percentage Bias	Ratio of Standard Deviations	Nash-Sutcliffe Model Efficiency	Number of observations
Winter	0 E	0.99 E	6E-09 E	0.51 E	0.60 P	2.59 P	0.39 R	868
Spring	0 E	0.94 E	4E-06 E	0.84 E	0.36 R	1.59 P	0.73 E	866
Summer	0 E	0.99 E	6E-09 E	0.27 E	0.18 G	1.28 R	0.90 E	870
Fall	0 E	0.89 G	2E-04 E	0.35 E	0.43 P	2.05 P	0.50 R	728
All Seasons	0 E	0.98 E	9E-09 E	0.57 E	0.39 R	1.66 P	0.70 E	3332
pH								
	H	Correlation Coefficient	p-value	Cost Function	Percentage Bias	Ratio of Standard Deviations	Nash-Sutcliffe Model Efficiency	Number of observations
Winter	0 E	0.99 E	5E-09 E	0.01 E	-0.01 E	1.07 E	0.49 R	875
Spring	1 P	0.91 E	5E-05 E	0.02 E	-0.02 E	1.41 P	-0.96 P	872
Summer	1 P	0.99 E	1E-09 E	0.02 E	-0.02 E	2.32 P	-0.07 P	844
Fall	1 P	0.98 E	2E-04 E	0.01 E	-0.01 E	1.77 P	-0.14 P	752
All Seasons	1 P	0.98 E	6E-08 E	0.02 E	-0.02 E	1.59 P	-0.18 P	3343
Ammonia								
	H	Correlation Coefficient	p-value	Cost Function	Percentage Bias	Ratio of Standard Deviations	Nash-Sutcliffe Model Efficiency	Number of observations
Winter	N/A	N/A	N/A	N/A	N/A	N/A	N/A	0
Spring	N/A	N/A	N/A	N/A	N/A	N/A	N/A	0
Summer	N/A	N/A	N/A	N/A	N/A	N/A	N/A	0
Fall	N/A	N/A	N/A	N/A	N/A	N/A	N/A	0
All Seasons	N/A	N/A	N/A	N/A	N/A	N/A	N/A	0

Table S4: Same as Table S1 for San Diego (City of San Diego stations) monitoring region.

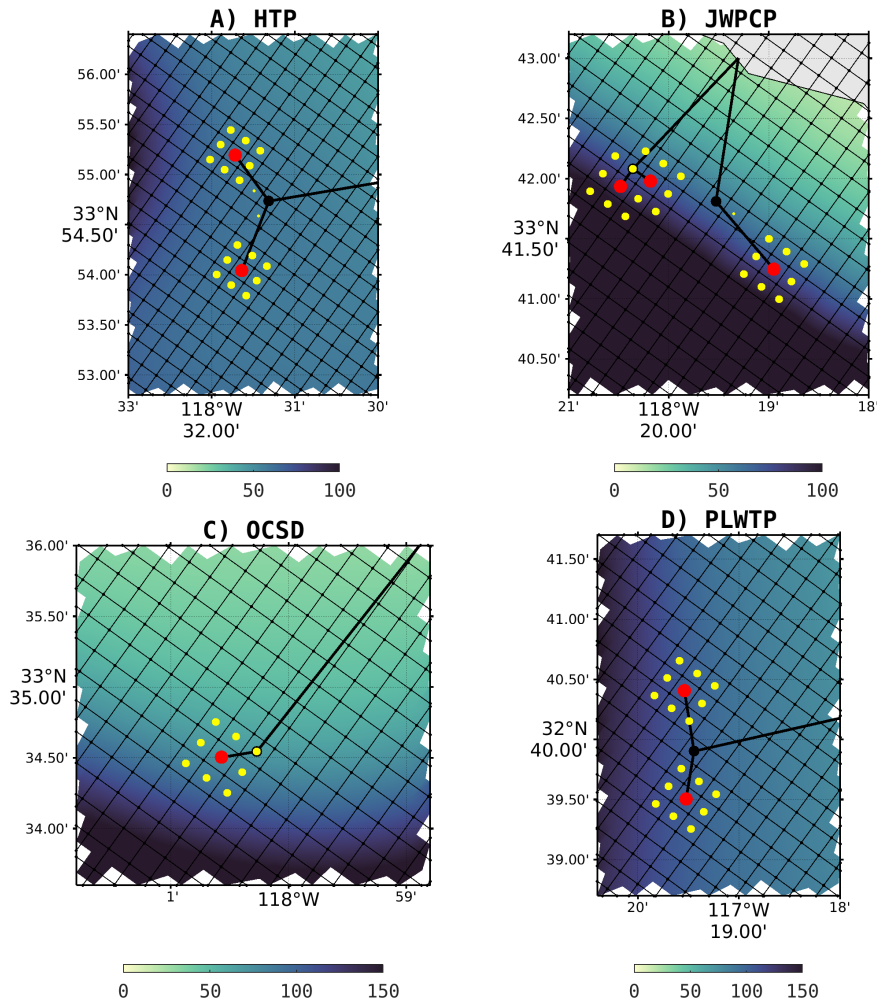


Figure S1: Spatial distribution of the point sources to simulate and to dilute the freshwater, nutrients and organic matter fluxes for the 4 majors POTW underwater outfalls locations. Color scale is bathymetry. Vertically integrated, the grid cells with the red dots discharge 4/9 of the respective flow at each diffuser, the grid cells with yellow dots north, south, east and west of the red dots discharge 1/9 of the discharge, and the yellow dots in the corners discharge 1/36 of the volume flux.

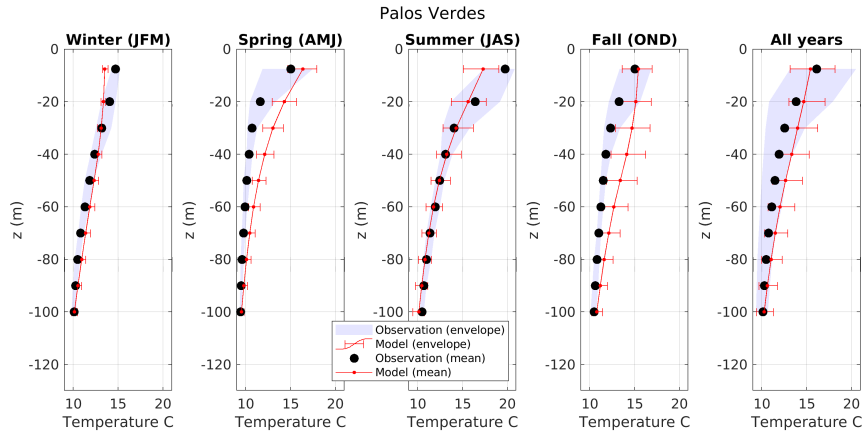


Figure S2: Seasonal profiles of average temperature off of Palos Verdes. The red line and red bars are the spatial and temporal means and the variability from the model. The black dots and the gray shade are the spatial and temporal mean and the variability from *in situ* data (LACSD stations). These profiles are showing agreement on intensity, seasonality and shape of the vertical profile with exceptionally high concentrations at mid-depth.

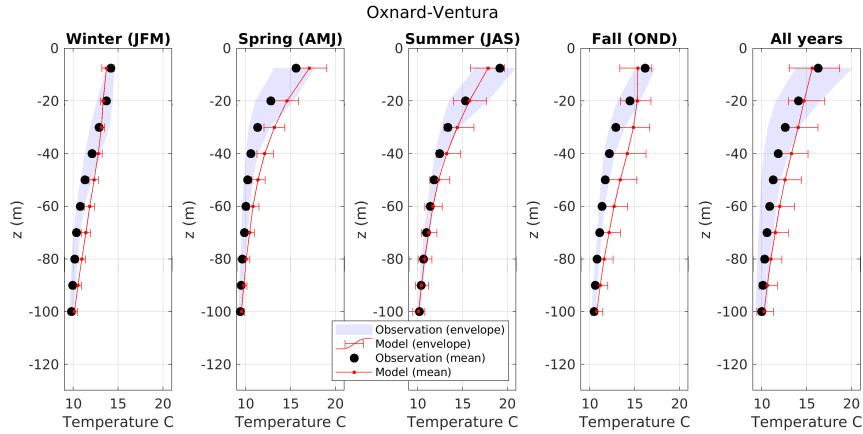


Figure S3: Same as Fig S2 for Oxnard/Ventura using City of Oxnard stations.

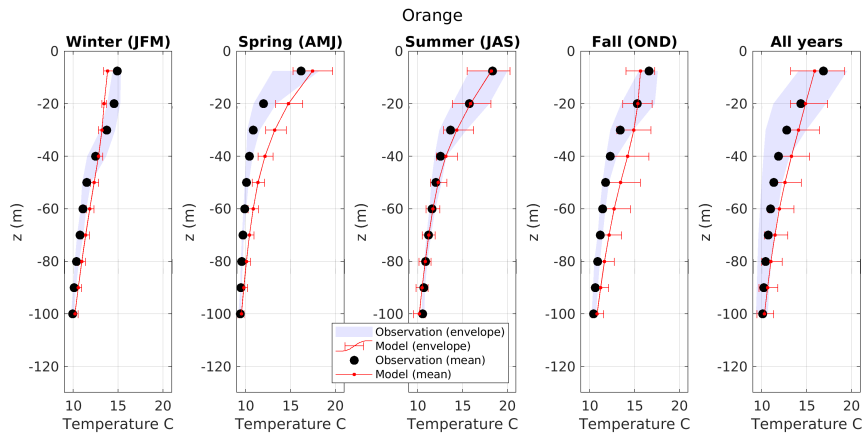


Figure S4: Same as Fig S2 for Orange County using OCSD stations.

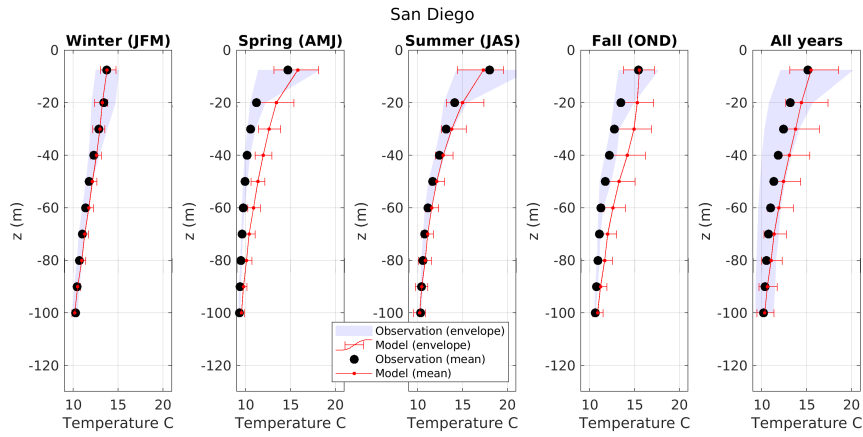


Figure S5: Same as Fig S2 for San Diego using City of San Diego stations.

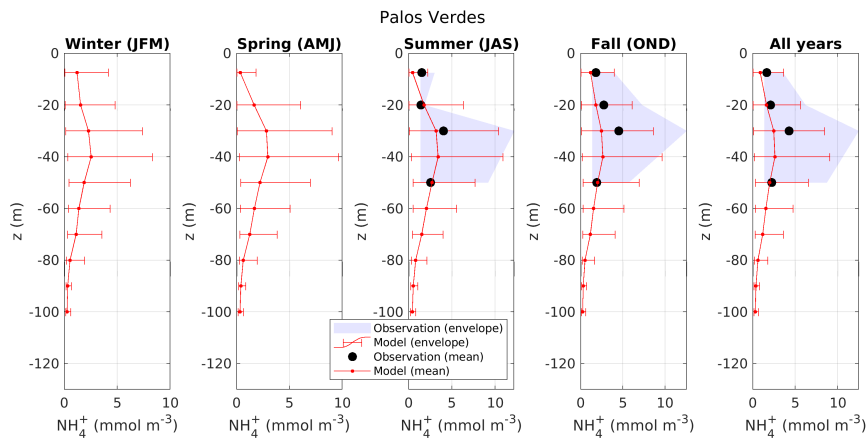


Figure S6: Seasonal profiles of average ammonium concentration off of Palos Verdes. The red line and red bars are the spatial and temporal means and the variability from the model. The black dots and the gray shade are the spatial and temporal mean and the variability from *in situ* data (LACSD stations). These profiles are showing agreement on intensity, seasonality and shape of the vertical profile with exceptionally high concentrations at mid-depth.

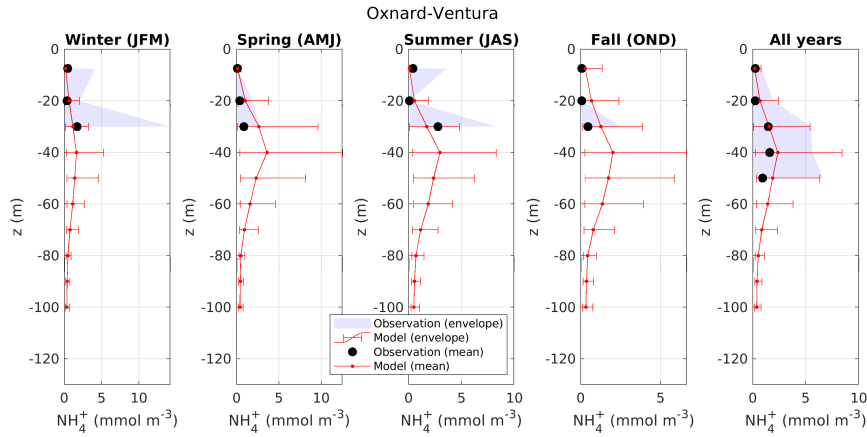


Figure S7: Same as Fig S6 for Oxnard/Ventura using City of Oxnard stations

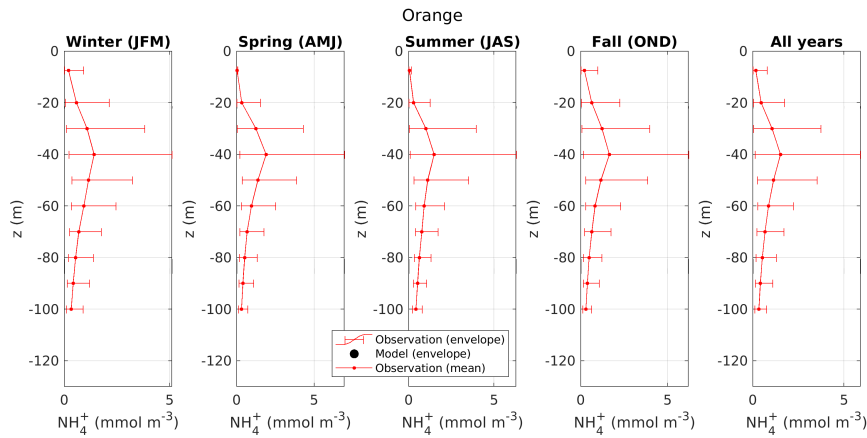


Figure S8: Same as Fig S6 for Orange County using OCSD stations.

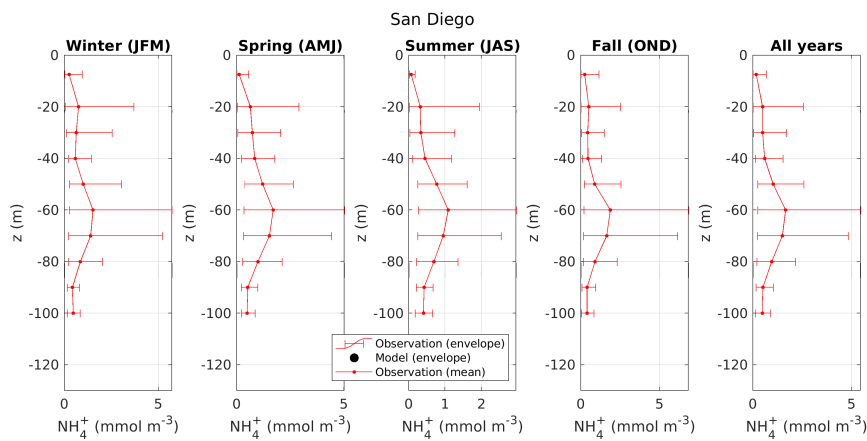


Figure S9: Same as Fig S6 for San Diego using City of San Diego stations. *In situ* data are missing but we wanted to report out the depth of maximum anthropogenic plume, in contrary to other subregion, in San Diego area, the plume rarely reaches 20 m.

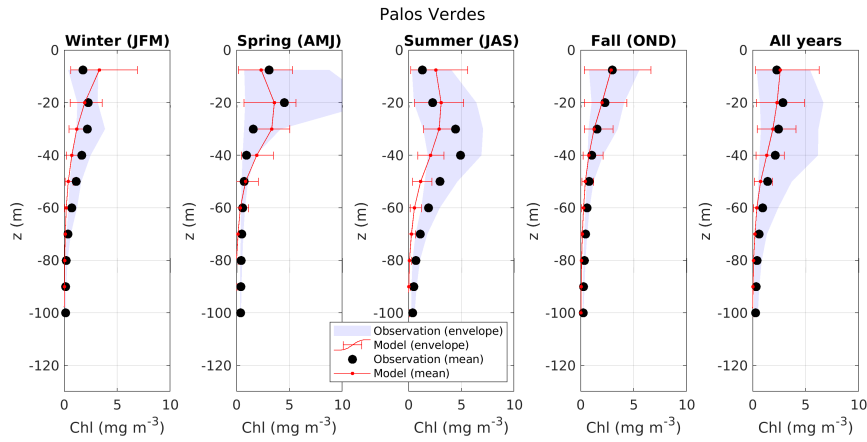


Figure S10: Seasonal profiles of average chlorophyll *a* concentration off of Palos Verdes. The red line and red bars are the spatial and temporal means and the variability from the model. The black dots and the gray shade are the spatial and temporal mean and the variability from *in situ* data (LACSD stations). These profiles are showing agreement on intensity, seasonality and shape of the vertical profile with exceptionally high concentrations at mid-depth.

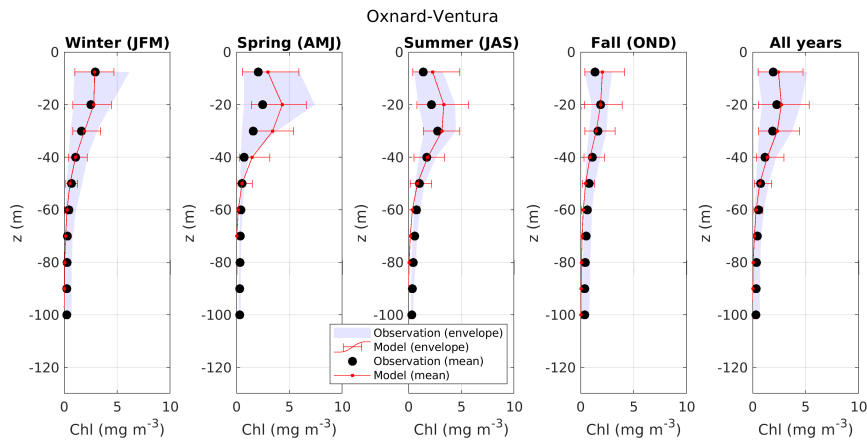


Figure S11: Same as Fig S10 for Oxnard/Ventura using City of Oxnard stations.

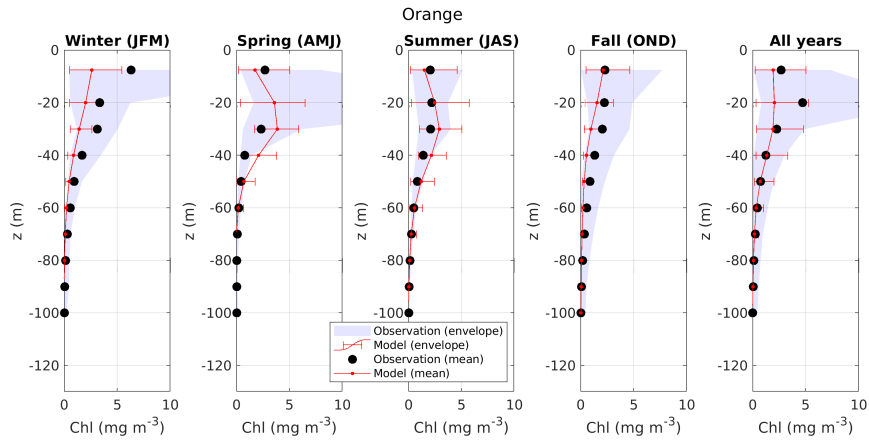


Figure S12: Same as Fig S10 for Orange County using OCSD stations.

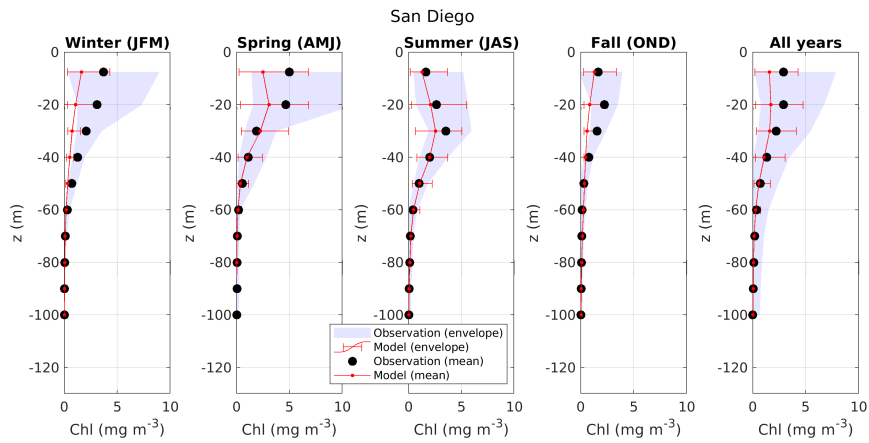


Figure S13: Same as Fig S10 for San Diego using City of San Diego stations.

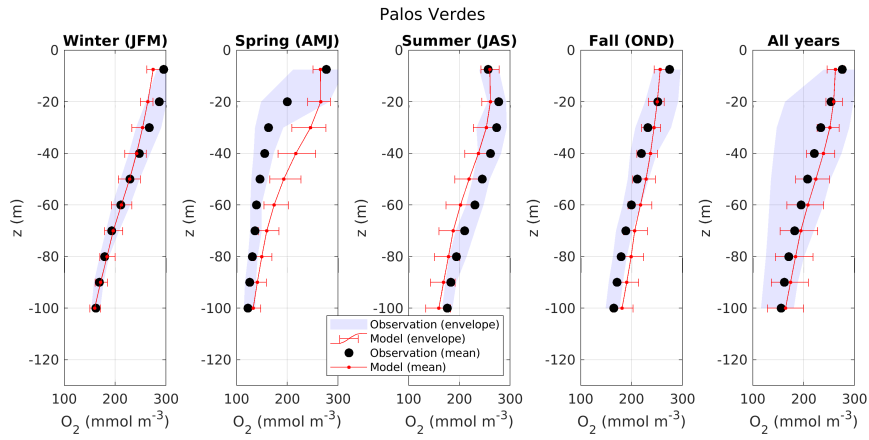


Figure S14: Seasonal profiles of average dissolved oxygen concentration off of Palos Verdes. The red line and red bars are the spatial and temporal means and the variability from the model. The black dots and the gray shade are the spatial and temporal mean and the variability from *in situ* data (LACSD stations). These profiles are showing agreement on intensity, seasonality and shape of the vertical profile with exceptionally high concentrations at mid-depth.

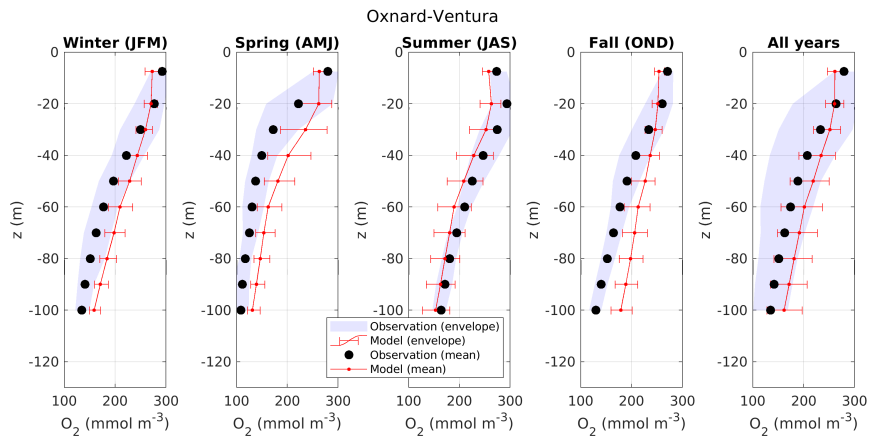


Figure S15: Same as Fig S14 for Oxnard/Ventura using City of Oxnard stations.

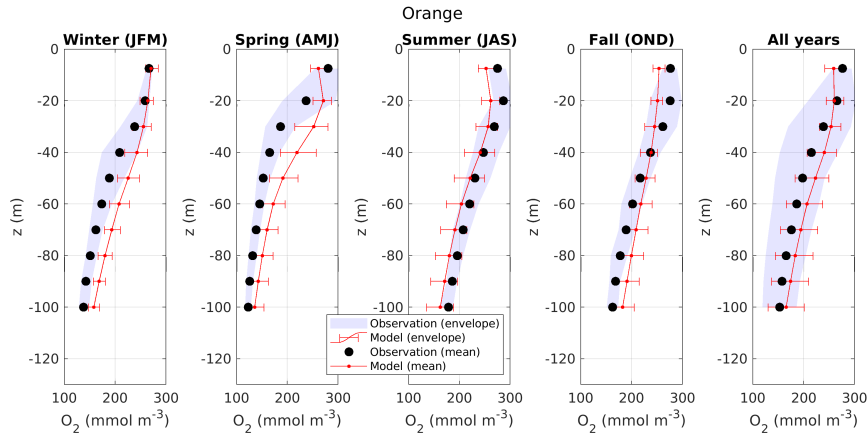


Figure S16: Same as Fig S14 for Orange County using OCSO stations.

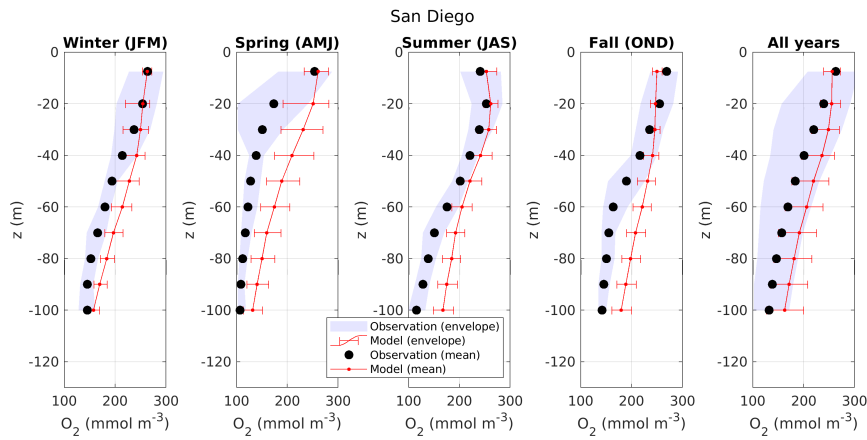


Figure S17: Same as Fig S14 for San Diego using City of San Diego stations.

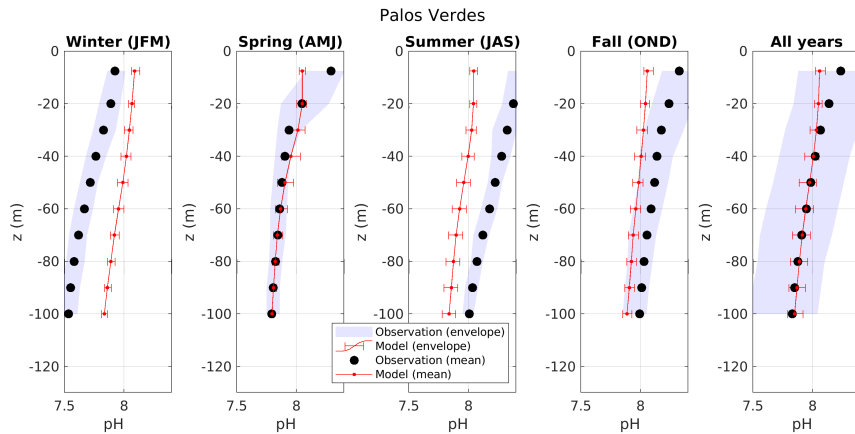


Figure S18: Seasonal profiles of average pH (seawater scale) off of Palos Verdes. The red line and red bars are the spatial and temporal means and the variability from the model. The black dots and the gray shade are the spatial and temporal mean and the variability from *in situ* data (LACSD stations). These profiles are showing agreement on intensity, seasonality and shape of the vertical profile with exceptionally high concentrations at mid-depth.

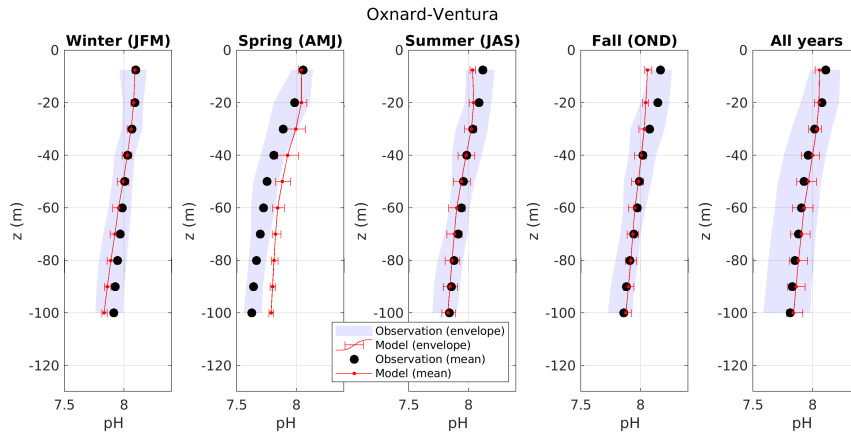


Figure S19: Same as Fig S18 for Oxnard/Ventura using City of Oxnard stations.

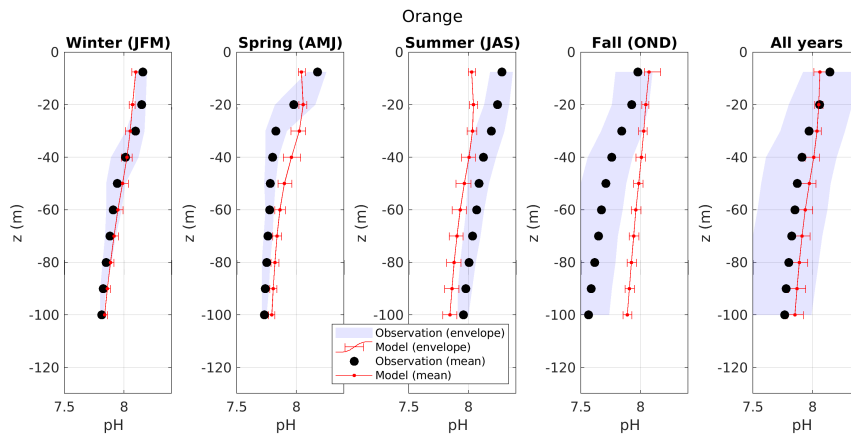


Figure S20: Same as Fig S18 for Orange County using OCSD stations.

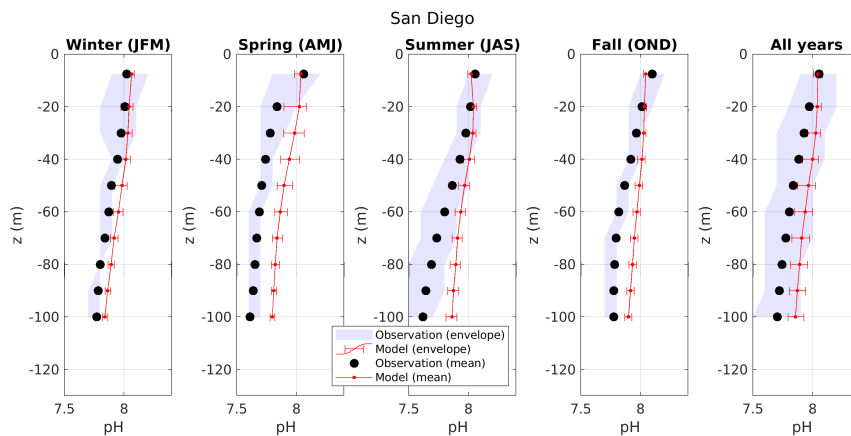


Figure S21: Same as Fig S18 for San Diego using City of San Diego stations.

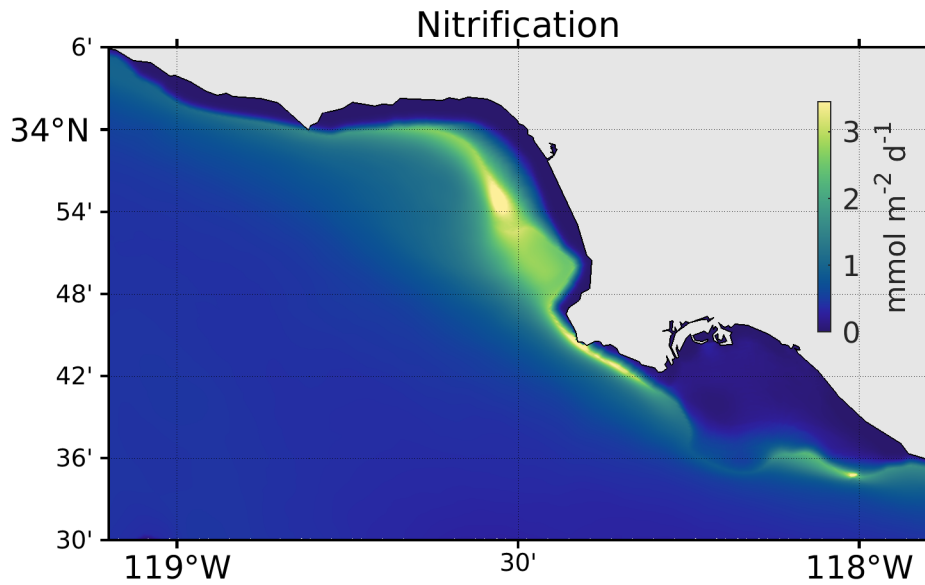


Figure S22: Average nitrification rate in Santa Monica and San Pedro bays. This figure shows the high rates around the locations of the outfalls that results from the release of high concentrations of ammonium below the thermocline.

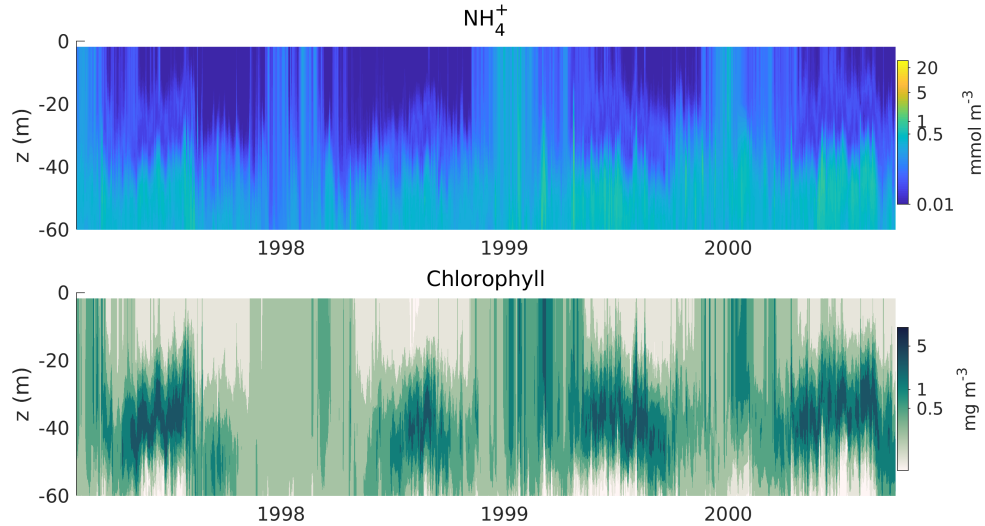


Figure S23: (a) Hovmöller of ammonium concentration at San Pedro Oceanic Time-series (SPOT) located mid-distance between Los Angeles coast and Catalina Island. (b) idem as (a) for chlorophyll *a* concentration. The Hovmöllers show 1) ammonium concentration off Los Angeles coast are not affected by anthropogenic loads. 2) Deep chlorophyll *a* maximum is trapped below at subsurface for 70% of the time and reach concentration of about 2 mmol Chl  $\text{m}^{-3}$ . Depth of the subsurface chlorophyll *a* maximum shows a seasonal cycle where it varies between 20 and 40m.

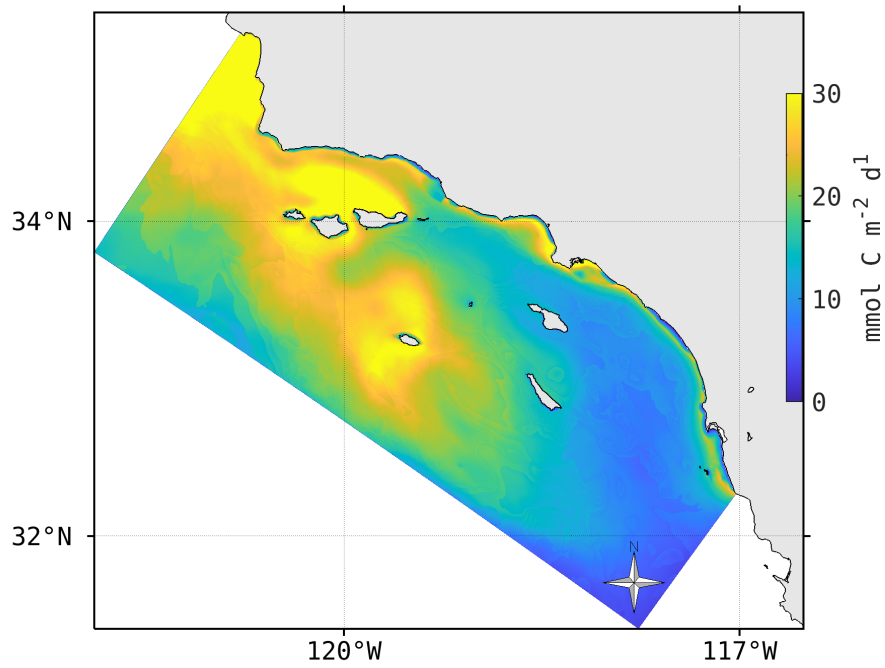


Figure S24: Summer time 1997-2000 average carbon export at 40 m in the SCB. The map shows hot-spots of intense carbon export in Santa Barbara and Los Angeles coasts.